Models and Image Reconstruction in Electrical Impedance Tomography of Human Brain Function

Adam David Liston

In collaboration with University College London,
Submitted for the Award of PhD. to

**The School Health and Social Sciences
Middlesex University**

May 2003

Abstract

Electrical Impedance Tomography (EIT) of brain function has the potential to provide a rapid portable bedside neuroimaging device. Recently, our group published the first ever EIT images of evoked activity recorded with scalp electrodes. While the raw data showed encouraging, reproducible changes of a few per cent, the images were noisy. The poor image quality was due, in part, to the use of a simplified reconstruction algorithm which modelled the head as a homogeneous sphere. The purpose of this work has been to develop new algorithms in which the model incorporates extracerebral layers and realistic geometry, and to assess their effect on image quality.

An algorithm was suggested which allowed fair comparison between reconstructions assuming analytical and numerical (Finite Element Method - FEM) models of the head as a homogeneous sphere and as concentric spheres representing the brain, CSF, skull and scalp. Comparison was also made between these and numerical models of the head as a homogeneous, head-shaped volume and as a head-shaped volume with internal compartments of contrasting resistivity. The models were tested on computer simulations, on spherical and head-shaped, saline-filled tanks and on data collected during human evoked response studies.

EIT also has the potential to image resistance changes which occur during neuronal depolarization in the cortex and last tens of milliseconds. Also presented in this thesis is an estimate of their magnitude made using a mathematical model, based on cable theory, of resistance changes at DC during depolarization in the cerebral cortex. Published values were used for the electrical properties and geometry of cell processes (Rall, 1975). The study was performed in order to estimate the resultant scalp signal that might be obtained and to assess the ability of EIT to produce images of neuronal depolarization.

Acknowledgements

Thanks to:

My supervisors, Richard Bayford, who has always been supportive and given helpful guidance, and David Holder, who kept pointing out the wood from the trees.

My colleagues, past and present, Adam Gibson, Tom Tidswell, Andrew Bagshaw, Rebecca Yerworth, Ori Gilad and Gershon Ahadzi for laughs, advice and collaboration and for feedback on parts of this thesis.

Those who gave me things, Hamid Dehghani, for his wonderful Matlab FEM code, Tom Tidswell for his human and tank data and Andrew Tizzard for his fine meshes.

Those who offered advice when I approached them, Kevin Boone, Hugh Bostock, for his wisdom concerning electrophysiological modelling, Simon Arridge, for his enthusiasm about analytical models and Tom Fearn for his recommendations on statistical analysis.

My parents and my friends for their encouragement and support, in particular Vanessa who helped me keep an even keel in the final stages and whose prayers were constant.

God, for the strength to continue and for rich blessings at the worst of times.

Contents

List of Figures

1 Introduction and Review

2 Image Reconstruction using Analytical and Numerical Methods

3 The Effect of Layers

4 The Effect of Geometry

5 Imaging Neuronal Depolarization

List of Tables

1 Introduction and Review

3 The Effect of Layers

4 The Effect of Geometry

5 Imaging Neuronal Depolarization

List of Abbreviations

ACT   Applied Current Tomography

RNA   Ribonuclaeic Acid

ASA   Advanced Source Analysis

BEM   Boundary Element Method

BOLD   Blood Oxygenation Level Dependent

BREIT   BOLD-Related Electrical Impedance Tomography

CAP   Compound Action Potential

CAT   Computerised Axial Tomography

CBV   Cerebral Blood Flow

C-normalisation   Column-normalisation

CSF   Cerebrospinal Fluid

CT   Computed Tomography

DC   Direct Current

DSM   Direct Sensitivity Method

EcoG   Electrocortigogram

EEG   Electroencephalography

EIT   Electrical Impedance Tomography

EITS   Electrical Impedance Tomograpic Spectroscopy

EP   Evoked Potential

FEM   Finite Element Method

FISH   Fluorescence *In Situ* Hybridization

fMRI   functional Magnetic Resonance Imaging

FNOSER   Fast Newton One-Step Error Reconstruction

Fs   Sampling Frequency

FWHM   Full Width at Half Maximum

Hb   Hemoglobin

HbO_2 Oxygenated Hemoglobin

I-DEAS   Integrated Design and Analysis Software

IEG   Immediate-Early Gene

IPT   Industrial Process Tomography

LHS   Left Hand Side

MaTOAST	Matlab Time-resolved Optical Absorption and Scattering Tomography
MEG	Magnetoencephalography
MRI	Magnetic Resonance Imaging
MSE	Mean Squared Error
NIRS	Near Infra Red Spectroscopy
NOSER	Newton One-Step Error Reconstruction
NURBS	Non-Uniform Rational B-Spline
PET	Positron Emission Tomography
PoP	Plaster of Paris
rCBF	regional Cerebral Blood Flow
RHS	Right Hand Side
rms	root mean square
R-normalisation	Row-normalisation
SEP	Somatosensory Evoked Response
SPM	Statistical Parametric Mapping
SQUIDS	Superconducting QUantum Interference Devices
SPECT	Single Photon Emission Computerised Tomography
SVD	Singular Value Decomposition
TOAST	Time-resolved Optical Absorption and Scattering Tomography
ToDLeR	Three-Dimensional, Linearised Reconstruction algorithm
VER	Visual Evoked Response

List of Symbols

σ   Conductivity

E   Electric Field

ϕ Electric Potential

H   Magnetic Field

J   Current Density

V   Voltage

v_n Normalized Voltage

A   Sensitivity Matrix

Z   Impedance

I   Current

Ψ,Φ   Electric Potential

M   Number of Measurements

N   Number of Pixels/Nodes

R   Row-Normalization Matrix

C   Column-Normalization Matrix

+   (*operator*) Moore-Penrose pseudo-inverse

♦   (*operator*) Square Moore-Penrose pseudo-inverse

w Elements of the Weighting Matrix

S   Support Matrix

v elemental volume

K   Matrix Containing Singular Values

r   Position Vector

r   Radial Position

Many further symbols are used in the derivations in Chapter 5 and at no other point in the thesis. Those symbols are listed clearly there to avoid duplication above and confusion where they are symbolic of different quantities.

Statement of Authorship

The research work described in this thesis was undertaken in collaboration with the UCL EIT group, led by David Holder and co-led by Richard Bayford (Middlesex University). Members of this group, past and present, and their direct contributions to work described in this thesis include:

Kevin Boone – formulation of the principles for DC measurement; calculations of impedance decreases due to neuronal depolarization under "sealed-end" boundary conditions; crab peripheral nerve measurements. **Adam Gibson** – development of an analytical homogeneous model for conduction in a sphere; development of a linear, non-iterative, truncated SVD algorithm for image reconstruction with the homogeneous sphere model; design of measurement protocol for human measurements. **Tom Tidswell** – Visual Evoked Response measurements; measurements on head-shaped tank (with skull); image viewing software. **Andrew Bagshaw** – debugging (in collaboration with **myself**) 3D MaTOAST code; production of spherical meshes; head-shaped tank measurements (without skull) with **Richard Bayford. Andrew Tizzard** – production of head-shaped meshes.

An external contribution was that of the MaTOAST code by **Hamid Dehghani** to produce the numerical solution for electric field in a 3D object when current is injected. The following research elements of this thesis where specific undertaken by myself:

Derivation and Matlab implementation of analytical solutions to electric field within a 4-shell sphere, in spherical co-ordinates, by differentiation of the solution for electric potential in literature (Ferree, Eriksen et al. 2000); suggestion and implementation of new processing in algorithm to make it a "level playing field"; building on existing, purpose-built, Perspex hemispheres, construction of a spherical tank phantom with electrodes on the inside and casting of a hollow spherical shell to simulate the skull; collection of all spherical tank data. "Open-end" solution for peripheral nerve resistivity changes and all code used for calculations in Chapter 5.

Refereed Papers as a Result of this Work[1]

Bagshaw, A. P., A. D. Liston, et al. (In press). "Electrical Impedance Tomography of Human Brain Function using Reconstruction Algorithms based on the Finite Element Method." Neuroimage.

Liston, A. D., R. H. Bayford, et al. (2002). "A multi-shell algorithm to reconstruct EIT images of brain function." Physiological Measurement 23: 105-119.

---

[1] These are included in an envelope attached to the back of this thesis.

Introduction and Review

1 Introduction and Review

1.1 Overview

The word tomography is derived from the Greek *tomos* meaning *volume* and *graphi* meaning *writing*. Electrical impedance is that which obstructs the flow of current. Therefore Electrical Impedance Tomography (EIT) can be used to describe the impedance properties of an object of interest, in this case, the human head. In the following report, I describe the development of improved mathematical models of current flow through the head and the benefit they bring when used to reconstruct EIT images of human brain activity.

This introduction contains an overview of current methods to image the brain, a review of EIT applications, a discussion of EIT as a brain imaging modality, a description of the apparatus and the algorithms used, and a review of the mathematical models that have been used thus far in EIT image reconstruction.

1.2   *Imaging the human brain*

1.2.1   Body Worlds

Much is known about the anatomy of the body. All medics learn first hand in the dissection room. One could also consult, in medical textbooks, the drawings made from life (or, more often, death), visit the Visible Human Project® Website (http://www.nlm.nih.gov/research/visible/visible_human.html), or attend the Body Worlds exhibition if it takes place nearby and one has the stomach.

Techniques for examining the anatomy without the body in question expiring or being cut open are preferable when the subject is a patient with a malady, or a volunteer for research, receiving £10 for their time. They can still be classed, however, as non-invasive or invasive and safe or biologically damaging. Radionuclide imaging of body function is an invasive and biologically damaging technique whereby a radioactive tracer is injected into the body and its radiative emissions are detected. The simple photographic X-ray and X-ray Computed Tomography (CT) are non-invasive but this radiation can damage the tissue of the examiner and examinee. The former technique is often used to find fractures in bones and the latter to produce internal maps of tissue contrast. A safe and non-invasive technique is ultrasound, which sends high-frequency sound waves into the body and measures the echo that returns. It is most famously used to image the foetus in the womb. Magnetic Resonance Imaging (MRI) is also safe and non-invasive, and works on the level of atomic nuclei. It is likely that the brain images the reader is most familiar with were generated using CT and MRI.

1.2.2   The Brain

1.2.2.1   Anatomy

Before discussion of the activity of the brain and *functional imaging* using EIT, the subject of this thesis, mention will be made of the foundation on which it is built, the anatomy of the brain and *anatomical imaging*. The latter might also be referred to as *static* or *absolute* imaging whilst the former might be called *dynamic* imaging, where images are expressed as a comparison with a control or a baseline state.

Last year, I was privileged to attend a course on brain anatomy at UCL, during which I held a human brain in my gloved hands. It is a complicated, undulatory mass of tissue in the form of many *gyri* (rounded elevations) separated by many *sulci* (furrows). It is made up of the *brainstem*, the *cerebellum*, the *diencephalon* and the *cerebrum*, the latter two constituting

the **forebrain**, which is split into a left and a right hemisphere (Figure 1-1). Individual brains differ substantially but, on each hemisphere, landmark sulci enable identification of four lobes: **frontal, parietal, occipital** and **temporal** (Figure 1-1). These are responsible for different areas of perception and conscious control, some of which will be discussed in Chapter 4 in relation to functional EIT studies of humans.

The *cerebral cortex* exists on the cerebral surface and extends several millimetres into the volume. It is also known as *grey matter* and consists of a suspension of cells called *neurons* and *glial cells* in *extracellular fluid*. Neurons are the cells that relay electrical signals throughout the brain, similar to the nerves that relay signals from the fingertips to the spinal cord, for example. Glial cells provide structural and metabolic support for cortical neurons. Also present beneath the cortex is *white matter*, which consists of *myelin*-coated *axons*, which relay signals from one part of the cortex to another. Throughout the brain run veins and capillaries, which direct and regulate the flow of blood there.

Cerebrospinal fluid (CSF) bathes the brain and fills its *ventricles*, cavernous formations near the centre of the cerebrum. It contains small quantities of glucose and protein, circulates to remove waste products and helps the brain to float within the skull.
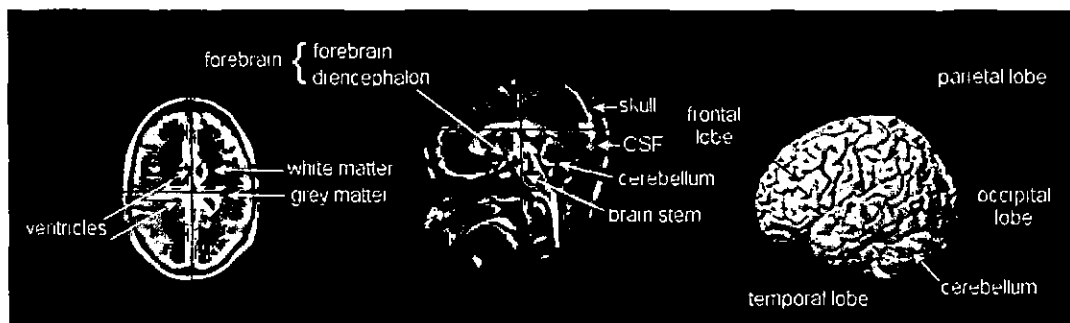
Figure 1-1: An MRI image of Lauren Stewart's brain showing the different anatomical regions. There is low contrast between CSF and skull so it is difficult to discern one from the other in the figure.

1.2.2.1.1   Computerized Axial Tomography (CAT SCAN)

If a simple X-radiograph were to be taken of the head, the structure of the skull would be revealed but the subject would appear brainless. This is because there is little attenuation of X-rays within brain tissue and there is no depth information from the technique when rays are used at the energy necessary to penetrate bone. More useful is CT or Computerized Axial Tomography (CAT). Here, a circular system of X-ray sources and detectors is rotated about the head. Information is acquired concerning the attenuation of the X-rays through only a thin slice of the brain and is then reconstructed into a tomographic image by a computer

algorithm. A CAT Scan is well suited for finding tumours and other abnormalities within the brain. A state of the art system might acquire four slices of data in 1/3s and reconstruct images with resolution under 1mm in less than a second (http://imaginis.com/ct-scan/spiral.asp).

1.2.2.1.2   Magnetic Resonance Imaging (MRI)

Structural details can also be revealed in the brain by MRI. This technique relies on the resonant properties of the nuclear magnetic moment in the hydrogen atoms attached to oxygen forming water throughout the volume under examination. The first two-dimensional images, using nuclear magnetic resonance, were produced in 1973 (Lauterbur 1973) of two capillaries of H_2O suspended in a tube of D_2O. In the presence of a high field B_0 (1-3T in MRI today), the nuclear moments precess about the field direction, like a spinning top, at a characteristic frequency dependent on B_0. If a pulse of radiation is applied at an appropriate radio-frequency, there is resonance and the moments are flipped. They change state briefly and, after a characteristic time, return to their original, preferred state whilst emitting the energy they absorbed. In MRI acquisition, *gradient coils* are used to apply a spatially variant field in addition to the standing field B_0. Therefore, nuclei at different positions have resonance at different frequencies and absorb and emit different quanta of energy. Because their emissions are therefore spatially tagged, it is possible to reconstruct an image of hydrogen density.

1.2.2.2   Function

Much has been learnt about the *function* of the brain by relating *post mortem* sections or CT- or MRI-detected abnormalities to symptomatic *dysfunction* in subjects. For example, someone who suffers damage to their motor cortex (located in the parietal lobe) may have their movement impaired, or, to their visual cortex (located in the occipital lobe), their vision (Ramachandran and Blakeslee 1998). Much inference has also been made from dissection of laboratory animals after sacrifice, but this is limited since God "teaches more to us than to the beasts of the earth" (Job 35:11) and there is a large difference in complexity between animal and human brains. Lessons learnt from these studies have been informative but cannot show us all we might wish to know about how the human brain works. For this, it is necessary to employ dynamic monitoring and imaging methods, the most common of which are listed below, along with several novel techniques that have been proposed and may contribute to

the field. Although EIT is one, it will not be discussed until section 1.2.2 since it is the subject of this thesis and requires a more thorough explanation.

1.2.2.2.1 Electroencephalography (EEG)

Electrophysiological methods have long been used to study the function, over milliseconds, of individual neurons. Their depolarization, or "firing", is well understood, as is the integration of signals on their cell projections, *dendrites*, from the *synapses* of neighbouring neurons - a neuron does not behave in a vacuum and brain function depends on the spatial and temporal synchrony of large populations of neurons.

Local behaviour of many neurons has been studied using depth electrodes but the electrical signature of neuronal activity can also be detected on the surface of the cortex (an *electrocortigogram*, *ECoG*) or with scalp electrodes (an electroencephalogram). *Electroencephalography* (*EEG*), the most widespread monitoring technique, measures voltage changes on the scalp providing information about the electrical activity of neurons near the surface of the cortex. EEG can be used to study a subject's response to visual, auditory or somatosensory (touch and movement) stimulation, or to detect abnormal activity associated with *epilepsy* or *encephalitis*.

The magnitude of the signal depends not only on the number and location but also the geometry of the synchronously firing neurons, since it possible for many arrangements to generate currents so that their associated potential distributions cancel. Therefore EEG is sensitive to the dendritic currents of active *pyramidal neurons*, oriented parallel to each other so that their potential distributions do not cancel. Temporal resolution is high and data is normally collected at a sampling rate of around 250Hz, sufficient to describe a 70ms interictal spike, common in epilepsy, with over 17 data points. However, while EEG successfully localizes active areas of cortex close to the skull, localization of deep activity is less reliable. EEG is non-invasive and safe. It is also inexpensive and widely used as a clinical tool. It is, however, difficult to detect signals from neurons deeper in the brain, and spatial resolution is poor.

EEG can be used as a *parametric* or an *imaging* tool in the estimation of EEG sources in the brain (Baillet, Mosher et al. 2001). In the former, also called *inverse dipole modelling*, it is assumed that the electrical activity in the cortex can be represented by a few equivalent dipole sources. The number, localization, magnitude and orientation of these are estimated, iteratively, until the calculated potential distribution matches best the measured voltages at the scalp electrodes. As an imaging tool, dipoles are assigned to each tessellated element on

25

the cortical surface and are oriented perpendicular to that as are the pyramidal sources. Only the amplitudes are unknown and these are varied again until the calculated potential distribution best matches the data. For parametric modelling, since the activity in the cortex is distributed, it can be that a single dipole cannot adequately represent an active section of cortex or that the dipole that does so exists outside the head! It is also found that, the more dipoles a model guesses, the less successful it is. For source imaging, the number of unknowns is two orders of magnitude higher than the number of electrodes so the problem is severely underdetermined and difficult to solve without some mathematical trickery.

1.2.2.2.2   Magnetoencephalography (MEG)

Magnetoencephalography (MEG) also provides information about the electrical activity of pyramidal neurons, similar to EEG, with high temporal resolution. Electrodes are replaced by small, inductive coils arranged on the inside of a helmet about 3cm from the subject's scalp. Tiny currents are induced by the changes in magnetic field associated with dendritic currents and these are measured using Superconducting QUantum Interference Devices (SQUIDS). The magnetic field is attenuated less by the skull than is the electric field so MEG is theoretically more sensitive than EEG. The problem of contact impedance is avoided, since the sensors do not come into contact with the scalp, and the positions of the sensors are well defined. However, MEG apparatus is expensive and immobile. It requires a dedicated, shielded room and also high maintenance in order to sustain SQUID operation.

1.2.2.2.3   Tracer-enhanced CT

Associated also with neuronal depolarization are metabolic demands, met, in the active area, by increased regional cerebral blood flow (rCBF). Several techniques rely on the change in tissue characteristics caused by this increase and are listed briefly here. For CT to be used to image physiological activity it must be tracer-enhanced. It works in exactly the same way as does anatomical X-ray CT except that the subject inhales a large proportion of stable xenon (Johnson, Stringer et al. 1991) or is injected with a *bolus* or contrast agent. This modifies the absorption characteristics of the tissue where it accumulates and therefore enables imaging of rCBF. Spatial resolution is high and, although temporal resolution used to be very low with this technique, recent improvements have meant that a slice of data can be acquired in under a second and can trace contrast changes even over the very short rise time of a compact bolus (Konig 2003). Brain perfusion imaging has the potential to be very useful

in early stroke management because it examines the underlying pathophysiology rather than simply structural signs of tissue damage.

1.2.2.2.4   Positron Emission Tomography (PET)

PET can be used to image blood flow or metabolism, closely coupled to neural activity (Jueptner and Weiller 1995), and has been a great aid to cognitive neuroscience (Fox and Raichle 1984; Raichle 1998). It has also had a huge impact in areas such as cerebrovascular disease, epilepsy, and cerebral tumours. It relies on the detection of the two 511keV photons produced when a positron and an electron are annihilated (Ter-Pogossian, Phelps et al. 1975). Metabolic glucose consumption can be monitored using the decay properties of radioactive ^{18}F-labelled glucose compounds (Carson, Wu et al. 2003). For perfusion studies, the source of positrons could be emission by the injected radiopharmaceutical $H_2^{15}O$, which can be easily produced and which has a half-life of about two minutes, enabling many repeat experiments in the same subject. Also used are the radionuclides Carbon-11, Nitrogen-13, and Fluorine-18. Pairs of photons produced by annihilation are emitted at 180° to each other so that the site of the event can be deduced from the timing and location of their detection. The theoretical limit of spatial resolution of this technique is 2-3nm because this is the distance the emitted positron travels before it is annihilated. However, in practice, the technique has a resolution of about 6mm.

1.2.2.2.5   Single Photon Emission Computerized Tomography (SPECT)

Similar to PET, SPECT acquires information on the concentration of radionuclides introduced to the patient's body. However, because only a single photon is emitted, a collimator is required in order to know the direction from whence the photon came. Where PET might employ 500 detectors, only 3 collimators might be used in SPECT. Detection efficiency is greatly reduced and, consequentially, so too are sensitivity and resolution (about 7mm). However, SPECT can be performed at approximately one-third the cost of PET due to the nature of SPECT instrumentation and the availability of the appropriate nucleotides such as Xe-133 (Wirestam, Ryding et al. 2000). It may be useful in the diagnosis of Alzheimer's disease (Jagust, Thisted et al. 2001).

1.2.2.2.6   Functional Magnetic Resonance Imaging (fMRI)

The dynamic version of MRI is functional MRI. This relies, once again on paramagnetic contrasts within the brain. Here the source of contrast is not the variation of anatomical tissue

but of rCBF, changes in which can be detected either by paramagnetic labelling of blood entering the brain or by blood deoxygenation contrast since HbO_2 is paramagnetic and Hb is not (Jezzard and Turner 1996). The latter is known as the blood oxygenation level dependent or BOLD signal. Its strict relation to neuronal activity will be discussed at more length in section 1.2.2.2.11, except to say an increase in rCBF disproportionate to an increase in oxygen uptake results in a focal hyperoxygenation (Menon 2001). FMRI has led the way in examination of cognitive function, along with PET but it is fMRI that is the main tool for research imaging of normal brain function. Most commonly used without injected tracers, it is a non-invasive technique that has high sensitivity and a spatial resolution of about 4mm. Its temporal resolution, seconds, is adequate to record rCBF changes which occur over several seconds. The disadvantages of fMRI are its expense and its requirement of a dedicated, shielded room - it is estimated that image acquisition from one subject costs £600.

1.2.2.2.7   Near infra-red spectroscopy (NIRS)

Changes in optical properties occur in neuronal tissue when there are changes in its functional state. The causes are varied and include microscopic structural changes, the release of neurotransmitters and changes in rCBF and its oxygenation. Many approaches use dyes but a technique such as Near Infra-Red Spectroscopy NIRS) relies on the intrinsic optical signals measured from tissue. Often, the technique has been applied to the exposed cortex *in vivo* and, by absorption and scattering measurements in the spectral range between 650 and 950 nm, can detect changes with excellent spatial and temporal resolution (Grinvald 1992). Oxygenation images have also been obtained by measurement over a 10x10 cm area on the scalp though it is difficult for the light to penetrate the skull and the images are low-resolution. For a review of these techniques see Obrig and Villringer (2003).

1.2.2.2.8   Optical tomography

Near-infra red light has also been used in order to produce tomographic images of brain function using *optical tomography*. Light is absorbed and scattered by the medium through which it passes and, as for NIRS, the oxygenation of cerebral blood can be investigated by injection and measurement using fibre-optic *optodes* on the scalp. The technique is similar, both mathematically and practically, to Electrical Impedance Tomography except that electric current is not absorbed as is electromagnetic radiation. Images have been reconstructed using data collected from 32 time-resolved channels on a neonatal head and the distribution of absorption has been presented due to a cerebral haemorrhage (Hebden, Gibson et al. 2002).

The numerical models for current flow, described later in this thesis, are based on those used by the UCL optical group to model absorption and scattering of injected light.

1.2.2.2.9 Other techniques

Another technique claims to provide information about neural activity. Fluorescence *in situ* hybridization (FISH) (Guzowski, McNaughton et al. 2001) is a technique which benefits from the transient induction of immediate-early gene (IEG) transcription in neurons after periods of synaptic activity. The distribution of subcellular *Arc* (an immediate early gene) RNA in rats, measured using FISH and laser scanning confocal microscopy, was then used to give information about the timing of individual neuron activation before the animal's sacrifice. The experiment they described allowed visualization and comparison of the neural populations activated by two different behavioural experiences and could allow further investigation of the roles of different populations in cognitive processes. At no stage will this provide a useful way of imaging the function of the human brain since it is required that animals are sacrificed less than 16 minutes after the stimulus, but much may be inferred from animal studies.

Some work has indicated that, by selected detection and suppression of rapidly and slowly changing magnetic fields, it may be possible to use MRI for detection of the ultraweak, transient field changes caused by neuronal currents (Bodurka and Bandettini 2002). The signals are at the limit of detection and physiological artefacts are present several orders of magnitude greater than those due to neuronal currents. Also, as in EEG, the signal is dependent on the geometry of the active neurons and can be reflected as either a magnitude or a phase change.

1.2.2.2.10 Multimodality imaging

Since it does not seem that there is one brain imaging technique that possesses both high temporal and the spatial resolution it has been suggested that different imaging modalities be integrated in order to relate their signals to information processing at the neuronal circuit level (Dale and Halgren 2001). There are two main methods to interpret *multimodal* results, both of which use information about the haemodynamic response to precondition EEG inverse modelling. The first is the "seeded-dipole" technique, whereby the electrical activity in the brain is represented by a small number of dipoles, as in parametric EEG modelling, described above. The initial guess is informed this time by the activation foci derived from PET or fMRI. The second uses imaging with EEG. Here, dipoles are assigned to many voxels

describing the cortical surface and are given orientation perpendicular to this surface. A solution is found for the dipole strength at each of these voxels and data from PET or fMRI is used to bias the solution, spatially, towards areas of the cortex that are haemodynamically active.

1.2.2.2.11 Insights Into Brain Function

Many conclusions have been made about neurological function by use of the above techniques. An extensive review can be found in Jueptner and Weiller (1995) but some will be listed in the following as deemed relevant to the work described later in this thesis.

Logothesis (2001) claimed, using both fMRI and electrophysiological recordings, that BOLD activation in an area reflects incoming input and local processing at the neuronal scale, rather than spiking activity, supporting findings that a visual stimulus is accompanied by an increased BOLD signal in the visual cortex. Radiographic studies have revealed close coupling between rCBF and local glucose metabolism in humans (Baron, Grandie et al. 1982). In a PET study by Fox and Raichle (1984) rCBF was shown to increase in the visual cortex, in association with visual stimuli, by an amount related to the rate of stimulus. They concluded, from this evoked response experiment, that the rCBF response size was a function of the number of neurons responding to each stimulus.

There is also a reverse effect when decreased neuronal activity leads to decreased blood flow (Kelly and McCulloch 1983). A PET study by Mentis *et al.* (1997) showed rCBF to decrease in extensive regions at the front of the brain in addition to the increases in the visual cortex during the evoked response. Prolonged negative BOLD signals have been found in some brain regions during stimulation and it has been suggested to reflect inhibition or suppression of neuronal firing patterns (Raichle 1998). Little is known about these signals. It has even been shown that a negative BOLD signal, whilst accompanying a decrease in *cerebral blood volume (CBV)*, occurred in a region of increased neuronal activity (Harel, Lee et al. 2002). This was detected in a region adjacent to another that gave a positive BOLD signal.

1.3 The Role of Electrical Impedance Tomography (EIT)

Electrical Impedance Tomography (EIT) is a non-invasive, safe, portable imaging technique that enables images of electrical impedance to be reconstructed from voltages measured with an array of electrodes placed on the body. Typically, an image data set is collected as a series of many tetrapolar impedance measurements designed to sample as much of the volume as possible. Before describing its application to imaging brain function, a little background will be provided as to the other areas of its use.

EIT was used in geological studies as long as 70 years ago (Stephanesco, Schlumberger et al. 1930) and industrial groups today use the identical technique Industrial Process Tomography (IPT) to detect air bubbles in process pipes or to monitor mixing processes (Webster 1990). There is even a group performing EIT of tree trunks! However, discussion here will be limited to the potential clinical applications of EIT.

1.3.1 Gastrointestinal function

Changes in gastric emptying can be an indicator of many functional disorders of the gastrointestinal tract, e.g. *pyloric stenosis*, and of stress (Akkermans, Tekamp et al. 1993). Also, slow gastric emptying can be a problem in the management of newborn babies recovering from intensive care (Devane 1993).

In the past, gamma scintigraphy has been used to follow the passage of a radioactive meal in adult experiments. Another method requires the patient to swallow a nasogastric tube, which is then used to extract samples of stomach contents some time after delivery of a dye substance. The volume of the stomach can be found from the ratio of dye delivered to its concentration in the removed sample. Dynamic EIT images are much more desirable, however, since the technique avoids the use of radioactive isotopes and, to which the author can testify, intubation is uncomfortable. Instead, electrodes can be attached easily around the abdomen, where there are no bony structures to obstruct current flow, and EIT can be used to follow meals such as porridge (Wright 1993) or meals labelled with saline.

There have been shown to be significant linear correlations between times to half emptying ($t_{1/2}$) measured with scintigraphy and with EIT (Mangnall, Baxter et al. 1987). Also shown were highly significant differences between gastric emptying in normal infants ($t_{1/2}$ = 18min) and those with hypertrophic pyloric stenosis ($t_{1/2}$ = 46min).

1.3.2 Pulmonary function

Clinically, EIT could be very useful for imaging ventilation and detection of blood clots in the lungs or pulmonary emboli, a common and often serious complication of surgery. It may also be of use to monitor the drainage of a pneumathorax caused by pulmonary lesions, since the impedance of air is very high, providing high contrast with the surrounding tissue.

Planar X-ray, X-ray CT, MRI and radioisotope scintigraphy can all be used, with high spatial resolution, to image pulmonary ventilation and perfusion. However, the patient is required to be brought to the device and repeated exposure to radiation is undesirable. For these reasons, EIT is very useful for such an application as it can be wheeled to the bedside. It has even been used during parabolic flights to determine regional ventilation and fluid shift signals in lateral posture during normo-, hyper- and micro-gravity (Dudykevych, Frerichs et al. 2001). However, one problem is that, as well as being sensitive to lung impedance changes, the technique is also sensitive to the ribs and to tissue movement, which can be large sources of artefact.

Electrical impedance tomographic spectroscopy (EITS) has been used at a range of frequencies (9.6kHz to 1.2MHz) to produce static images of the thorax (Brown, Leathard et al. 1995). This enabled analysis of changes in tissue impedance with respect to frequency after reconstruction of data from 12 normal subjects during breath held at maximum inspiration and at maximum expiration. The resulting tissue characterization was consistent with an electrical model of the lungs based on the Cole equation where parameters were those related to alveolar structure and composition. The group at Rensselaer has developed an adaptive current tomography (ACT) system with which they imaged a simulated pulmonary embolus in a dog, first ventilating one lung at a time and then occluding a major branch of the pulmonary artery. The region of the lungs that was ventilated but not perfused by blood, had different electrical properties and, therefore, was observable in a time-varying conductivity map of the thorax. The group also reconstructed conductivity changes during lung ventilation in human volunteers using both a ring of electrodes placed around the thorax and a 4x4 rectangular array placed on the subject's chest (Cheney, Isaacson et al. 1999; Mueller, Isaacson et al. 2001). It has been reported, however (Holder and Temple 1993), that use of EIT is ineffective for diagnosis of anything other than the grossest of pulmonary lesions since inter-patient variability is so high. Therefore a more realistic aim might be the continuous monitoring of the same patient over time.

1.3.3   Thoracic blood volume

It has been suggested that EIT may be used to measure cardiac output or isolated perfusion defects, suggesting a pulmonary embolism and the requirement of anti-coagulants. Advantages and disadvantages of EIT over other techniques are similar to those for its use in pulminory monitoring.

It is possible, in EIT of the thorax, to perform cardiosynchronous averaging and produce dynamic impedance images describing different times in the cardiac cycle (Eyüboglu, Brown et al. 1987). The Rensselaer group have reported changes in their conductivity images correlating with the heartbeat (Mueller, Isaacson et al. 2001) and, more recently, sources of a cardiac-related electrical impedance waveform have been reconstructed using data from thoracic surface measurements made on human subjects (Hoetink, Faes et al. 2002). Their separation, spatial and temporal, corresponded well with MRI measurements of surface area changes of the thoracic organs during the cardiac cycle.

1.3.4   Breast tumours

Early detection and treatment of tumours in the breast increases chance of survival amongst women who develop breast cancer. The properties of many tumours, in particular malignant tumours, differ significantly from the surrounding tissue and separation and characterization of contrasting tissues can deliver this early diagnosis.

At present, women are screened for breast cancer using X-ray mammography, though some cancers of the breast cannot be seen using this technique. During this procedure, their breast is compressed flat in order to visualize all the tissue and minimize the required radiation dose - this can be uncomfortable and sometimes painful for the patient. Another disadvantage of the technique is the high (40%) false-positive rate. A positive test is highly alarming and requires the patient to undergo further testing, which could include fine-needle aspiration or *biopsy*. Meanwhile, the false-negative rate is 26% Regular screening is recommended for women over 40 years old but the technique is difficult with younger women whose breast tissue is in general more dense.

The EIT group in Moscow produced three-dimensional tomographic images of *in vivo* breast tissue among women with different hormonal status using a circular grid of 256 electrodes (Cherepenin, Karpov et al. 2002). Multifrequency EITS has produced some promising results for detection of breast malignancies. In a study at Dartmouth, participants lay prone on a customized table and 16 radially-adjustable electrodes were put into contact with the pendant breast (Kerner, Paulsen et al. 2002). Of 6 out of 26 subjects who had ACR

4-5 suspicious lesions, inspection of EIS images, using visual criteria, resulted in 83% detection specificity and numerical criteria 67%. A larger study was performed by Transcan Medical Ltd, who used a probe, containing a square grid of 64 electrodes, to examine the breasts of a learning group consisting of 83 carcinomas and 378 benign cases (Glickman, Filo et al. 2002). They achieved a sensitivity of 84% and a specificity of 52%, which suggests that the false-negative rate may be 10% less than that of mammography. Ongoing studies are being carried out to improve the post-processing algorithm.

1.3.5   Hyperthermia

Reduction of tumour size is possible in certain malignancies using temperature treatment or *hyperthermia*. This involves concentrated heating of the tumour tissue to about 47°C without damaging the surrounding tissue.

A non-invasive form of thermometry would be valuable in order to ensure that the heating remains focused only on the malignant region. Since there is a linear relationship between temperature and tissue resistivity (2% / °C (Foster and Schwann 1989)), EIT may be useful in this application. However, it has been found that there are artefacts in the resistance images due to other physiological factors and that they are significant compared to the temperature-dependent changes (Liu and Griffiths 1993). The feasibility of EIT for thermometry has also been questioned in light of changes in tissue fluid content during hyperthermic treatment and of the different impedance spectra of skeletal muscle and tumour tissue in rats during the same (Lin and Griffiths 1993).

1.3.6   Other Medical Applications

Not all electrical impedance techniques are tomographic. Measurements can be used for a range of applications, such as measuring body composition, assessing the effect on the skin of moisturisers, probing for malignancy in cervical squamous tissue, bubble detection and assessing the technical quality of meat, to name but a few. However, the main medical applications of impedance tomography have been listed above and it remains to review investigations into the potential use of EIT to monitor the brain.

1.4   EIT of the Human Brain

Potentially, EIT could be applied to imaging both structural and functional abnormalities in the human brain. EIT has several advantages over existing brain-imaging techniques. These include cost, portability, the non-invasive and safe nature of the measurement, the potential for ambulatory measurement and, finally, speed. Already, as described in section 1.3.3, it has been used to resolve events within one cardiac cycle. The Sheffield Mk 3.5 EIT/EIS system can acquire 33 frames per second (Wilson; Milnes et al. 2001) but EIT can, in principle, record hundreds of images per second. Therefore it is probably the only existing technique with the potential to image neuronal depolarization, the fundamental unit of brain activity, which occurs over tens of milliseconds.

The main disadvantage of EIT for general anatomical applications is its poor spatial resolution in comparison to MRI or CT. This is true also for functional imaging of the brain when EIT is compared to fMRI and PET, although less so in the case of PET and the further acquisition time is reduced in fMRI. For EIT of the human brain, spatial resolution is reduced even further because the highly resistive skull prevents much of the injected current from entering the brain region. EIT also has significant inter-subject variability so it is possible that its clinical use may be limited to intra-subject studies.

The precise physiological mechanisms of the observable impedance changes will be discussed in detail in section 1.4.2 but in the next section are listed the main fields within brain imaging where EIT could contribute and a review of investigations therein.

1.4.1   Electrical properties of tissue

At a later stage in this thesis will be described realistic models of the conductive behaviour of the head at both microscopic and macroscopic levels. Below are documented the many measured, macroscopic values of resistivity for each of the tissues present, the brain, the CSF, the skull and the scalp.

The impedance of living tissue has resistive and reactive components because of the presence of fatty cell membranes. For this reason, it is more difficult to pass current through it at lower frequencies than at high frequencies. At low frequencies, flow is generally restricted to the extracellular space but as frequency is increased, current begins to bypass the membranes and enter the cells themselves, resulting in a resistivity decrease. In the following, the reactive component is neglected and we may speak in terms of frequency-dependent resistivity rather than the complex impedivity.

1.4.1.1   The brain

It is difficult to compare the measurements made of the resistivity of cerebral cortex because they have been made using different electrode configurations and current frequencies. Ranck (Ranck 1963) measured the resistivity of rabbit cerebral cortex to be 3.21 ± 0.45 Ω m at 5Hz and 2.30 ± 0.37 Ω m at 5 kHz. He used two pairs of electrodes, one to deliver current and one to measure a potential difference between two points in the tissue. This is a four-terminal measurement, which avoids the effects of electrode polarization at low frequencies and can be taken to give a reliable result. In rats (Ranck 1966) he determined cortical resistivity to be around 2.5 Ω m using a similar method. Van Harreveld (VanHarreveld and Ochs 1956) found it to be $2.30 - 2.85$ Ω m by making measurements with two electrodes at 1kHz on the surface of rabbit cortex and then comparing them with measurements on the surface of a block of agar of brain dimensions. Later (VanHarreveld, Murphy et al. 1963) he found the resistivity of rabbit's cortical tissue to be 2.08 ± 0.06 Ω m at 1kHz using two depth electrodes, one deeper than the other along a line perpendicular to the surface of the cortex. Freygang and Landau (1955) used the four-electrode method and found cortical resistivity to be 2.22 ± 0.09 Ω m using pulses of constant current lasting between 0.3ms and 0.7ms. It is difficult to determine to which frequency this measurement equates because the membrane RC time constant for neurons is of order milliseconds so it is unlikely that the voltage induced by the constant current reached steady state while the pulse endured. It is important that a mathematical model in chapter 5 predicts resistivities similar to those listed above at appropriate frequencies. A summary of the above results is given in Table 1-1.

Source	Animal	Resistivity (Ωm)	Technique	Measurement Frequency (Hz)
Ranck (1963)	Rabbit	3.21 ± 0.45	4-electrode	5
Ranck (1963)	Rabbit	2.3 ± 0.37	4-electrode	5000
Ranck (1966)	Rat	2.5	4-electrode	1.5-3000
Van Harreveld and Ochs (1956)	Rabbit	2.3-2.85	2-electrode	1000
Van Harreveld et al. (1963)	Rabbit	2.08 ± 0.06	2-electrode	1000
Freygang and Landau (1955)	Cat	2.22 ± 0.09	4-electrode	DC? (see text)

Table 1-1: Reported values for the resistivity of grey matter

White matter has a resistivity several times higher than grey and, in addition, is highly anisotropic. Using the 0.3-0.7ms pulse technique, the resistivity of cat white matter was found to be approximately 3.44 Ω m, almost double that of grey (Freygang and Landau 1955). Van Harrefeld (1963) found the resistivity of rabbit white matter to be over 4 times that of grey. In their review, Geddes and Baker (1967) report values, averaged over low-frequency, body temperature measurements on rabbits and cats, of 2.84 Ω m and 6.82 Ω m for the resistivity of grey and white matter respectively. In addition to this, they also report the ratio of transverse to longitudinal resistivity of this fibrous tissue ranging between 5.7 and 9.4.

1.4.1.2   The CSF

The resistivity of CSF is 0.56 Ωm, as measured most recently by Baumann (1997) at body temperature. CSF is perhaps the most easily measured of the constituents of the head listed here.

1.4.1.3   The skull

Skull resistivity is a bone of contention! Reports range from 18 Ωm at 1MHz on freshly excised human bone tissue (Hemingway and McLendon 1932) to approximately 90 Ω m for excised rat femur at 10kHz (Kosterich, Foster et al. 1983). Law (1993) reported large variations in skull resistivity from site to site. Four-terminal measurements, made at 100Hz, revealed resistivities between 13.6 Ωm at a *suture* line and 214 Ωm at *compact* bone. The overall mean was 75.6±41 Ωm, and the large standard deviation simply reflects the variation from one point to the next and brings into question the validity of reporting a mean value.

Rush and Driscoll (1968) found the effective resistivity of skull, when soaked with a conducting fluid, to be 80 times that of the fluid. If the fluid were to be CSF, the skull resistivity would be 45 Ωm. More recently, it has been suggested that the contrast between skull resistivity and that of brain was much less than was previously implemented in models (Oostendorp, Delbeke et al. 2000). Specifically, a mathematical model of the head, used by Rush and Driscoll (1969), and others subsequently, assumed a ratio of 1/80 between brain and skull resistivity. Rather, Oostendorp *et al.* (2000) suggest, this should be modelled as the contrast between CSF and skull. At 100 Hz-10 kHz, their measurement of 66.7±13.0 Ωm (2000) is, respectively, about 14 and 120 times greater than the resistivity values reported above for brain and CSF, and it is very similar to that of Law.

The anisotropy of bone is well demonstrated by the results of Saha and Williams (1992), who made measurements at 100kHz on the *tibia* bone to find the axial, circumferential and radial mean resistivities to be 16, 158 and 215 Ωm.

1.4.1.4   The scalp

Only a single measurement of conductivity of scalp has been generally cited (Burger and Milaan 1943) but researchers often use a value of 2.27 Ωm the average of skin and muscle.

1.4.1.5   The blood

The resistivity of human blood is dependent on the amount of *haematocrit* (red cells) it carries. Resistivities of between 1.3 and 1.7 Ωm were measured by Rosenthal (1948) for 37°C blood at normal levels (~ 40%) of haematocrit at a frequency of 1kHz.

1.4.1.6   Summary of head resistivities and conductivities

Amongst the ranges of reported values for the resistivity of constituents of the head, one was chosen, for each, for the purpose of modelling in this thesis. These are summarized in Table 1-2. Since this thesis describes mainly the comparison of algorithms for reconstruction of simulated and tank data, the choice of values was not deemed to be crucial.

Tissue type	σ ($\Omega^{-1}m^{-1}$)	Reference for σ	Outer radius of tissue type (mm)
brain	0.25	Geddes and Baker (1967)	80
CSF	1.79	Baumann (1997)	82
skull	0.018	Law (1993)	87
scalp	0.44	Burger and Milaan (1943)	92

Table 1-2: Values used for resistivity and conductivity in this thesis

1.4.2   Resistance changes in the brain and their visibility using EIT

There are three categories of resistance changes in the brain that may be imaged using EIT, large, medium and small. Each of the following sub-sections contains a brief look at the theory of the changes and a review of investigations made by the EIT community.

1.4.2.1   Large, pathological resistance changes

Large resistance changes occur over seconds, minutes or hours due to *cell swelling*, or *ischemia*. Here, metabolic demands are not met, due to the prolonged, repetitive activity during epilepsy, for example, or due to an interruption of the supply of oxygen-carrying

blood, as in stroke (Lux, Heinemann et al. 1986). This results in *anoxic depolarization*. As a consequence, the active pumps fail to maintain the correct balance of ions inside and outside the neurons (*homeostasis*), and *osmosis* occurs (Hansen and Olsen 1980). This reduces the amount of extracellular space in the ischemic region and increases its resistivity .

1.4.2.1.1   Neonatal intraventricular haemorrhage (IVH) and hypoxia-ischemia

There is a high risk of intraventricular haemorrhage (IVH) in a neonate and early diagnosis can lead to improved treatment. When blood displaces CSF there is approximately a three-fold resistivity increase (see section 1.4.1) which should be detectable using EIT. Another cause of disabling or fatal brain injury is hypoxia-ischemia, caused by the lack of oxygen or blood to the brain at birth. Of great use in neonatal care would be a cotside system, such as EIT, that imaged the head continuously.

Neonatal imaging has mainly been confined to studies of the lungs (Brown, Primhak et al. 2002). However, some preliminary images were presented by Murphy et al. (1987), and numerous evoked response experiments have been performed on neonates by this group. These have been reported at conferences but sufficient data has not yet been acquired to publish.

1.4.2.1.2   Stroke

In treatment of stroke, it is important to know what type of stroke has occurred, ischemic or haemorrhagic in order to know which drug to administer. For ischemic stroke, blood is not reaching the damaged area and delivering the oxygen required for metabolism, resulting in *apoptosis*, a process of cell death. In this case, if a blood clot is causing the blockage, it is necessary to administer *antithrombalitics* to break it down, although the effectiveness of these drugs is greatly reduced after the first 3 hours. It would be extremely undesirable to administer such drugs if the stroke were to be haemorrhagic. EIT is a technique that could provide immediate and continuous bedside monitoring of stroke patients and would not require the expense and inconvenience of MRI.

Resistance increases of 15-60% were obtained by 50kHz measurements on the cortical surface of anaesthetized rats with induced ischemia (Holder 1993). Scalp measurements returned changes 5-10 times less than this, suggesting that it would be possible to image changes in resistivity caused by ischemic stroke. These measurements were relative to a baseline, however, and, since baseline images cannot be acquired from a stroke patient it is thought that EITS (see section 1.3.2) will be a more appropriate technique for proper stroke

diagnosis. Work is in progress at UCL to develop a multifrequency system to produce static, tissue contrast images of stroke.

1.4.2.1.3   Epilepsy

Focal epilepsy is a functional abnormality often related to a structural abnormality like a lesion, and an individual's seizure always originates from the same cerebral focus. For patients with intractable epilepsy, surgery is required to remove that part of the brain and accurate localization of the *epileptic focus* is crucial before surgical excision. As mentioned above, the repetitive activity due to a focal seizure can cause local ischemia, detectable using EIT (Lux, Heinemann et al. 1986). Continuous monitoring is necessary because the occurrence of seizures is so unpredictable, therefore EIT may be better suited than fMRI for localization of epileptic foci. At present EEG inverse dipole modelling has been attempted for such a purpose. Patients have their epilepsy-suppressing medication suspended for a week prior to surgery, during which time they are monitored with EEG in order to gain as much electrical information as possible during seizure activity. This technique, known as telemetry, is quite successful for localization of superficial foci but less so for foci situated deeper in the brain. For these, EEG electrodes are often implanted deep in the brain, a process which can cause irreversible damage. EIT may provide a more powerful, as well as less invasive, alternative for their localization.

Previous work with EIT involved the placement of electrodes on the exposed cortex of anaesthetized rabbits. This showed the magnitude of the conductivity changes during an induced epileptic seizure to be about 10% (Holder, Rao et al. 1996; Rao, Gibson et al. 1997; Rao 2000). Studies are being carried out at present using scalp EIT electrodes in addition to EEG electrodes to collect data from presurgical patients in the telemetry ward at King's Hospital. Preliminary results have been presented from data that have been collected ictally (Bagshaw, Liston et al. In press). These were encouraging, although no substantial claims have been made for them at this stage. In the two subjects considered for that publication, localized conductivity increases could be seen with the same lateralization as is expected from the EEG telemetry data. In addition, the images produced from two seizures in the same patient were consistent with each other.

1.4.2.1.4   Spreading depression and migraine

Cortical spreading depression (CSD) was first reported by Leâo (1944) and takes the form of a wavefront of intense electroencephalographic (EEG) activity which travels at about

3mm min^{-1}. In the wake of this is left a depression of EEG activity, as cell swelling occurs, and a DC potential shift as the extracellular ionic content changes (Hansen and Olsen 1980). The propagation of the wavefront is thought to be caused by the passive diffusion of excitatory neurotransmitting substances ahead of the active region (Bures, Buresova et al. 1974). Study of the speed of propagation of the auras experienced by sufferers of migraine has suggested that the mechanisms for this may be similar to those for CSD but this yet to be confirmed (Welch, Barkley et al. 1987).

An accompanying resistivity increase occurs as a result of the cell swelling. At 1.6kHz this has been measured as a 100% change (Hoffman, Clarck et al. 1973) and as 40% at 50kHz (Ranck 1964). In experiments carried out by this group, Boone (1994; 1995) initiated an episode electrically in 6 anaesthetized and paralysed rabbits and, upon cortical measurement using a ring of 16 electrodes, observed resistivity increases in reconstructed APT images of 5-20%, moving at 2-5mm min^{-1}. Most recently, Yoon (1999) measured a conductivity decrease at 100kHz of 5%, with a latency of 30-60s, followed by a change of 34% with a latency of 200-300s.

1.4.2.2   *Medium, functional changes - slow*

Medium-sized resistance changes occur over a time course of seconds as a result of changes in rCBF or, more specifically, cerebral blood volume (CBV), during normal brain activity. Since blood is about 4 times less resistive than the cortex (section 1.4.1) it is expected that CBV increase will produce a resistance decrease in a reconstructed EIT image and that it is possible, therefore, to image brain function using EIT. Although there are already proven good techniques for imaging the metabolic response due to brain function, efforts towards this end in impedance tomography are very worthwhile as a means to test algorithms and hardware by comparison of images with the "expected" results obtained by fMRI and PET (see section 1.2.2.2.11)

Using the cardiosynchronous EIT method described in section 1.3.3, McArdle (1993) observed conductivity changes of magnitude 0.2% in the adult human head, related to the cardiac cycle after 500 cycles were averaged. EIT images have also been obtained using a ring of 16 electrodes on the cortical surface of anaesthetized rabbits during intense photic stimulation in both eyes (Holder, Rao et al. 1996). Resistance decreases of 4.5 ±2.7% were observed in the appropriate cortical areas with a time course similar to the stimulation. More recently human evoked response experiments have been carried out by the UCL group (Gibson 2000; Tidswell, Gibson et al. 2001b). Although surface resistance measurements

generally changed in magnitude by 0.5-1% during stimulation, there was a large variability in changes observed in the reconstructed images. Only 19 out of 52 recordings returned changes localized in the "expected" cortical region.

1.4.2.3   Small, functional changes - fast

The change of resistive properties in individual neurons underlies all neural activity. When a neuron depolarizes, ion channels open in the cell membrane and its resistance decreases over tens of milliseconds (Cole and Curtis 1939; Araki and Terzuolo 1962). Therefore it is easier for current to flow inside the neurons during depolarization than during the resting state, as is shown diagrammatically in Figure 1-2. Qualitatively, therefore, we expect the resistance of the tissue containing depolarising neurons to decrease while the extra ion channels remain open. When the activity of a population of neurons displays spatial and temporal coherence, as in normal brain function, there is therefore an accompanying resistivity change in the active tissue as a whole. This lasts for tens of milliseconds, the length of the signal on an EEG trace accompanying an evoked potential. The mechanisms of neuronal depolarization will be discussed in more detail in chapter 5, as will the relationship between the associated microscopic and macroscopic impedance changes.

EEG successfully localizes electrically active areas of cortex close to the skull with sufficient temporal resolution to distinguish neural events tens of milliseconds apart. But, as mentioned above, localization of deeper activity is less reliable. FMRI and PET may be used to generate images of activity with a high spatial resolution throughout the brain but their temporal resolution is only sufficient to observe metabolic consequences of neuronal depolarization. It would be of great use to cognitive studies could an imaging technique combine the spatial and temporal resolution of fMRI/PET and EEG respectively to map neuronal activity itself, rather than its consequences. A technique such as EIT has the capability of measuring with sufficient time-resolution to do so if it can attain the sensitivity required to detect the small changes associated with neuronal depolarization (Boone and Holder 1995). Boone predicted a resistance decrease of about 0.01% measured on the surface of the scalp (Boone 1995) and that the maximal resistance change associated with neuronal depolarization occurs when measurement is made at DC.
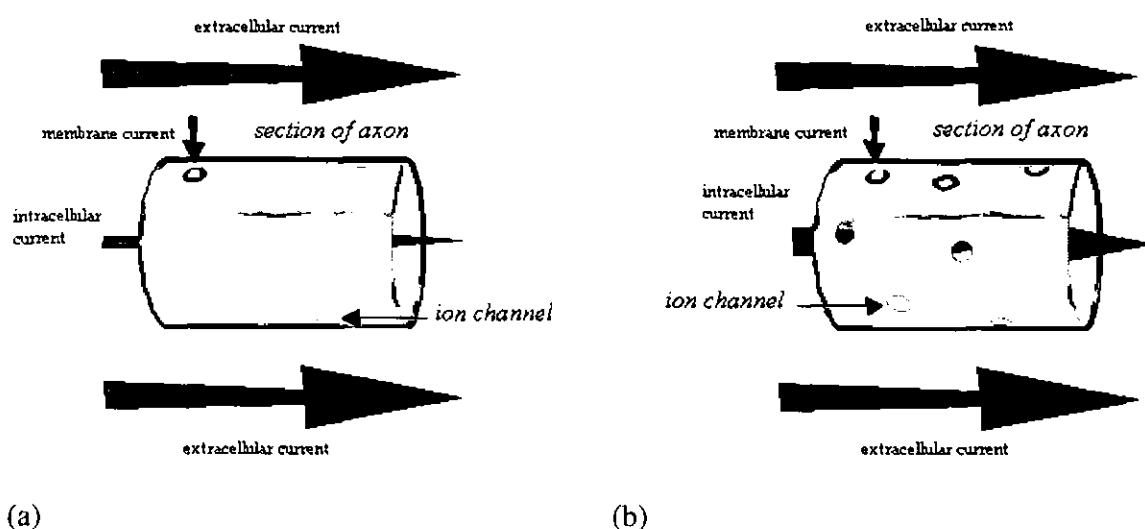
Figure 1-2: The flow of externally applied current inside and outside an axon and across its membrane (a) during the resting state and (b) during depolarization. More current flows through the intracellular space during depolarization.

Klivington and Galambos (Klivington and Galambos 1968) reported localized cortical resistance changes of 0.005% at 10kHz, during auditory evoked responses in the cat. They used a sharpened, intracranial wire electrode and a platinum plate electrode resting on the adjacent cortical surface. This means that over half the total sensitivity was due to a 1-mm layer of tissue surrounding the wire electrode, where current density was maximal. This is a volume similar to that containing the evoked, neuronal activity. Therefore the method was very sensitive to localized changes in resistivity, directly comparable with the measured changes in resistance. Freygang and Landau (1955) used the four-electrode method described in section 1.4.1.1 to measure a decrease of 3.1%±0.8% due to direct electrical stimulation on the surface of the cortex. Boone measured resistance changes of –0.01% to –0.03% due to evoked responses in rabbit brains (Boone 1995). He stimulated the median nerve, injected a square wave of constant current between electrodes 1-3mm apart and measured voltage between electrodes 9mm apart. All electrodes were on the surface of the cortex.

1.4.3   Implications for EIT

In summary of the previous section, there are broadly three potential modes of operation for EIT for use in imaging the human brain, one anatomical and two functional.

43

1.4.3.1   Anatomical-mode

With use of multi-frequency current injection, it may be possible to produce static images of tissue contrast within the head. EITS could then be used to diagnose stroke, IVH and hypoxic-ischemia in adults and neonates. While the anatomical-mode can be considered static, it is also possible to monitor the patient over time with the same technique and to produce continuous, dynamic, multifrequency images as these conditions deteriorate or improve.

1.4.3.2   FMRI-mode

The first functional mode may be called fMRI-mode whereby it is used to image the changes in rCBF or cell swelling associated with normal or pathological neural activity. EIT could be used in this mode to localize epilepsy and could be of some use in the investigation of migraine. EIT in fMRI-mode may also provide an alternative low-cost tool for investigations of cognitive function.

1.4.3.3   EEG-mode

It would be very exciting were EIT to become operational in the EEG-mode. Images could be obtained of resistance changes occurring over tens of milliseconds and the activity of different populations of neurons could be traced in time and space throughout the brain revealing much about cognitive processing and control. The predictions of models and the small measured changes suggest that sensible images in the EEG-mode will be difficult to achieve but are not beyond theoretical limitations.

1.5   *Instrumentation*

1.5.1   Absolute, Dynamic and Spectroscopic

There are three types of system in use at present in the medical applications of EIT, *absolute, spectroscopic* and *dynamic*.

In the first, current is applied through many electrodes in a trigonometric pattern designed to maximize sensitivity throughout the object. Examples of this are the ACT or ACT3 systems at the Rensselaer Technical Institute in the USA (Saulnier, Blue et al. 2001).

An example of an Electrical Impedance Tomographic Spectroscopy (EITS) system is the Sheffield Mk3.5 system, which uses eight electrodes and an adjacent drive/receive electrode data acquisition protocol to deliver packets of summed sine waves at frequencies between 2kHz and 1.6MHz (Wilson, Milnes et al. 2001).

A dynamic imaging system collects data over time in order to observe relative changes in impedance. An example of this is the Sheffield Mark 1 system (Barber and Seagar 1987).

Detailed discussion in this section will be limited to the systems used at UCL, in particular those used to acquire data in this thesis. See Boone *et al.* (1997) for a thorough review of EIT hardware.

1.5.2   Systems Used at UCL

1.5.2.1   HP-EIT

For human images published by (Tidswell, Gibson et al. 2001b), impedance measurements were made with an HP 4284A impedance analyzer (Hewlett Packard, http://www.hewlettpackard.com). This was modified in order to switch through different combinations of 4-terminal impedance measurements using 31 electrodes placed on the head. In a 4-terminal impedance measurement, two *drive* electrodes deliver current while the potential difference is measured between the other *measure* electrodes. Current was delivered at 50 kHz with a magnitude of between 1 and 2.5 mA using combinations of electrodes that were diametrically opposed to one another.

1.5.2.2   UCLH Mark 1b

The UCLH Mark 1b system can address up to 64 electrodes independently and employs a single 4-terminal impedance-measuring circuit and cross point switches, which can be controlled using software installed on a laptop. The electrodes are connected from the scalp to

a head-box the size of a videocassette, which is worn by the subject. This, in turn, is connected by a 10m ribbon cable to a base box, the size of a video recorder, which works at 18 single frequencies that can be chosen over the frequency band between 225Hz and 77Hz. The long lead allows the patient to be ambulatory and the size of the equipment allows the system to be portable.

The magnitude of the impedance is measured using a synchronous-demodulation voltage sensing circuit. Since signal phase is dependent on the positions of the drive and measure electrodes, and on the characteristics of the object under study, a phase shift is selected as optimal for each measurement combination so that demodulation occurs in-phase with the signal. Gain is also selected in order that the digitized voltage represents a sizeable proportion of the full range and digitization noise is minimized on the receive side. More than 600 hundred measurements can be made every second. The protocol used presently requires 258 measurements to be made during acquisition of one image. This takes just over 0.4s.

1.5.2.3   UCLH Mark 2 – EITS of the Human Brain

A new multifrequency EIT design has been developed, at UCL, which adapts the Sheffield Mark 3.5 system for use with up to 64 electrodes (Yerworth, Bayford et al. 2003). Cross point switches were added to a single current/receive module, on this system, in order to allow selection from any combination of 32 available electrodes and to produce what is known as the UCL Mark 2 system. The system was successful in producing multifrequency images of cylinders of banana with diameter 10% the diameter of a saline-filled, spherical tank.

1.6   Image Reconstruction

1.6.1   Overview

1.6.1.1   The inverse problem

EIT uses the voltages measured on the surface of an object of known geometry, through which a known current has been passed, to determine the distribution of conductivity inside that object. This is called the *inverse problem*.

1.6.1.2   The quasi-static forward problem

The solution of the inverse problem first requires solution of the *forward problem*, which is possible since we know the equations and the boundary conditions governing the flow of current through the object Ω under study.

For the purposes of reconstruction in this thesis, the problem is assumed to be *quasi-static* (Kleinermann 2001). This means that the effect of magnetic induction can be ignored in Maxwell's equations so that they become

$$\mathbf{E} = -\nabla\phi \qquad [1\text{-}1]$$

and
$$\nabla \times \mathbf{H} = \sigma \mathbf{E} + \mathbf{J}_{\text{impressed}} \qquad [1\text{-}2]$$

where E is the electric field, ϕ is the electric potential, H is the magnetic field and $\mathbf{J}_{\text{impressed}}$ are the current sources. If the divergence is taken on both sides of [1-2], and $\mathbf{J}_{\text{impressed}}$ is set to zero then, since there are no current sources inside Ω, it becomes

$$\nabla.(\sigma\nabla\phi) = 0 \text{ in } \Omega \qquad [1\text{-}3]$$

with Dirichlet boundary conditions $\phi = v_i$ under electrode i, or Neumann boundary conditions, $\sigma\nabla\phi.\mathbf{n} = j_i$ under electrode i and $\sigma\nabla\phi.\mathbf{n} = 0$ elsewhere. In this thesis we are concerned with known current injection j so, when this is defined, it is possible to solve the Neumann problem to find ϕ and hence v_i. In practice, a finite number of electrodes are used, giving a finite number N of possible voltage measurements. These can form a vector $\mathbf{V}=[\ v_1, v_2,..., v_N]$ which can be related to the conductivity distribution σ by a matrix $\mathbf{A}_\sigma$.

$$\mathbf{A}_\sigma\sigma = \mathbf{V} \qquad [1\text{-}4]$$

This is the formulation of the forward problem and the inverse problem requires recovery of σ knowing V. Because $\mathbf{A}_\sigma$ is dependent on σ, the matrix equation [1-4] can be said to represent a system of non-linear differential equations whose solution is σ. For the same reason, the inverse problem is also non-linear.

1.6.1.3 Uniqueness, ill-posedness and ill-condition

A solution to [1-4] is *unique* when no other solution for σ returns the same value of **V**. Is it possible in EIT that more than one conductivity distribution could produce the same boundary voltage measurements **V** within their precision? The answer is yes. If measurements were made to infinite precision and the entire object surface was sampled continuously, the solution would be unique. However, there is loss of information in the imaging process since data is discretely sampled and noisy and a large variation of resistivity may only produce a small variation in the discrete measurements. Therefore, the problem is *ill-posed*. It is also *ill-conditioned*, since small oscillations in the data (i.e. noise in **V**) can produce large, wild oscillations in the solution for σ. For further discussion of ill-posed inverse problems, the reader is referred to Bertero and Boccacci (1998). The measured data can suggest a set of approximate solutions for conductivity and it is wise to apply additional constraints from the physics of the problem. *Regularization* methods and *a priori* information will be discussed later in this section as a means to compensate for loss of information in order to reduce the solutions set.

1.6.2 The forward solution

1.6.2.1 Geselowitz and the linearized sensitivity relationship

The reciprocity theorem states that if a current I_Φ is impressed at points A and B on the surface of an object, giving rise to a voltage ϕ_{CD} between points C and D, the mutual impedance Z is the same as if current I_ψ were impressed at C and D and voltage ψ_{AB} was measured between A and B (Geselowitz 1971) so that

$$Z = \phi_{CD} \,/\, I_\Phi = \psi_{AB} \,/\, I_\psi \qquad [1-5]$$

The expected impedance measurement $Z = \phi_{CD} \,/\, I_\Phi$ can be calculated as follows, using Gauss' divergence theorem for a vector function f.

$$\int_s \mathbf{f} \cdot d\mathbf{S} = \int_v \nabla \mathbf{f} dv \qquad [1-6a]$$

Taking two scalar functions Φ and Ψ, and replacing f by $\Phi\nabla\Psi$ gives

$$\int_s \Phi\nabla\Psi \cdot dS = \int_v \Phi\nabla \cdot (\nabla\Psi)dv + \int_v \nabla\Phi \cdot \nabla\Psi dv \qquad [1-6b]$$

If Ψ is defined to be a solution to [1-3] and $\nabla\Psi$ is replaced by $\sigma\nabla\Psi$, so that the first term on the RHS vanishes, [1-6b] becomes

$$I_\psi \phi_{CD} = \int_v \sigma\nabla\Phi \cdot \nabla\Psi dv \qquad [1-7]$$

because the left hand side is a result of a surface integral that is only non-zero at the electrodes C and D. Therefore, from equation [1-5]

$$Z = \int_v \sigma \frac{\nabla\Phi \cdot \nabla\Psi}{I_\Phi I_\psi} dv \qquad [1-8]$$

Expanding [1-8] for perturbations in each variable except current, it is possible to derive the sensitivity relationship

$$\Delta Z = -\int_v \Delta\sigma \frac{\nabla\Phi(\sigma) \cdot \nabla\Psi(\sigma + \Delta\sigma)}{I_\Phi I_\psi} dv \qquad [1-9]$$

where ΔZ is the change expected in the impedance measurement. For small conductivity changes, it is assumed that $\nabla\Psi(\Delta\sigma) << \nabla\Psi(\sigma)$ in order that second order terms can be neglected in the expansion of $\nabla\Psi(\sigma+\Delta\sigma)$. Therefore, the linearized sensitivity relationship is

$$\Delta Z = -\int_v \Delta\sigma \frac{\nabla\Phi(\sigma) \cdot \nabla\Psi(\sigma)}{I_\Phi I_\psi} dv \qquad [1-10]$$

49

Physically, this means that the sensitivity of each measurement to internal conductivity changes remains constant, even while those changes from baseline occur. This approximation is valid as long as changes are sufficiently small, which is expected for human brain function where they are 20% or less (Holder, Rao et al. 1996), when caused by increased blood volume, and 1% or less when cause by neuronal depolarization.

At this point, it is worth pointing out that whilst, superficially, it may appear that impedance is proportional to conductivity, Φ and Ψ are inversely dependent on σ so that the units are consistent on either side of equations [1-8] and [1-10].

1.6.2.2 Discretization and the Sensitivity Matrix

The linearized sensitivity relationship must be discretized in order that it can be calculated on a computer. Instead of being integrated over volume, the scalar product is summed over N discrete volume elements making up the entire volume. This is a further approximation since it assumes that each of σ_n, $\Delta\sigma_n$, Φ_n and Ψ_n are constant within each element n.

In practise, M measurements are made of impedance so that equation [1-8] becomes, for each measurement m,

$$Z_m = \sum_n \sigma_n \frac{\nabla\Phi_{mn} \cdot \nabla\Psi_{mn}}{I_\Phi I_\Psi} \qquad [1\text{-}11]$$

and equation [1-10]

$$\Delta Z_m = -\sum_n \Delta\sigma_n \frac{\nabla\Phi_{mn} \cdot \nabla\Psi_{mn}}{I_\Phi I_\Psi} \qquad [1\text{-}12]$$

where the potentials in the latter are those for an unperturbed conductivity distribution. The MxN *sensitivity matrix* or *Jacobian* can then be defined as

$$A_{mn} = -\frac{\nabla\Phi_{mn} \cdot \nabla\Psi_{mn}}{I_\Psi} \qquad [1\text{-}13]$$

so that

$$V = -A\sigma \qquad [1\text{-}14]$$

and $$\Delta V = A\Delta\sigma \qquad [1\text{-}15]$$

where V and ΔV are the vectors containing measured voltages and their changes and σ and $\Delta\sigma$ are the vectors containing conductivity values and their changes in each element j. Physically, A contains in each row a voxel *map* $A_{m,n=1...N}$ of sensitivity for each measurement combination m sampled at N voxels. I_Ψ and I_Φ are often taken as unity for simulations.

1.6.2.3   Data-normalization or row-normalization

In most examples of dynamic image reconstruction, the measured voltage changes are normalized relative to the unperturbed, or reference, measurements V_{ref} so that fractional data are reconstructed.

$$\Delta v_{norm} = \mathbf{RA}\Delta\sigma \qquad [1\text{-}16]$$

where $\Delta v_{norm} = \Delta V\ .\ /\ V_{ref}$ and $\mathbf{R}$ is an MxM diagonal matrix whose diagonal is $1.\ /\ V_{ref}$. Here, the operation ". /" is an element-by-element division. $\mathbf{R}$ will also be referred to as the *row-normalization* matrix in the remainder of this thesis. This process of normalization causes partial cancellation of the errors introduced in ΔV and V as a result of deviations of the object from the expected geometry and of errors in electrode placement and, for this reason artefacts caused by these are less apparent in dynamic images.

1.6.2.4   Pixel-, Column-, or C-Normalization

In practice, another form of normalization is often used. Here, compensation is made for the large variation of sensitivity between regions close to and distant from electrodes by normalising for each element, voxel or pixel over all M measurements. This normalization can take the form of dividing each value in the column of the sensitivity matrix by the mean of absolute values in that column (Gibson 2000), by the root mean square (rms) of that column or just by the sum (Kotre 1994) so that

$$\kappa\Delta V = \mathbf{AC}\Delta\sigma \qquad [1\text{-}17]$$

where κ is the constant $\Delta\sigma^{-1}\mathbf{C}\Delta\sigma$ and $\mathbf{C}$ is an NxN diagonal matrix in which $C_{n,n}$ contains the normalization factor relevant for the nth element.

1.6.2.5   Analytical and numerical techniques

For simple objects, such as a plane, a circle, a sphere, or a cylinder, it is possible to solve for Φ and Ψ analytically at any points (often on a square grid) within the object and, hence, define the sensitivity matrix "exactly".

Alternatively, if the object in question is not of simple geometry, it is necessary to resort to numerical methods, such as the Finite Element Method (FEM) or Boundary Element Methods (BEM). These approximate the potential as linear or polynomial functions within volume or surface elements respectively. The resulting piecewise solutions are quite appropriate since the sensitivity matrix contains discrete coefficients each representing a finite volume. Further

discussion of these techniques will be left until section 1.7 which describes the modelling methods used thus far in EIT.

1.6.3   Linear reconstruction algorithms

1.6.3.1   Backprojection

In the reconstruction of CT images, a sensor detects the attenuation of an X-ray beam, which has travelled along a known path, and assigns an equal value for attenuation to each of the pixels it has passed through. When multiple beams have been passed through the object at all angles, the pixel values are combined. A pixel in a region of high attenuation will have affected all the beams passing through it and will have cumulated high pixel values relative to those surrounding it. The same principal has been applied to EIT despite the fact that the current path is so less well defined than that of X-rays.

In the *Sheffield Algorithm* (Barber and Brown 1986; Barber and Seagar 1987), compatible with data collected from the Sheffield Mark 1 system, the x-y plane is transformed into a *u-v* plane where *u* are isopotentials and *v* are isocurrents and a weighting function W=2*v*-1 is applied to each isocurrent pixel. Filtering was also required to deblur the image. This they applied empirically, to produce uniform resolution but also applicable is the *constrained optimization reconstruction technique*, in which the variance of pixel values is minimized given that their backprojection-weighted sum is equal to the sum of all the boundary potentials (Bayford, Hanquan et al. 1995). It was shown there, as suggested by Avis *et al.* (1994), who used the Sheffield back projection technique, that a *polar* (diametric) current drive protocol produced greater sensitivity at the centre of the image than does an *adjacent* current drive protocol, since more current is delivered to the centre of the object.

1.6.3.2   Sensitivity coefficient methods

To calculate the image value for a pixel n, Kotre (1994) used the normalized sensitivity coefficient there, described in section 1.6.2.3, in each measurement map $A_{m,n=1...N}$ to weight the corresponding measured voltage v_m in a summation over all the M measurements $m=1,...,M$. This method is equivalent to approximating the inverse of AC in [1-17] by its transpose. After transformation to equi-resolution space using a local magnification factor, and application of a Weiner filter, Kotre successfully reconstructed images of tank phantoms and the human thorax.

The Sheffield group applied sensitivity coefficient methods for 3-D reconstructions in order to avoid some of the conceptual difficulties involved in adapting the backprojection method from the 2-D case (Metherall 1998). The UCL group has also employed sensitivity methods to good effect in producing images of conductivity perturbations in 3-D tanks

(Tidswell, Gibson et al. 2001a). Both techniques involved the inversion of a sensitivity matrix, or Jacobian, data-normalized in the former (section 1.6.2.3). In the latter, pixel-normalization was employed (section 1.6.2.4) but, whilst normalized data was reconstructed (see LHS of [1-16]), the sensitivity matrix was not premultiplied by the matrix **R** (see RHS of [1-16]). The effects of this are explored in Chapter 2. The Jacobian is calculated in nearly all reconstruction methods in use today in order to map the conductivity space to the measurement space.

1.6.3.3   Perturbation methods

For *perturbation methods*, a perturbation matrix is generated instead of a sensitivity matrix, the elements of which are the inverse of the ratio of calculated change in measured voltage δv_i to the conductivity perturbation $\delta \sigma_j$ that causes it. Otherwise known as the "direct sensitivity matrix", it has elements approximately equal to $\partial \sigma_j / \partial v_i$ and can be multiplied by the vector of voltage changes in order to give an approximate solution for $\Delta \sigma$ (Morucci, Marsili et al. 1994; Morucci, Granié et al. 1995).

1.6.3.4   Singular Value Decomposition (SVD)

1.6.3.4.1   Principles

Singular value decomposition (SVD) is a technique by which a solution can be obtained for most *linear least-squares* problems. It is a very stable algorithm and allows an MxN matrix **A** to be analysed and then easily inverted (Golub and Loam 1996). This is decomposed so that

$$\mathbf{A} = \mathbf{U}\mathbf{K}\mathbf{V}^T \qquad [1\text{-}18]$$

where **U** and **V** are matrices of orthonormal vectors and **K** is the diagonal matrix whose elements k_{ii} are the eigenvalues, or singular values, arranged in order of decreasing magnitude. The inverse of an orthogonal vector is its transpose and that of a diagonal vector is simply another diagonal vector whose diagonal elements are ($1 / k_{ii}$) so that

$$\mathbf{A}^{-1} = \mathbf{V}\mathbf{K}^{-1}\mathbf{U}^T \qquad [1\text{-}19]$$

If M<N, as in the problem of EIT where few voltage measurements are required to provide a solution with many conductivity values, that matrix is *underdetermined*. In this situation, there are more unknowns than equations. In order to condition the matrix better, ($\mathbf{A}\mathbf{A}^T$) is inverted rather than **A**. If each of these are decomposed then

$$\mathbf{A}\mathbf{A}^T = \mathbf{U}\mathbf{K}\mathbf{V}^T\mathbf{V}\mathbf{K}\mathbf{U}^T = \mathbf{U}\mathbf{K}^2\mathbf{U}^T \qquad [1\text{-}20]$$

and the inverse, premultiplied by $\mathbf{A}^T$ to retrieve $\mathbf{A}^{-1}$ gives

$$\mathbf{A}^T (\mathbf{AA}^T)^{-1} = \mathbf{VKU}^T \mathbf{UK}^{-2} \mathbf{U}^T = \mathbf{VK}^{-1} \mathbf{U}^T \qquad [1\text{-}21]$$

as in [1-19]. Because $\mathbf{AA}^T$ is square, I will refer to this technique as square inversion of $\mathbf{A}$.

1.6.3.4.2   Analysis and regularization

If the eigenvectors are plotted, it can be shown that they represent or reach domains within the object of increasing spatial frequency and with increasing weight towards the centre (Breckon 1990). However, due to the ill-posedness of the problem, the singular values decay to values lower than bit-precision. In fact, the *rank* of the matrix is normally less than its size because the noise in the data introduces degeneracy of measurement. For this reason, the smaller singular values become meaningless. It is necessary, therefore, to *regularize* by truncation of the diagonal of $\mathbf{K}^{-1}$ in order that its diagonal elements k_{ii}^{-1} are zero beyond a defined threshold value for i. Otherwise, errors will become large. In practice, a truncation level is defined of r included singular values in order to reflect the noise levels of the measurement system and to maximize the spatial resolution and depth of sensitivity of the algorithm. The process is then a *pseudo-inversion* known as the Moore-Penrose pseudo-inverse of $\mathbf{A}$, $\mathbf{A}^+$, or, when $(\mathbf{AA}^T)$ is inverted, it shall be referred to as square Moore-Penrose pseudo-inversion of $\mathbf{A}$, $\mathbf{A}^*$

$$\mathbf{A}^* = \mathbf{A}^T (\mathbf{AA}^T)^+ = \mathbf{VK}^+\mathbf{U}^T \qquad [1\text{-}22]$$

The rate of decay of the singular values is indicative of the condition of the matrix.

Another method to improve the condition of a matrix is *Tikhonov regularization*, by which method, a weighted matrix $\mathbf{L}$ could be added to $\mathbf{AA}^T$ before inversion so that

$$\mathbf{A}^{-1} = \mathbf{A}^T (\mathbf{AA}^T + \varsigma \mathbf{L})^{-1} \qquad [1\text{-}23]$$

where ς is the weighting factor (Vauhkonen, Vadasz et al. 1998). A classic example of an *ad hoc* regularization matrix is the identity matrix $\mathbf{I}$.

1.6.3.4.3   The use of SVD

Eyüboğlu (1996) used SVD of the sensitivity matrix to reconstruct 2-D images and described the empirical process of choosing a truncation level for the pseudo-inverse in order that resistive objects could be seen in a tank. Without any truncation, he reported, it was impossible to see the objects. Kleinermann (Kleinermann and Avis 2000; 2001) used a truncated SVD algorithm with 2-D and 3-D sensitivity matrices in order to reconstruct images of objects inside a right cylindrical tank. Truncated SVD has also been used to invert recalculated Jacobians based on iteratively updated conductivity distributions in order to

approach the true distribution after several repeated calculations (Clay and Ferree 2002; Tang, Wang et al. 2002).

The UCL group has used the linear, non-iterative, truncated SVD algorithm for all the 3-D EIT images it has presented of tanks and human evoked responses (Gibson 2000; Tidswell, Gibson et al. 2001a; Tidswell, Gibson et al. 2001b). It could localize, to a reasonable degree, sponge resistance changes within a saline tank and some focal impedance changes within the brain, although at locations other than those suggested by physiology.

1.6.3.5   Iterative Methods

Initial estimates of a conductivity distribution can be improved, iteratively, by finding the best solution to measured data. Linear methods involve updating the conductivity distribution using an equation such as did Gibson (2000)

$$\sigma_{i+1} = \sigma_i - \tau \mathbf{A}^T(\mathbf{A}\sigma_i - \mathbf{V}) \qquad [1\text{-}24]$$

in a process known as in *Landweber's method*, where $\mathbf{S}\sigma_i - \mathbf{V}$ is the difference between the ith calculated voltages and the actual distribution and τ is a proportion which weights the *error image* $\mathbf{A}^T(\mathbf{A}\sigma_i - \mathbf{V})$. The iterations continue until the calculated and measured data match each other to within the accuracy of the system. He showed the iterative technique to have worse resolution than inversion by truncated SVD but similar accuracy in tank and computer simulation experiments.

1.6.3.6   Newton One-Step Error Reconstruction (NOSER), Fast NOSER (FNOSER) and Three-Dimensional, Linearized Reconstruction Algorithm (ToDLeR)

These techniques have been developed and are employed by the Rensselaer group (Saulnier, Blue et al. 2001). The Newton One-Step Error Reconstruction (NOSER) technique first finds the value of the homogeneous conductivity that minimizes the error between calculated and measured boundary voltages for EIT on a homogeneous and isotropic 2-D object of arbitrary shape. The code takes only one step of the Newton iterative method described in section 1.6.4.1., improving the speed of reconstruction, which is particularly important in 3-D. FNOSER is the computationally streamlined version of NOSER and ToDLeR extends the algorithm to the 3-D case.

1.6.4   Non-linear reconstruction algorithms

1.6.4.1   Gauss-Newton and modified Newton-Raphson methods

These are known as non-linear least squares estimations, which converge in distribution. They solve the inverse problem by iterative linearization of the non-linear relationship between resistivity and the electrical measurements. In order to do this, the Jacobian is recalculated at every iteration. The method was shown to out-perform perturbation and backprojection methods for reconstruction of 2-D, computer simulated resistivity distributions (Yorkey, Webster et al. 1987) but would be very costly when used in 3-D problems.

1.6.4.2   POMPUS

The Oxford group described a reconstruction algorithm, known as POMPUS, based on the use of optimal current injection, for distinguishability between regions, and iterative inversion (Paulson, Lionheart et al. 1993; Paulson, Lionheart et al. 1995). It was designed and shown to be many times faster than standard, Newton-based, reconstruction algorithms and yielded results comparable to those produced by these standard algorithms.

1.6.4.3   Layer-stripping

This technique involves the calculation first of impedance on the boundary by use of voltage measurements corresponding to highest spatial frequency, since they are most sensitive to variations near the surface (Somersalo, Cheney et al. 1991; Isaacson, Cheney et al. 1992). The voltages on the surface of the next, underlying layer are then synthesized and the process is repeated until the whole volume has been defined. This method would appear to be particularly applicable to an object which is naturally layered, such as the head and might be worth further investigation.

1.6.4.4   Temporal Optical Absorption and Scattering Tomography (TOAST)

Temporal optical absorption and scattering tomography (TOAST) is the algorithm used to reconstruct images for optical tomography by the UCL group (Arridge, Hebden et al. 2000). It works by iteratively updating the parameters in a FEM model in order to best-fit experimentally measured and predicted data. It was used successfully to produce the images described in section 1.2.2.2.8 (Hebden, Gibson et al. 2002).

1.6.5 Prior information

The ill-posed inversion problem in EIT must be regularized, as has already been stated. This can be performed by simple truncation of singular values at a point suggested by spatial resolution and noise considerations, or by *ad hoc* Tikhonov regularization. However, the problem can be made less ill-posed in a more intelligent way by the use of *a priori* information, if it is available.

1.6.5.1 Parametric Reconstruction

It has been suggested that the ill-posedness of the inverse problem in EIT could be cured if it was reduced to the calculation of a relatively small number of parameters (de Munck, Faes et al. 2000). The disadvantage of the technique is that a large amount of information needs to be obtained *a priori*.

1.6.5.2 Basis constraint and Tikhonov regularization with **a priori** *knowledge*

Vauhkonen regularized the EIT problem for the thorax, based on anatomical information (Vauhkonen, Kaipio et al. 1997; Tidswell, Gibson et al. 2001a) gained from MRI. The conductivity distribution was approximated as a summation of weighted basis functions. A covariance matrix was then constructed from a learning set of feasible conductivity distributions and was broken down, using principal component analysis, into eigenvectors and corresponding eigenvalues. When displayed, the eigenvectors appeared to model the different compartments of the thorax, the lungs and the heart so that the coefficients of the basis functions had a direct physiological interpretation.

However, the technique gave unreliable results when the prior information was incompatible. Subsequently, Vauhkonen (1998) penalized each iteration of a solution by its distance from the *subspace* S_w spanned by the basis functions, drawing it towards rather than forcing it to be in the subspace, as in the *basis constraint method*. In this case, as opposed to the identity matrix, the regularization matrix L is built so that its null space is the subspace S_w. The technique was shown to give reasonable results even when the prior information was incompatible.

1.6.5.3 Anisotropic smoothness constraints

Kaipio *et al.* (1999) implemented Tikhonov regularization using a regularization matrix into which approximate spatial prior information is incorporated. They showed that, by using anisotropic smoothness constraints there were improvements over Tikhonov-based 2-D

reconstructions using the identity matrix and that images were no worse when the *a priori* information was wrong. Borsic performed similar reconstructions using Gaussian anisotropic filters and found that conductivity patterns could be reconstructed even if they violated the prior information (Borsic, Lionheart et al. 2002).

1.6.6 Summary

In most linear reconstruction methods, the conductivity change is found by a single matrix operation on a vector of measured data. Backprojection methods have been used in 2-D but 3-D linear methods are based mainly on the Moore-Penrose inverse of a sensitivity co-efficient matrix (Jacobian) using SVD.

Non-linear iterative methods have been employed for many solutions of 2-D problems. These become very computationally expensive when the 3-D problem is tackled. The inclusion of prior information appears to be of great benefit in directing non-linear iterative solutions towards a likely solution, particularly when there are identifiable physiological compartments within the part of the body under consideration.

Reconstructions in this thesis will be made using a linear, non-iterative, truncated SVD algorithm since the focus is not on the inversion process but on the difference made to images by improvement of the forward solution.

1.7 Modelling in EIT

This section describes the models that have been used in all aspects of EIT, in particular for reconstruction of brain images. It will be shown, using examples from EIT and EEG modelling, that a 3-D model must be used and that non-sphericity and inhomogeneity, due to the layered nature of the head, produce an as yet unquantified effect on reconstructed EIT images of tank and human data.

1.7.1 2-D models

1.7.1.1 General reconstruction

Sections 1.3 and 1.4 describe the use of EIT for many applications in medical imaging. In order to generate a Jacobian for image reconstruction, it is necessary to calculate $\nabla\Phi$ and $\nabla\Psi$, knowing something about the pattern of current being applied and making assumptions about the shape of the object under consideration and about its internal conductivity distribution σ.

In many cases of image reconstruction of thoracic or gastrointestinal images, electrodes were arranged in a plane and a 2-D model was used to approximate the internal fields when a single plane of electrode was used for measurement. This was done using analytical and FEM models of a circular conductor (Avis 1993; Avis and Barber 1994; Metherall, Barber et al. 1996; Patterson, Zhang et al. 2001), and of a plane conductor with a more realistic boundary shape (Jain, Isaacson et al. 1997; Borsic, McLeod et al. 2001). The latter was found to reduce distortions markedly when data was obtained from a non-circular boundary. The 2-D model was extended to 2½-D in reconstruction of data from a cylindrical tank, assuming axial uniformity (Jerbi, Lionheart et al. 2000) where stacked slices were assumed to be circular, uniform conductors. Results showed improvements over strictly 2-D methods. 2-D circular models have also been used in general to reconstruct breast images (Kerner, Paulsen et al. 2002) although they suggest that a 3-D approach is needed to increase sensitivity to deep lesions.

1.7.1.2 Models of the head

2-D models have also been used in the reconstruction of brain images. Boone used the Sheffied backprojection algorithm (Barber and Seagar 1987) to reconstruct images of spreading depression in the rabbit cortex (Boone, Lewis et al. 1994). This assumed that the resisitivity distribution was initially homogeneous and 2-dimensional, as is the flat cortex of

the rabbit brain. Bayford used a 2-D algorithm based on backprojection for reconstruction of data from a 2-D phantom with a circular, Plaster of Paris ring to simulate the presence of a skull (Bayford, Hanquan et al. 1995). Gibson *et al.* (2000) suggested a 2-D circular FEM solution to model impedance changes in the centre of the neonatal head and their resultant boundary voltage changes, but did not actually perform any reconstructions with this model. The problem of stroke detection and monitoring was approached by Clay and Ferree (2002) using a circular FEM with four concentric regions representing brain, CSF, skull and scalp, as did Gibson *et al.*. Images were reconstructed using an iterative approach and high correlation was shown between simulated and reconstructed impedance changes.

Pidcock *et al.* presented a formulation of rectangular, circular and elliptical analytic and semi-analytic solutions for the problem of EIT, including, in each case, the presence of layers (Pidcock, Kuzuoglu et al. 1995). No reports have been made of the models' implementation.

1.7.2   3-D models

1.7.2.1   General reconstruction

Since current is not confined to 2-dimensions in a 3-D object, it is more appropriate to employ 3-D models in a reconstruction algorithm for such medical applications as have been described above. Pidcock *et al.* also presented a formulation of cubic, cylindrical and spherical analytic and semi-analytic solutions for the 3-D problem of EIT, and, as for the 2-D case, included in each case the presence of layers (Pidcock, Kuzuoglu et al. 1995). Again, no reports were made of the models' implementation.

Analytical and FEM-based 3-D models .have been applied for imaging resistivity perturbations in cylindrical simulations and phantoms (Blue, Isaacson et al. 2000; Kleinermann and Avis 2000; leHyriac and Pidcock 2000; Vauhkonen, Vauhkonen et al. 2000; Kleinermann 2001) and static and dynamic images have been obtained of the human thorax during respiration (Saulnier, Blue et al. 2001) using several planes of electrodes. Blue concluded from his results that, for a system with a given number of channels, it is best to divide the electrodes among several planes rather than increasing resolution in a single plane by placing all of them in a dense ring. In the latter case, he reports a larger artefact than in the former due to impedance perturbations occurring outside the image plane. Kleinermann reported, from inspection of singular values, that the 3-D reconstruction algorithm appeared to be better conditioned than the 2-D algorithm. He also modelled an elliptical cylinder but reconstructed images were not presented.

1.7.2.2   Models of the head

There are several examples of 3-D models used to reconstruct EIT images of the head. The analytical models approximate the head as a sphere only and FEM models as a sphere or a realistic, head-shaped geometry.

1.7.2.2.1   Spherical and homogeneous models

Our group at UCL has previously produced images of resistance changes in hemispherical and head-shaped phantoms and in the head, during brain function, using a 3D analytical forward solution for a homogeneous sphere (Gibson 2000; Tidswell, Gibson et al. 2001b). Both these studies showed that, in the presence of a real or simulated resistive skull, the homogeneous algorithm reconstructed impedance changes too centrally, suggesting the need to take the skull into account in future algorithms. In the head-shaped tank, a 12% resistance change was localized with an error of 6-25mm without the presence of the skull and 19.6-36mm with the skull in place. In the hemispherical tank, the mean value for peak impedance change inside a simulated skull was 34% that of the change without the presence of the skull and the localization error was 6.5-20.3mm. Localization accuracy was similar for reconstructions from tanks with and without the simulated skull when a radial correction factor of 1.6 was introduced.

The perturbation approach (section 1.6.3.3) was employed by Morruci et al. (1995) to reconstruct an off-centre perturbation in an otherwise homogeneous sphere. A direct sensitivity matrix was produced, using BEM, for a square grid describing the upper hemisphere and 40 electrodes arranged in rings from its equator to its apex.

1.7.2.2.2   Spherical and inhomogeneous models

There are two examples of the use of analytical, layered sphere models in the literature. The solution for potential was derived by Ferree et al. (2000) for injection of current I through point electrodes on a four-shell sphere in order to estimate the regional head tissue conductivities in vivo. A similar method was employed by Goncalves et al. (2000) in order to better specify regional head conductivities when solving for the EEG problem, but their analytical model included only three layers. Neither papers reported reconstruction of images.

Another spherical model of the head was produced by Towers et al. (2000). They used the Ansoft Maxwell FEM package to solve for one hemisphere of a sphere consisting of 4 concentric shell layers, scalp, skull, CSF and brain with a ring of 16 scalp electrodes attached around its equator. They did not produce images but showed the requirements of voltage

measurement sensitivity to be 100-120 dB in order to detect changes in rCBF and those due to application of a carotid clamp. They also compared their results with those from a 2-D model, which indicated sensitivity requirements 15 dB less severe than did the 3-D model.

1.7.2.2.3 Realistic geometry and inhomogeneity

A FEM model of a 4-compartment, realistically-shaped head was used by Gibson (Gibson 2000) in a truncated SVD algorithm to reconstruct images from tank data and human evoked responses. In neither case were reconstructions significantly better than when an analytical spherical model was used, but he suggested that errors in the mesh may have substantially reduced the accuracy of the FEM-generated sensitivity matrices and hence reduced the benefits of including realistic geometry and inhomogeneity in the forward model. Images were reconstructed iteratively by Polydorides et al. (2001) from simulation of a visual evoked response using a similar FEM model on an improved mesh with 5 compartments and electrodes arranged in a ring. Their results will be discussed further in Chapter 4.

In a further study, the change in transfer impedance was studied for a 30-40% impedance change due to a 10cm^3 central oedema, as simulated by a FEM model with realistic head geometry, including 13 different tissues and using hexahedral elements (Bonovas, Kyriacou et al. 2001). However, no images were presented using this technique.

A solution for current flow through a realistically shaped head was reported by Bayford et al. (2001), using *integrated design engineering analysis software (I-DEAS)*. A full sensitivity matrix was not built, however, and no images were reconstructed.

1.7.3   Modelling in EEG

Whilst EIT is an active technique, in that current is injected into the head, EEG is a passive technique. Nonetheless, the problem of dipole modelling in EEG is similar to that in EIT because it is necessary to calculate distributions of potential and of electric field inside the head as if current was being injected. The non-sphericity and inhomogeneity of the head present similar problems. Three- and four-shell models are often used in source localization from measured EEGs (Rush and Driscoll 1969; Ary, Klein et al. 1981; Yvert, Bertrand et al. 1997; Krings, Chiappa et al. 1999; Mosher, Leahy et al. 1999; Cuffin and Schomer 2001). Mostly, multi-shell models have included three shells only, neglecting the CSF, which is expected to shunt some of the injected current. In the past, spherical models have been compared with non-spherical models and homogeneous with non-homogeneous. Some of the results of these comparisons follows.

1.7.3.1   The effect of shells

Ary quantified the difference between analytical solutions for potential generated by a dipole in 1) a homogenous sphere with conductivity that of brain and 2) a system of three concentric shells, brain, skull and scalp, each with appropriate conductivity. The latter suggested that a radial correction factor of about 1.6 could compensate for the presence of the skull and the resultant localization error when a homogenous model is used.

1.7.3.2   The effect of geometry in the presence of shells

Many workers have compared the use of spherical and non-spherical models for localising dipoles within non-spherical objects. Simulation studies, such as that by Roth (1993), showed average and maximum localization errors of 19.7mm and 40mm when dipoles were simulated in the frontal and temporal lobes of a realistic BEM model and reconstructed using a 3-shell sphere mode. Yvert (1997) performed a similar calculation for 2000 simulations of dipoles at random positions on the segmented cortical surface of a realistically-shaped, 3-shell BEM model. Localization errors for inverse calculations with a spherical model were reported to be 5-6mm in the upper part of the head and 15-25mm in the lower part. Cuffin (2001) investigated two features of non-spherical geometry in the head, the general boundary shape and the *brain pan*, which is the very non-spherical surface at the bottom of the brain cavity. Inverse calculations were performed using an analytical 3-sphere model and data was generated using 3-shell, non-spherical BEM models with and without a *brain pan*. It was found that the maximum localization errors were approximately 10mm in the former and 20mm in the latter.

The same author reported localization studies of 177 dipole sources created by injecting current into depth electrodes implanted into the brains of 13 human subjects. Using a 3-layered sphere model for the inverse calculation, the best average localization that could be achieved was 10mm. In a similar study, Krings *et al.* (Krings, Chiappa et al. 1999) used a 4-shell spherical head model to localize 11 dipoles in only 2 subjects. Localization errors were 17mm and 13mm using 21 electrodes and 41 electrodes respectively, when a proportionality correction factor was applied to correct for non-spherical head shape. Errors were 23mm and 17mm when the factor was not applied. In the latter study, electrodes were implanted and anchored with metal skull screws. In the former, anchors were non-conductive.

In order to study the effect of realistic geometry in correct physiological localization of the source associated with somatosensory evoked potentials (SEPs), Kristeva-Feige *et al.* (1997) performed 9 daily replications of a right median nerve stimulation experiment on one

healthy subject. A 3-shell spherical model and a 3-compartment realistically shaped BEM model were used for the inverse calculations and both located the dipole sources, correctly, within the postcentral gyrus when results were projected onto the individual's MRI and compared with an fMRI image during the same stimulation protocol.

1.7.4   Anisotropy

A further problem in both EIT and EEG is that the tissue inside the head is highly anisotropic, in which case, it is possible that no isotropic conductivity distribution could accurately predict the measured data (Lionheart 1998). Data measured from a real-skull phantom head was reconstructed by Baillet *et al.* (2001), who suggested that full, anisotropic realistic head FEM models were necessary, rather than spherical models to fit the data with a reasonable level of residual variance. They suggested that an analytical spherical model, while not as good as the detailed FEM model, produced better results than simpler FEM and BEM models with realistic geometries but less conductivity constraints.

In order to include anisotropy information in a FEM model of the head, conductivity tensor data could be provided by diffusion weighted tensor MRI, which is sensitive to the freedom of water molecules to diffuse in different directions through tissue. Haneisen *et al.* (2002) found a minor influence of anisotropy on source localization but a major influence on source strength estimation when tissue anisotropy was considered in localization using computer simulated data. The effect of anisotropy is not investigated in this thesis.

1.7.5   Summary

In EEG inverse dipole modelling using spherical models, neglecting to include shells in the inverse calculation results in sources localized too centrally when data is from a shelled object. The inclusion of shells corrects for this. Similar mislocalizations were found in EIT images of impedance changes within a shell in a spherical phantom when a homogeneous reconstruction algorithm was used.

Simulated dipoles in realistic head models are localized best when realistic geometry is assumed in the inverse calculation but the inclusion of real geometry in EEG modelling has not been shown to improve significantly the localization of dipoles in real heads. This could be for a number of reasons, including inaccurate knowledge of tissue conductivities, anisotropy information and individual geometry. Given the conclusions of Baillet *et al.* (2001) it is reasonable to ask whether FEM will give any improvement in EIT reconstruction

of head images over a shelled sphere model unless it is pushed to its limit and includes all of this patient-specific information.

1.8   Statement of Objectives

It is my aim to develop and investigate the possible use of an analytical multi-shell sphere algorithm in EIT reconstruction of human images. I shall compare its efficacy with that of algorithms based on a homogeneous sphere model, a homogeneous, linear FEM model with realistic-geometry and one that includes four internal tissue compartments. Finally, I shall present a mathematical model of the small impedance change that occurs in neuronal tissue during depolarization and comment on the ability of EIT to produce images of such a change.

1.9   Design

In Chapter 2 will be described the analytical and FEM methods used in this thesis as will the particulars of the reconstruction method used.

Chapter 3 describes inclusion of multiple shells in an analytical EIT image reconstruction algorithm and reconstruction of computer-simulated and tank data from a multi-shell spherical object. Results are compared with those using a homogeneous algorithm in order to assess the improvement due to the new algorithm. To investigate the ability of a linear FEM to take into account thin shells of high resistivity contrast, results are compared also with those using a linear FEM algorithm for a multi-shell sphere.

In Chapter 4, FEM models are used to investigate the effect of including realistic geometry in the reconstruction algorithm. Data is reconstructed from homogeneous and shelled tanks with realistic head geometries and reconstructions are performed using spherical and non-spherical, homogeneous and inhomogeneous models. These algorithms are also applied to the reconstruction of human images in order to assess how much better it is to include shells and realistic geometry in a reconstruction algorithm for human brain function.

In Chapter 5, a model will be presented of the microscopic impedance changes associated with neuronal depolarization. Predicted changes from the model will be included as perturbations in the macroscopic models developed for the head in order to estimate the expected scalp signal and assess the feasibility of their reconstruction.

Image Reconstruction using Analytical and Numerical Methods

2 Image Reconstruction using Analytical and Numerical Methods

2.1 Introduction

It is necessary in EIT to describe current flow as accurately as possible but, to my knowledge, an analytical multi-shell concentric sphere model has not been implemented before in an EIT reconstruction algorithm. It seems reasonable that an improved model of current flow will reduce localization error in the resulting images. I have therefore applied an analytical model of current flow in concentric spheres to the problem of EIT image reconstruction. The model assumes the head to be four concentric, spherical shells of different conductivity representing brain, cerebro-spinal fluid (CSF), skull and scalp.

2.1.1 Purpose

In this chapter, I will 1) describe and compare the implementation of analytical and linear FEM-based numerical methods in order to solve the forward problem in EIT for homogeneous spheres and those with concentric layers of contrasting resistivity; 2) describe the inversion process which will be used for EIT image reconstruction from computer simulations and laboratory phantoms. Comparison of image reconstruction using numerical and analytical methods will be left until chapter 3 when the effect is investigated of the presence of shells on EIT images.

2.1.2 Modelling the Forward Problem

2.1.2.1 Analytical and Numerical Methods

Some justification is necessary for the pursuit of analytical methods in this study when it is clear that a sphere is only an approximate representation of the head. One of the most commonly used methods of solving the forward problem is the numerical Finite Element Method (FEM) in which a given volume is divided up into tetrahedral elements and the potential distribution is approximated throughout by polynomial functions within each element. Ultimately a realistic FEM model of the human head (Bayford, Gibson et al. 2001) will give a more faithful representation of the current distribution than would either of the analytical, spherical models suggested.

69

Meshes are relatively easy to generate but it is difficult to provide solutions for electrical potential throughout without a mesh of good quality, which is less easy to generate. Solutions of the forward problem using the FEM are dependant on the type of elements, the degree of interpolation function and the type of solver used. An analytical solution is not dependant on these factors. The FEM has difficulty modelling very thin layers without resorting to the use of extremely fine meshes, which increases computation time considerably. The problem of thin layers exists in both simple shell geometry and that which accurately models the geometry of the compartments in the head. Currently our group is working to develop both FEM and analytical reconstruction. The analytical reconstruction is intended as a check on the FEM solution and a possible alternative.

2.1.2.2   Elemental, Nodal or Voxel

In 2-D and 3-D analytical and numerical methods, conductivity and sensitivity coefficients can be defined for each element of a mesh (Murai and Kagawa 1985; Kleinermann 2001; Polydorides and Lionheart 2001; Vaukhonen, Lionheart et al. 2001), for each node (Arridge, Hebden et al. 2000) or for each pixel or voxel (Morucci, Granié et al. 1995; Gibson, Tidswell et al. 1999; leHyriac and Pidcock 2000; Mueller, Isaacson et al. 2001). For a given mesh, there are many more elements than nodes so a nodal sensitivity matrix is smaller and reconstruction is less ill-posed. The density of elements, nodes or voxels can be chosen at will.

In order to discretize Geselowitz's sensitivity relationship (section 1.6.2.2), it is assumed that both electric field and conductivity are constant in the volume represented by the sensitivity coefficient, whether calculated for an element, a node or a voxel. Therefore, it is desirable for that volume to include one type of tissue only when contrasting tissues exist within the whole, as in the case of the head.

2.1.2.3   Electrodes

Many algorithms have suggested the inclusion of electrode models in the solution of the forward problem (Cheng, Isaacson et al. 1989; Hua, Woo et al. 1993; Vauhkonen, Kaipio et al. 1997; Dehghani 1999). In practice, scalp electrodes have a finite area and present a complex impedance in series with that of the head alone. Analytical solutions have accounted for the former consideration (Pidcock, Kuzuoglu et al. 1995; Kleinermann 2001) but previous analytical reconstructions of human data have assumed current injection to be through *point electrodes* which present no contact impedance (Gibson 2000).

2.1.2.4   *Spatial Sampling on the Head*

In order to sample as much of the head as possible, Gibson (Gibson 2000) devised a set of positions for scalp EIT electrodes based on the 10-20 system in EEG (Binnie, Rowan et al. 1982). 12 more electrodes were added so that, in total, 31 were used. When these positions were used to produce images of spherical computer simulations, all but four were on or above the equatorial plane of the sphere. It was proposed (Bayford, Boone et al. 1996) that sensitivity is maximized to central changes when current is driven through electrodes at opposite sides of the object *(polar drive)* or when a trigonometric pattern is used for injection through many electrodes (section 1.5.1). Based on the principle of *polar current drive*, a list of 258 4-terminal measurements was devised (Gibson 2000) using 21 different pairs of electrodes for polar or near-polar injection and 38 different pairs of adjacent electrodes to measure potential difference.

High-density EEG employs N_e=64-128 electrodes. If spatial resolution is proportional to $M_m^{-1/3}$, where M_m is the number of measurements, and M_m=$(N_e/2)(N_e-3)$ for polar drive (Clay and Ferree 2002) then, using 31, 64 and 128 electrodes would produce resolutions of 1 : 1.6 : 2.6 relative to each other. Application of electrodes is time consuming but some studies have been carried out to investigate the use in EIT of nets and caps specially designed for EEG and containing many electrodes in preordained positions. For the purposes of studies in this thesis, only 31 electrodes were used.

2.1.3   The Finite Element Method (FEM)

2.1.3.1   *The Choice of FEM as Opposed to BEM*

The boundary element method (BEM) is a numerical method often used in EEG inverse dipole modelling and has been used in the past for EIT reconstruction as well (Morucci, Granié et al. 1995). However, for BEM, all internal regions must be isotropic, piecewise homogeneous and continuous, requirements which are not met in the case of the head, which is highly anisotropic and in which there are large discontinuities such as *sutures* and holes in the skull. FEM is capable of modelling these (Thevenet, Bertrand et al. 1991) and was therefore chosen in this work for EIT reconstruction of head images.

Previously, this group (Gibson 2000) compared results using an analytical model of the head as a homogeneous sphere, a FEM model of the head as a homogenous sphere and a FEM model of the head with a realistic geometry and internal resistivity distribution, albeit isotropic. The voltages were calculated for every four-terminal measurement in a protocol list for each case and then compared. This produced *voltage profiles*. Both spherical models were expected to return similar results but this was not found. The quality of the mesh was suspected but the cause of these discrepancies still needs to be resolved. This problem will be investigated using new meshes generated by Integrated Design Analysis Software (I-DEAS: a commercial software package designed primarily for use in stress and thermal modelling) (Bayford, Gibson et al. 2001) and a new version of the FEM solver, TOASf (http://www.medphys.ucl.ac.uk/~martins/toast/index.html), used in Gibson's study and described in section 1.6.4.4.

2.1.3.2   *How the FEM works*

2.1.3.2.1   *Mesh Generation*

In order to use FEM, the volume under consideration must be divided into discrete elements. An example of the use of hexahedral elements can be found in the work of Bonovas *et al.* (2001) but they are usually tetrahedral. There are various methods to generate a tetrahedral mesh to describe a given volume such as *Octree, Delauney* and *Advancing Front*. By the latter method, the surface of the object is represented as a 2-D triangular mesh and tetrahedra are grown inwardly throughout the volume until it is all meshed.

It has been suggested that, once the mesh has been generated, it is useful to refine it so that the it is of higher density near regions of high field variation, such as near electrodes and

near internal tissue boundaries (Molinari, Cox et al. 2001; Molinari, Cox et al. 2002) and of lower density elsewhere. A higher density mesh produces a more accurate numerical solution for field distribution. The refinement method increases the accuracy of the numerical approximation without requiring a high-density mesh throughout the volume and, therefore, increases the efficiency of a FEM algorithm by reducing computational time and storage requirements.

The mesh used previously by Gibson (2000) for FEM reconstruction was produced by the University of Utah using a method based on Delauney triangulation. It was found, however, that, relative to the largest elements, some elements were very small and others were long and thin. This was thought to introduce errors in the sensitivity matrices. The suitability of I-DEAS for mesh generation and the possibility of solving the forward problem in EIT of the human head have been considered previously (Bayford *et al* 2001). With this software, higher quality meshes can be generated and so its use is likely to reduce errors. The mesh generation is based on an advancing front algorithm and meshes can be constructed from linear or quadratic, tetrahedral elements.

2.1.3.2.2 Discretization - Support

A good forward model must describe accurately the distribution of current and potential throughout the head upon current injection through scalp *drive* electrodes. It must also describe accurately the sensitivity relationship between an internal conductivity change and the associated voltage change measured at the *measure* electrodes. The former is often tested by comparing relationship [1-14] (in which the discretized conductivity distribution is related to the measured voltages by the discretized sensitivity matrix) with the potentials calculated directly and analytically. It is normally found that finer discretization produces a more accurate numerical solution for potential throughout the volume and also a more accurate prediction of the boundary voltages V in equation 1-14 whether by use of a numerical or an analytical sensitivity matrix (Dehghani 1999). However, the larger the number of elements, the more computationally expensive is the FEM solution and the larger the sensitivity matrix becomes.

The FEM can produce solutions for field on an elemental basis after calculation of potential at each of the nodes (Murai and Kagawa 1985; Bayford, Gibson et al. 2001; Kleinermann 2001) or it can calculate the field on a nodal basis as does TOAST (Arridge, Hebden et al. 2000). Other methods calculate field at the centre of a cubic or cylindrical voxel, as described above. For purposes such as calculating the gradient of potential and

discretising the sensitivity relationship, it is necessary to define the volume represented by each sensitivity coefficient. This is equal to the volume over which the integral in [1-9] is evaluated, and will be referred to as the *support* or v_e. For an elemental solution, that is simply the volume of the element and for a voxel-based solution, the volume of the voxel. In the latter case, many authors ignore support since it is the same for each coefficient (Morucci, Granié et al. 1995; Gibson 2000). For a nodal solution, the volume is not so obvious and *complementary elements* have been suggested, extending half-way along the edges of each of the elements to which that node belongs (Dong, Bayford et al. 2003). Also used as support could be the summed volume of all the elements to which that node belongs. This approach is adopted here.

2.1.3.2.3 Degree of Interpolation

A FEM model can assume that potential varies as a polynomial function from point to point within an element. For each of the elements in a mesh an *interpolation function* (or *basis function*) is suggested and a summated series of these can be used to approximate the solution to the entire model. These functions can have any degree but it is most common only to use *linear* or *quadratic* functions. For the latter technique, extra nodes are added at the midpoints of each element edge. Increasing the number of linear elements will improve the linear solution but, in practice, a quadratic solution will be more accurate than a linear solution for the same number of elements, especially in regions of high field variation.

2.1.3.2.4 Solution

A full description of the formulation of the system of equations in FEM is outside the scope of this thesis. However, the interested reader may wish to consult Jin (1993), who describes its use in the solution of electromagnetic problems for 1-D, 2-D and 3-D cases. In a domain Ω, the problem can be described as

$$\Im \phi = f$$

[2-1]

where $\Im$ is a differential operating matrix, dependent on the properties of the system, f is the excitation or forcing function and ϕ is the unknown function e.g. potential. The book describes the Ritz (or Rayleigh-Ritz) and Galerkin methods to approximate the solution. The former is a variational method in which a variational expression is minimized with respect to its variables, giving a differential matrix whose elements depend on the chosen interpolation

functions. The latter is a weighted residual method and derives a similar system of equations dependent on the interpolation functions.

2.1.3.2.5 Implementations

A thorough review of available FEM packages was carried out by Gibson (Gibson 2000) with an aim to choose one for use in EIT. These were mostly sophisticated, inflexible pieces of software and it was difficult to see how they could be adapted in order to solve for the 59 different boundary conditions described in section 2.1.2.4. EEG source modelling software, like ASA (Advanced Source Analysis, ANT Software BV, Enschede, The Netherlands) and CURRY (Neurosoft, Inc., Sterling, USA) was disregarded because it was based on BEM models of the head. More recently, CURRY has developed FEM meshing and solving capabilities but this was not considered for studies in this thesis. Neither were the solutions provided by I-DEAS used, although I wrote a macro which produced 10 consecutive solutions for 10 different boundary conditions. At this point, however, the demands on memory became very high.

Gibson used the TOAST software developed at UCL, which solves for photon density throughout an object when light is injected at one optode on the surface. The scattering of light is comparable to resistivity but there is no analogue in EIT to the concept of absorption. However, photon density and the diffusion coefficient were substituted for the electric potential and conductivity, and the absorption coefficient set to zero in order that the diffusion equation became identical to Poisson's equation. The refractive index was set to one in order to prevent refraction and reflection at internal tissue boundaries. In order to solve for current injection through a pair of point electrodes, Robin boundary conditions were applied (a combination of Dirichlet and Neumann conditions described in section 1.6.1.2) to obtain a solution for injection of light at one optode and this was subtracted from a separate solution for light injection at the other. Nodal values for intensity were translated onto a pixel basis, as in section 2.1.4.1, and the gradient was calculated in 3-D in order to build the sensitivity matrix. This was then smoothed and normalized as described in section 2.1.4.2.

He obtained better, reconstructed images with a low-resolution, quadratic FEM than with a high-resolution, linear FEM but the latter appeared to localize impedance changes less accurately than did an analytical sphere model. Regions of negative photon density were found in both the FEM solutions for light injection through one optode. This is physically impossible and it was suggested that these errors were due to the poor quality of the mesh. The ratio of largest-to-smallest element volume was 40000 for the high resolution mesh and

170000 for the low resolution mesh. Also present were long, thin elements in which voltage variation cannot be modelled accurately as a quadratic function, particularly near to the electrodes. His work emphasised the need for a mesh of high quality in order to produce accurate solutions.

More recently, the UCL group received a version of TOAST written in Matlab for 2-D and 3-D problems and incorporating boundary conditions appropriate for the case of EIT. This code, referred to as MaTOAST, had been tested in the 2-D case but it was left to this group to test it in the 3-D case. MaTOAST was used to produce solutions in the following work and its nature will be described in section 2.2.1.4.

Preliminary results were submitted a year ago, and are currently in press, which showed the first reconstructions using sensitivity matrices produced on I-DEAS-generated 3-D meshes (Bagshaw, Liston et al. In press). The MaTOAST solution produced more realistic voltage profiles than those reported by Gibson (Gibson, Bayford et al. 2000) and images were produced from computer simulated data, tank data and human data. The reconstruction algorithm differed from that described below in several key aspects, namely the matrix normalization method and the implementation of post-weighting. These are described in sections 2.1.5.2 and 2.1.5.3 and enable fair comparison to be made between numerical and analytical reconstructions. Using the algorithm described by Bagshaw *et al.* (In press), it was not possible to produce reasonable images using the analytical shell model. The algorithm described below allows reasonable images to be reconstructed using both techniques.

2.1.4 The Analytical Method

2.1.4.1 Building a sensitivity matrix for a homogeneous, spherical head

The head has previously been approximated as a homogeneous sphere and a reconstruction algorithm developed and validated, based on this model (Gibson, Tidswell et al. 1999; Gibson 2000; Tidswell, Gibson et al. 2001a; Tidswell, Gibson et al. 2001b). In order to generate the sensitivity matrix, the upper hemisphere of a homogeneous sphere was discretized into six horizontal planes of square pixels. The diameter of the equatorial plane was 32 pixels. Therefore, each sensitivity coefficient represented a voxel of dimensions approximately 6 x 6 x 15mm. In order to calculate the field, Gibson differentiated the solution for potential

$$V(\mathbf{x}) = \kappa \left[\frac{2}{r_a} - \log(1 - \mathbf{x} \cdot \mathbf{a} + r_a) \right] - \left[\frac{2}{r_b} - \log(1 - \mathbf{x} \cdot \mathbf{b} + r_b) \right] \qquad [2\text{-}2]$$

where electrodes at **a** and **b** were at distances r_a and r_b from a point **x** within the sphere. He calculated the 21 drive and 38 measurement fields, analytically, at the centre of each voxel and their scalar product was taken (see section 1.6.2.1) for the 258 appropriate combinations of field distributions. These were considered to be the values of sensitivity representative of the entire voxel ($\rho = 1\Omega m$) when, for each measurement, a current of 1A was injected through point electrodes A and B on the surface of a unit sphere and potential difference measured between point electrodes C and D (see section 1.6.2.1).

Kleinermann (2001) calculated the electric potential at the nodes of element in a 2-D slice through a 3-D cylinder and approximated the field throughout the element using interpolation functions in the same fashion as did Murai et al. (1985). For this reason, his algorithm may be thought of as quasi-analytical, but, since the value is a discretization of a volume integral over the whole element, that value he calculated as representative of the element may be more suitable even than that calculated from the analytical value of $\nabla\Phi$ at the centre of the element. Another way to derive the sensitivity coefficient would be to sum values of $\nabla\Phi_e^n$. $\nabla\Psi_e^n$, calculated analytically at n points, evenly distributed throughout the element and multiply the total by $v_e/(I_\phi I_\psi n)$. Finally, the continuous integration could be evaluated over the volume of the element but it is not obvious that this extra computational expense would benefit the reconstruction algorithm.

2.1.4.2 *Smoothing and C-normalization*

A further step, introduced by Gibson, was to smooth the sensitivity matrix by making each coefficient equal to the mean of itself and its eight neighbouring coefficients. This appeared to smooth steep changes near electrodes without affecting the images elsewhere. Documentation of this process was not found in other literature. Finally, Gibson C-normalized the sensitivity matrix as described in section 1.6.2.4.

2.1.5 Reconstruction of Images

2.1.5.1 Truncated SVD

Only one method of inversion was considered in this thesis, since the emphasis is on improving the accuracy of the forward solution. Sensitivity matrices were constructed and inverted using the truncated SVD (TSVD) or Moore-Penrose method section 1.6.3.4.2. In the past, the UCL group has used this method in order to reconstruct images of computer simulations, tanks and human evoked responses. In those studies, choice of truncation was based mainly on localization accuracy and resolution when the position of the impedance change was known and mainly on visual criteria and noise considerations when it was not known, as for human experiments. Xu (1998) described the difficulties in setting criteria for the choice of truncation in SVD methods to solve linear ill-posed problems. Criteria such as F-statistic, the L-curve and a quality-based Mean Squared Error (MSE) were discussed. Choice of truncation level has a significant effect on the quality of images and on the localization of impedance changes so it is very important, when comparing two algorithms, to set truncation criteria to the detriment of neither method.

2.1.5.2 R-Normalization

It was mentioned in section 1.6.2.3 that images published previously by this group were reconstructed from normalized or percentage-difference data (Gibson 2000; Tidswell, Gibson et al. 2001a; Tidswell, Gibson et al. 2001b). It is necessary in this case to pre-multiply the sensitivity matrix by a row-normalizing matrix R whose diagonal is the inverse of the predicted or measured data. However, whilst they pixel- or column-normalized the sensitivity matrix in order to suppress the artificially high sensitivity calculated near the electrodes, pre-multiplication by R was not performed, an omission which might have led to increased errors. In other work submitted by this group (Bagshaw, Liston et al. In press), pre-multiplication was performed but the diagonal of R was not the inverse of the predicted data but the inverse of the root mean square (rms) of each row of the sensitivity matrix. It is not clear how exactly this difference might affect the result but this technique has been avoided in the studies described below.

2.1.5.3 Post-Weighting and Uniformity

In these studies, Gibson's algorithm was more sensitive to an impedance change at the edge of the image. In order to correct for this, he divided the reconstructed image into 16

conccntric spherical shells and invented a radially dependent factor by which each could be divided. This way, the amplitude of the peak impedance change remained more constant when an object moved from the centre to the edge. It is unclear what modification might be required for this correction when the conductivity in the objcct varies from one radius to another as in the case of spherical shells. It is also unclear as to how this correction could be introduced in the case of a non-spherical image such as that produced by a realistic head-shaped FEM.

Kotre (1994) pixel-normalized the sensitivity matrix in a similar way to Gibson and also applied a radially-dependant filter to the resulting image. Clay *et al.* (2002) introduced a weighting scheme in which they column-normalized the sensitivity matrix before inversion but also "column-normalized" the resulting image. They produced impedance data

$$\Delta \mathbf{Z} = (\mathbf{AW})(\mathbf{W}^{-1}\Delta\sigma)$$

[2-3]

initially, where $\mathbf{W} = \mathrm{diag}(w_n)$ and

$$w_n = \left[\sum_{m=1}^{M} A_{mn}^2 \right]^{-1/2}$$

[2-4]

Their subsequent solution was written as

$$\Delta\sigma \approx \mathbf{W}(\mathbf{AW})^{+}\Delta\mathbf{Z}$$

[2-5]

Given impedance data from a tank, this is similar to reconstruction of difference data (as opposed to normalized data) by inversion of Gibson's C-normalized sensitivity matrix with the image uniformity correction replaced by a second C-normalization. This post-weighting was not included in the algorithm used for recent work submitted by this group (Bagshaw, Liston et al. In press). Its use may be of grcat advantage in further reducing electrode artefact since changcs near the clectrodes are heavily penalizcd.

2.1.6   Summary

The analytical and the linear and quadratic finite element methods have been employed by the UCL group, and others, to reconstruct EIT images from measured and computer simulated data. Various methods were described above in order to discretize the volume under consideration. Also described were techniques to compensate for inadequacies in the forward models, namely smoothing and normalization. These reduced the effect of the artificially high current density calculated near electrodes due to the assumption of point electrodes in the model.

In order to compare the use of different analytical and numerical forward models in reconstruction, it is necessary to impose a level playing field. In the following section will be described the implementation of FEM and analytical methods for reconstruction in this thesis. This has been devised in order that comparison of reconstructed images reflects genuinely the effects of different forward models rather than a difference in any other aspect of the reconstruction algorithm when incorporating these models. Discussion will be limited to implementation for the spherical models to be used in chapter 3. Its extension to realistic geometry will be described in chapter 4.

2.2   Methods

2.2.1   The Forward Problem

2.2.1.1   The Physical Models

In each of the models, it was assumed that current was injected and voltage measured by point electrodes on the surface. The current injected was constant and so Neumann boundary conditions were imposed.

The homogeneous spherical models had an outer radius of 100 mm (Figure 2-1(i) and (v)). In the 4-shell model, the shells had outer radii (conductivities) of 80 mm (0.25 Sm^{-1}) for the brain, 82 mm (1.79 Sm^{-1}) for the CSF, 87 mm (0.018 Sm^{-1}) for the skull and 92 mm (0.44 Sm^{-1}) for the scalp (Burger and Milaan 1943, Geddes and Baker 1967, Baumann et al 1997). These values fell within the range of values listed in section 1.4.1 and were used by Ferree et al. (2000) in their study to estimate head tissue conductivity. Use of the same values enabled comparison of my surface potential results with those of their group.

For sensitivity matrices generated to reconstruct tank images, the shell models included only 3 contrasting, concentric regions. This was because it was not viable to construct a tank that had a fourth layer to simulate CSF. The head *phantom* consisted, instead, of a spherical volume of conducting fluid in which was suspended a highly resistive, spherical shell to simulate the skull. The spherical phantom will be described in more detail in chapter 3, as will its construction.

2.2.1.2   Meshing

I-DEAS was used to generate all of the finite element meshes used in the current work and elements were tetrahedral and linear. It was necessary to partition the geometrical volume into octants order that the advancing front meshing algorithm could be initiated. Quadratic solutions were not considered. The nodal clouds and the equatorial slices are shown in Figure 2-1 for the homogeneous and 4-shell meshes, and the latter show the positions of those point electrodes which coincide with the equatorial plane. The homogeneous mesh consisted of 24734 nodes and 130229 elements whilst the 4-shell mesh had 22420 nodes and 106825 elements. In the former, the ratio of largest to smallest element was about 49 and, in the latter, 66.
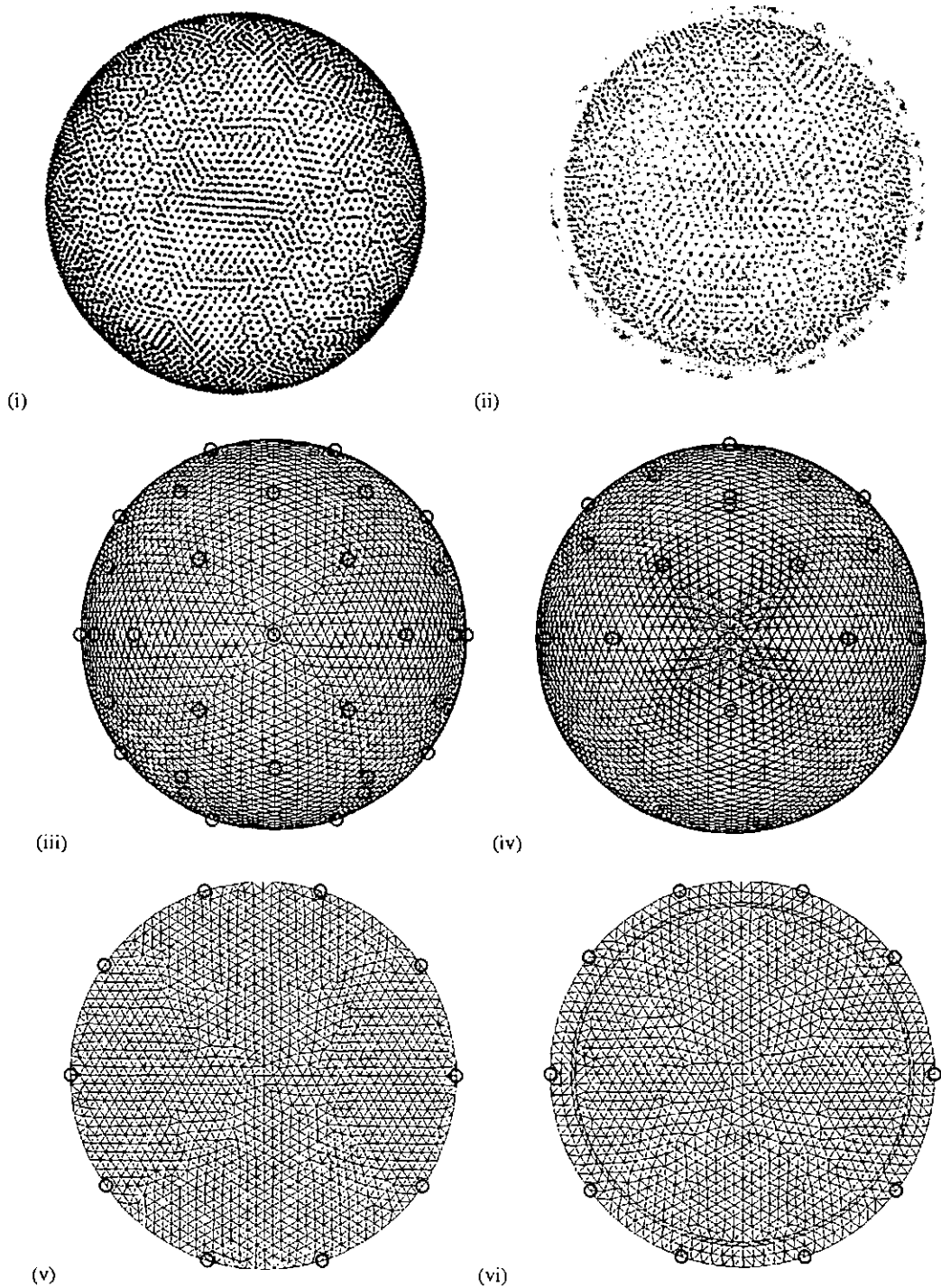
Figure 2-1: The nodal clouds of (i) the homogeneous mesh and (ii) the four-shell spherical mesh – brain (grey), CSF (cyan), skull (beige), scalp (pink). The 4-shell surface mesh from (iii) the top, (iv) the left hand side – the back of the head is to the right of the page. The equatorial planes of (v) the homogeneous mesh and (vi) the four-shell spherical mesh. The red circles show the positions of the simulated equatorial electrodes and are coincident with nodes on the surface of each mesh.

2.2.1.3   Support

Both the FEM and analytical sensitivity matrices were calculated on a nodal basis in order that discretization was equivalent by each method. Therefore, it was necessary to define the volume supporting that node. This process is first explained in 2-D. In the numerical code provided by Dr Dehghani, the support of a node was defined as the sum of the areas (or volumes in 3-D) of all the elements to which that node belongs. By study of Figure 2-2(i), it can be seen that this results in an overlap of the support of each node. The support of 3 nodes (each marked with a red x) is shown as a shaded region. The triangular element defined by these three nodes has shading three times as dense as those elements counted only once. In the case of tetrahedral elements, therefore, it is reasonable to assume that the volume of an element will be counted 4 times since 4 nodes define it.

This was confirmed by a summation of the support of each node (Figure 2-2(ii)) in the tetrahedral mesh defining the spheres. This sum was four times as large as the value obtained using $4\pi r^3/3$. The support of each node was defined as

$$s_n = \sum_{i=1}^{N_S} v_{ei}$$ [2-6]

where N_S is the number of elements to which the nth node belongs and v_{ei} is the volume of each of those elements. It was not redefined to account for overlap because the factor of 4 does not affect the sensitivity of the nodes relative to one another. A distribution is shown in Figure 2-3 of the magnitude of the elements of support s throughout the upper hemisphere of a 4-shell mesh. The partitioning of the volume can be seen clearly, as it can also in the homogeneous spherical mesh.

(i)   (ii)
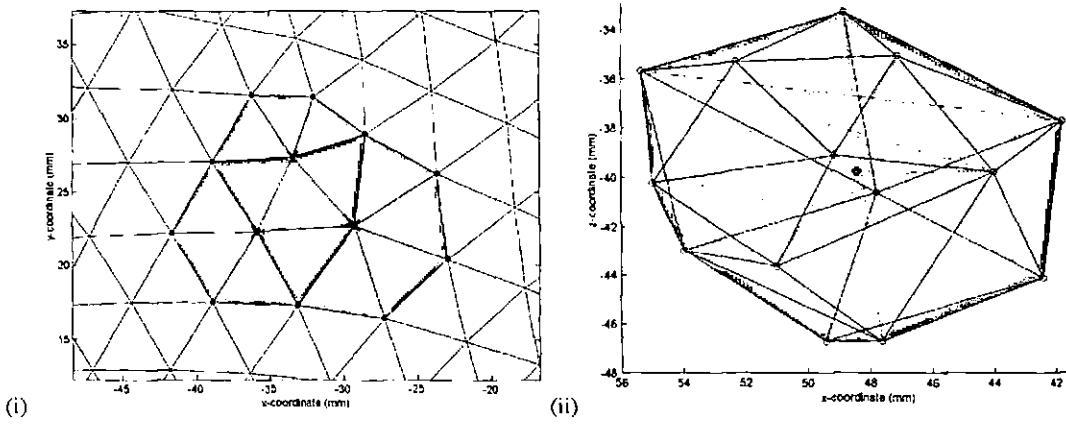
Figure 2-2: (i) A section of a 2D mesh with the shaded areas showing the *support*, and it's overlap, of 3 nodes (red x). (ii) A number of elements make up a polygonal volume defined as the *support* of the node of interest in our technique. In the figure, 24 are shown, each of which has this node (black o) as one of its vertices. The inner edges are red, dotted lines and the faces not containing the node of interest are filled with transparent cyan and bounded by black lines.

Figure 2-3: The figure is a representation of the *support* of the upper hemisphere in the four-shell mesh (divided by 4 so that its sum is equal to the total volume of the sphere).

85

2.2.1.4 The Numerical Solution - MaTOAST

In order to perform a FEM solution for the Jacobian, information was collected from several files. These contained the co-ordinates of the nodes, the connectivity of the nodes, their conductivity, the positions of the 31 electrodes and the list of M=258 electrode combinations with which 4-terminal measurements are made.

The electrodes were shifted so that their location coincided with the surface node nearest their actual position. 21 drive and 38 measurement boundary conditions, or 59 forcing vectors $b_{b=1,...,59}$, were defined at the surface so that current injection was zero at all surface nodes except those defined as coincident with the active electrodes.

Differential operating matrices were built K, K'_x, K'_y and K'_z, (like $\mathcal{T}$ in section 2.1.3.2.4) for scalar and vector fields respectively, using linear interpolation functions. The preconditioned conjugate gradient method was then used 59 times, as defined in the MATLAB function reference (http://www.csb.yale.edu/userguides/datamanip/matlab/help/techdoc/ref/pcg.html), to produce approximate solutions to $[K.\phi_{b=1,...,59}] = [b_{b=1,...,59}]$, where $\phi_{b=1,...,59}$ was a vector whose elements were the scalar electric potential at each node in the mesh.

The three components of electric field $E_{b=1,...,59} = [E_x, E_y, E_z]_{b=1,...,59}$ were calculated at every node for each boundary condition by pre-multiplication of $\phi_{b=1,...,59}$ by K'_x, K'_y and K'_z. When field was plotted, it was not a smooth function, as it should have been. However, division at each node by the corresponding element of the support vector s corrected for this to produce the smoothly-varying $\widetilde{E}_{b=1,...,59}$. The scalar product was found at each node, for each of the M, 4-terminal measurement configurations in order to build the Jacobian so that the sensitivity coefficient at the nth node during the mth measurement was defined as

$$A_{mn}^{FEM} = (\widetilde{E}_{drive}^{n} \cdot \widetilde{E}_{meas}^{n})_m \cdot s_n \qquad [2\text{-}7]$$

2.2.1.5 The Analytical Solution for a homogeneous sphere

2.2.1.5.1 Field Calculation

The calculation of field was carried out in exactly the same way as described in section 2.1.4.1 but, in this implementation, its value was found at every node in the same mesh as was used for the FEM solution and the lower hemisphere was considered as well as the upper hemisphere.

2.2.1.5.2 Generation of a Sensitivity Matrix

In order to generate the sensitivity matrix, the scalar product was taken, at each node, of the drive and measure fields for each 4-terminal measurement. These nodal values were multiplied by nodal support in order to discretize the Geselowitz sensitivity relationship.

2.2.1.6 The Analytical Solution for a 4-shell sphere

2.2.1.6.1 Field Calculation

In this thesis, to generate a new sensitivity matrix for the head, Poisson's equation was solved for Φ and then for $\nabla\Phi$ in a multi-layered sphere with suitable conductivities and geometry. The solution for Φ was derived by Ferree (Ferree, Eriksen et al. 2000) for injection of current I through point electrodes on a four-shell sphere in order to estimate the regional head tissue conductivities *in vivo*.

$$\Phi^{(\alpha)}(r) = \sum_{n=1}^{\infty} \left[A_n^{(\alpha)} \left(\frac{r}{r_\alpha} \right)^n + B_n^{(\alpha)} \left(\frac{r_\alpha}{r} \right)^{n+1} \right] \cdot \left[P_n(\hat{r}.\hat{r}_A) - P_n(\hat{r}.\hat{r}_B) \right] \qquad [2\text{-}8]$$

where $r = |r|$; r_A and r_B represent the locations of the injection electrodes; r_α is the radius of layer α; P_n is the Legendre polynomial of order n; and $A_n^{(\alpha)}$ and $B_n^{(\alpha)}$ are constant coefficients, for each region, determined by the appropriate boundary conditions. Those conditions are the continuity of potential and radial current density between different tissue layers α and the Neumann boundary conditions at the scalp surface, which state that normal current density is zero everywhere except under the electrodes. In this case, it was set equal to $-(I / r_4^2)$.

The solution [2-1] differs to that of Pidcock because it has been simplified by the assumption of azimuthal symmetry for injection through each electrode. Hence, it need not contain the associated Legendre polynomials (Pidcock, Kuzuoglu et al. 1995). To calculate

the appropriate sensitivity matrix, it was necessary to differentiate expression [2-8] using the spherical form of ∇. Hence an analytical expression was found to describe the field E in spherical co-ordinates

$$E^{(\alpha)}(\mathbf{r}) = \underline{e}_r \left(\frac{1}{r_\alpha}\right) \cdot \sum_{n=1}^{\infty} \left[A_n^{(\alpha)} n \left(\frac{r}{r_\alpha}\right)^{n-1} - B_n^{(\alpha)} (n+1) \left(\frac{r_\alpha}{r}\right)^{n+2} \right] \cdot \left[P_n(x_A) - P_n(x_B) \right]$$

$$+ \underline{e}_\theta \left(\frac{1}{r}\right) \cdot \sum_{n=1}^{\infty} \left[A_n^{(\alpha)} \left(\frac{r}{r_\alpha}\right)^{n} + B_n^{(\alpha)} \left(\frac{r_\alpha}{r}\right)^{n+1} \right] \cdot F(\theta, \theta_A, \theta_B, \varphi_A, \varphi_B, x_A, x_B)$$

$$+ \underline{e}_\varphi \left(\frac{1}{r}\right) \cdot \sum_{n=1}^{\infty} \left[A_n^{(\alpha)} \left(\frac{r}{r_\alpha}\right)^{n} + B_n^{(\alpha)} \left(\frac{r_\alpha}{r}\right)^{n+1} \right] \cdot G(\theta, \theta_A, \theta_B, \varphi_A, \varphi_B, x_A, x_B) \qquad \text{[2-9]}$$

where

$$F = [\sin\varphi_B \sin(\theta - \theta_B) \frac{\partial}{\partial x_B}\{P_n(x_B)\} - \sin\varphi_A \sin(\theta - \theta_A) \frac{\partial}{\partial x_A}\{P_n(x_A)\}] \qquad \text{[2-10]}$$

$$G = [(\cos\varphi \sin\varphi_A \cos(\theta - \theta_A) - \sin\varphi\cos\varphi_A) \frac{\partial}{\partial x_A}\{P_n(x_A)\}$$

$$- (\cos\varphi \sin\varphi_B \cos(\theta - \theta_B) - \sin\varphi\cos\varphi_B) \frac{\partial}{\partial x_B}\{P_n(x_B)\}] \qquad \text{[2-11]}$$

and $\qquad x_{A/B} = \hat{r}.\hat{r}_{A/B} = \sin\varphi \sin\varphi_{A/B} \cos(\theta - \theta_{A/B}) + \cos\varphi\cos\varphi_{A/B} \qquad \text{[2-12]}$

Upon trying to implement the equations using values reported by Ferree (2000), I found that solutions diverged. Although their results were valid, the equations they published were incorrect and an errata was published at a later date (Ferree, Eriksen et al. 2001).

2.2.1.6.2 Convergence

The solution for E contains an infinite summation, as does expression [2-8]. In order to implement the solution, it was necessary to include only a finite number of terms. A plot of the partial solution versus N_{max}, the number of terms included in that partial solution, revealed a decaying oscillation, which approached a value E_∞ the solution after summation of an infinite number of terms. At most points in the sphere, the solution for E converged quickly enough so that it sufficed to truncate the solution by averaging over the range $N_{max} = 100 - 250$. In the scalp, however, the magnitude of the oscillations increased dramatically with

increasing radius and their period increased as $\hat{r}.\tilde{r}_{A/B} \rightarrow 1$. To obtain accurate solutions here, the lower and upper limits of the average were higher and further apart. $N_{max} = 250 - 500$ was used in this region for the solutions which follow.

2.2.1.6.3   Generation of Sensitivity Matrix

Sensitivity coefficients were calculated as in section 2.2.1.5.2 using the solution for field in a 4-shell sphere. Values were found at all nodes except those on the surface of the scalp, since the convergence of field solutions was poor there.

It was impossible, from the equations, to calculate the field for a node at $r = 0$. The value here was taken as the mean value of those at its nearest-neighbour nodes. When electrodes were situated on one of the axes of the mesh, it was impossible to define field on those nodes situated on that axes because the differentials of the Legendre polynomials contain a zero/zero term. However, the functions are not asymptotic either side of the singularities so their values were approximated again by the mean for the surrounding nodes.

2.2.1.7 Comparison of Homogeneous and 4-Shell Forward Solutions

In initial numerical simulations, the potential distribution $\phi(r)$ was calculated for current injection between electrodes at ($\pm R$, 0, 0) where R was the radius of the sphere (see Figure 2-1(v) and (vi)). ϕ was then sampled at nodes around the circumference of the equatorial plane of the sphere. Each of the profiles was also simulated analytically, for homogeneous and 4-shell spheres, using equations [2-2] and [2-8], with N_{max} = 100 – 250 in the latter. The same homogeneous mesh was used for comparison between analytical and numerical solutions for the homogeneous sphere and the same 4-shell mesh was used to compare solutions for the 4-shell sphere.

The current density $J = \sigma E$ was also calculated, using the analytical solution for four shells, at all points on a square grid, 80 voxels across, describing a plane across the centre of the homogeneous and the 4-shell spheres. In the former calculation, each shell was given the same conductivity, $\sigma = 0.25$ S m^{-1}. In each model, the mean magnitude of current density was then found only for the region defined as brain. This demonstrated the effect on the analytical solution for current flow when the skull and CSF were included and provided some idea of the relative sensitivity of each model to resistance changes within the brain.

In order to further compare the solution to the forward problem using analytical and linear FEM methods, the current density $J(r)$ was calculated on the 4-shell, spherical mesh. $J(r)$ was found analytically by evaluating $E(r)$ at each node and multiplying each nodal value by the conductivity of the medium in which that node existed. Nodes on the boundary between two media were considered to belong to the inner medium. $E(r)$ was difficult to evaluate accurately on the outer boundary of the sphere (for reasons mentioned above) so these values were not calculated. $|J(r)|$ was then calculated numerically throughout the volume (including surface nodes) using linear tetrahedral elements in MaToast.

2.2.1.8   Generation of Simulated Image Data Sets

2.2.1.8.1   Reference data

For *rigorous simulation* of the expected data set, a current of 1A was injected through point electrodes situated at two appropriate nodes on each mesh and the potential difference then calculated between two other nodes corresponding to the measurement electrodes. By this method, 258 4-terminal measurements were simulated in order to compare further numerical and analytical solutions for potential ϕ in each spherical model, shelled and homogeneous. Equation [2-8] was used to solve for Φ in each case.

As a test of the forward solution, equation 1-14 was then used to generate data sets, $\mathbf{V}_{ref}$, for the analytical and FEM 4-shell, spherical models. This will be referred to as the *Discretized Sensitivity Method* (*DSM*) to produce the forward solution. It is the inverse of this data that forms the diagonal of $\mathbf{R}$, the row-normalization matrix. Results were compared with the 258 voltage measurements predicted by solutions for ϕ. A further data set was generated including sensitivity coefficients for only those nodes existing in the upper hemisphere. This was in order to assess the importance of including the lower hemisphere in the sensitivity matrix.

It is reasonable to ask, if the forward predictions are affected by the omission of sensitivity coefficient below the equator, how are they affected by omission of coefficients on the surface of the sphere? Finally, DSM was used to predict voltages using the numerical sensitivity matrix for 4 shells with and without the surface coefficients.

2.2.1.8.2   Perturbation Data

Equation 1-15 was used to generate perturbation data for numerical and analytical 4-shell models. For all simulations, nodes were found which fell within a spherical region inside the brain, of radius 5mm, and the corresponding values of the conductivity vector were increased by 10%. This distribution is referred as the *target* conductivity distribution. $\mathbf{V}_{pert}$, the perturbed voltage was found for multiple locations of a single perturbation. The reference data was subtracted from this and the difference was normalized, as described in section 1.6.2.3 so that

$$\Delta\mathbf{v}_n = (\mathbf{V}_{pert} - \mathbf{V}_{ref}) \, . \, / \, \mathbf{V}_{ref} \qquad\qquad [2\text{-}13]$$

and, as in Equation 1-16, for the ith perturbation

$$(\Delta\mathbf{v}_n)_i = \mathbf{R}\mathbf{A}\Delta\sigma_i \qquad\qquad [2\text{-}14]$$

This provided computer-simulated data for reconstruction. However, to avoid committing the inverse crime (whereby only the matrix inversion is tested, and not the reliability of the model), the forward calculation was made, in all cases, for a more densely meshed volume defined by 44588 nodes and 244073 elements. Results of this simulation and subsequent reconstruction will be left until the next chapter but its inclusion here is important in order that the reader may understand the steps in the reconstruction process described in section 2.2.2.

2.2.2 The Inverse Problem of Image Reconstruction

2.2.2.1 Normalization, Post-Weighting and Smoothing Combined

The sensitivity matrix $\mathbf{A}$ was R-normalized to give a new matrix $\mathbf{RA}$, as described in section 1.6.2.3, in order that percentage difference data could be reconstructed and electrode errors could be reduced in tank reconstructions. It was also C-normalized before inversion, the nth diagonal element of $\mathbf{C}$ being

$$w_n = \left[\sum_{m=1}^{M} A_{mn}^2 \right]^{-1/2}$$

[2-15]

as in the weighting scheme described in section 2.1.5.3. The matrix, to be inverted, was then $\mathbf{RAC}$. The diagonal matrices $\mathbf{R}_{258 \times 258}$ and $\mathbf{C}_{N \times N}$ were stored as sparse matrices. A plot of the log of w_n and of the smoothed weighting vector $w_n s_n$ are shown in Figure 2-4 for the 4-shell sensitivity matrix. Suppression can be seen clearly near to the electrodes and amplification towards the centre and in the lower hemisphere, weighting coefficients for which are up to 3 orders of magnitude greater than near the electrodes. Some asymmetry can by seen in the YZ-plane as a result of asymmetry in the electrode configuration.
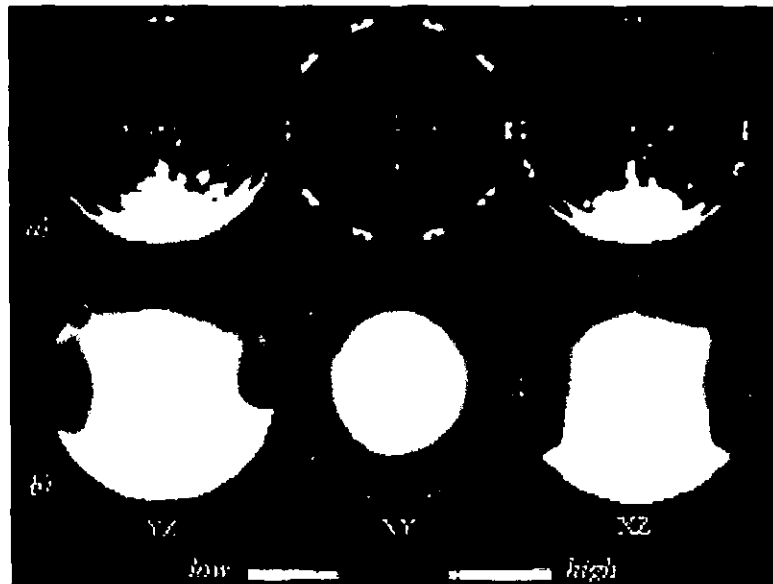
Figure 2-4: The spatial variance of a) the C-normalising vector and b) the same smoothed by multiplication by support, for the 4-shell sensitivity matrix. These are plotted in three perpendicular planes and described by a log colour scale, covering 3 orders of magnitude. The YZ plane is shown viewed from the right hand side.

After square Moore-Penrose inversion of **RAC** (section 1.6.3.4.2), the inverted matrix was premultiplied by **C**, in a fashion similar to the weighting scheme of Clay *et al.* (2002). This made the reconstruction process consistent with the data generation process, described in section 2.2.1.8.2. The weighting was also then equivalent for the homogeneous and 4-shell, analytical and numerical reconstructions, unlike a uniformity correction that might have been invented for each, similar to Gibson's (2000).

To summarize the reconstruction process so far

$$\Delta\sigma_{image} \approx \mathbf{C(RAC)}^* \Delta v_n \qquad [2\text{-}16]$$

where * indicates the square Moore-Penrose inversion. However, in equation [2-14], **A** is not a spatially smooth matrix. It is lumpy because its value, at each node, is proportional to its support but the detail of its lumpiness is largely lost when only 258 data points Δv_n are sampled on the surface. In equation [2-16], the multiplication of **A** by **C**, in parenthesis, removes all the effect of lumpiness introduced by support and it is a spatially smooth matrix that is inverted. Pre-multiplication by **C** reintroduces the lumpiness but Δv_n does not contain enough information to cancel this. Therefore, a lumpy distribution $\Delta\sigma_{image}$ is produced, even if the target distribution $\Delta\sigma_{target}$ was smooth. Rather than introducing a Gaussian smoothing routine, it sufficed to premultiply again by a matrix **S** containing the support vector s on its diagonal so that the final reconstruction process can be summarized by

$$\Delta\sigma_{image} \approx \mathbf{SC(RAC)}^* \Delta v_n \qquad [2\text{-}17]$$

Without this premultiplication, image reconstruction is very susceptible to meshing artefacts since normalization increases sensitivity in regions where the mesh is finer. In the case of the spherical meshes, changes were drawn towards partitioning planes (see Figure 2-4a).

2.2.2.2   *Threshold for Truncation*

The matrices generated using the different models displayed different condition when the decay of the singular values was plotted (see section 1.6.3.4). I decided to truncate singular values once they had decreased to 0.1% of the maximum value. This choice reflected the noise characteristics of data acquired by Gibson from saline-filled tanks (2000), and was used to regularize all reconstructions in this thesis and ensure consistency between methods.

2.2.2.3   *Condition*

The condition of the square matrix $\mathbf{AA}^T$ was studied for all four generated sensitivity matrices, as was the effect on this of row-normalization and column-normalization, using

singular value decomposition as an analysis tool. R and C were calculated for the homogeneous and 4-shell numerical sensitivity matrices A. In each case, after decomposition of square matrices AA^T, $AC(AC)^T$ and $RAC(RAC)^T$ into U, K and V, the decay of the diagonal of K was plotted for comparison.

2.3 Verification Results

2.3.1 The Forward Problem

2.3.1.1 Current Distribution

2.3.1.1.1 Homogeneous versus 4-Shell

The magnitude of current density $|J(r)|$ (Am^{-2}) was found at every point on the grid defined above and the results were plotted (Figure 2-5) in using the Matlab SURF function with interpolated shading, the COLORMAP set to 'grey' and a colour axis defined to show variation in areas of low current density while allowing the plot to saturate near to the electrodes.

(i)   (ii)
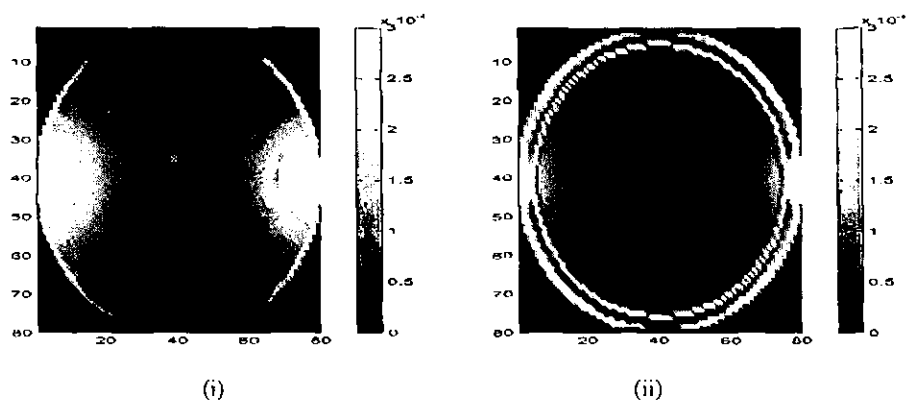
Figure 2-5: A Matlab interpolated SURF plot of $|J(r)|$ (Am^{-2}) on an 80x80 grid in the plane of two bipolar point electrodes applying 1μA on the surface of a (i) homogenous sphere of conductivity $\sigma=0.25$ S m^{-1} and (ii) 4-shell sphere as described in methods. The x- and y-axes are pixel numbers.

The mean value of $|J(r)|$ in the diametric plane across the brain was 9×10^{-5} Am^{-2} and 5×10^{-5} Am^{-2} in the homogeneous and four-layered concentric spheres respectively. Its maximum value was 1.9×10^{-4} Am^{-2} and 1.1×10^{-3} Am^{-2} for each respectively. The ratio of the two means was 0.56 and of the two maxima 0.18. The maximum value of current density in the scalp region of both spheres was calculated to be around 0.06 Am^{-2}. This was calculated 0.8mm from the point electrodes by definition of the grid with respect to the electrode positions. The value was 60 times and 330 times greater than the maximum in the brain region of the respective models.

2.3.1.1.2 4-Shell Numerical versus Analytical

Figure 2-6(a) shows the magnitude of current density, calculated analytically on the 4-shell mesh. For the sake of the plot, $|J(r)|$ at the boundary was set to the mean value throughout the rest of the object. The solution is also shown in Figure 2-6 (b) using linear tetrahedral elements in the MaTOAST FEM implementation.
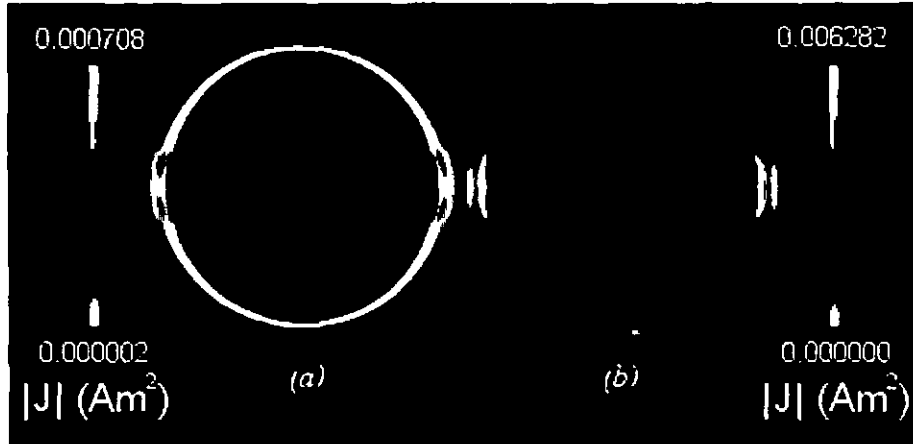
Figure 2-6: The magnitude of current density $|J(r)|$ (plotted on a log colour scale) throughout a 4-shell sphere when current is injected through 2 point electrodes on its surface, solved (a) analytically, (b) numerically on linear, tetrahedral elements, using MaTOAST. Current was not evaluated on the surface of the analytical model

2.3.1.2   *Potential Distributions*

Voltage profiles around the equator can be seen in Figure 2-7 for homogeneous (1 Sm⁻¹)
and 4-shell spheres, calculated analytically and by the MaTOAST, 3-D FEM implementation.
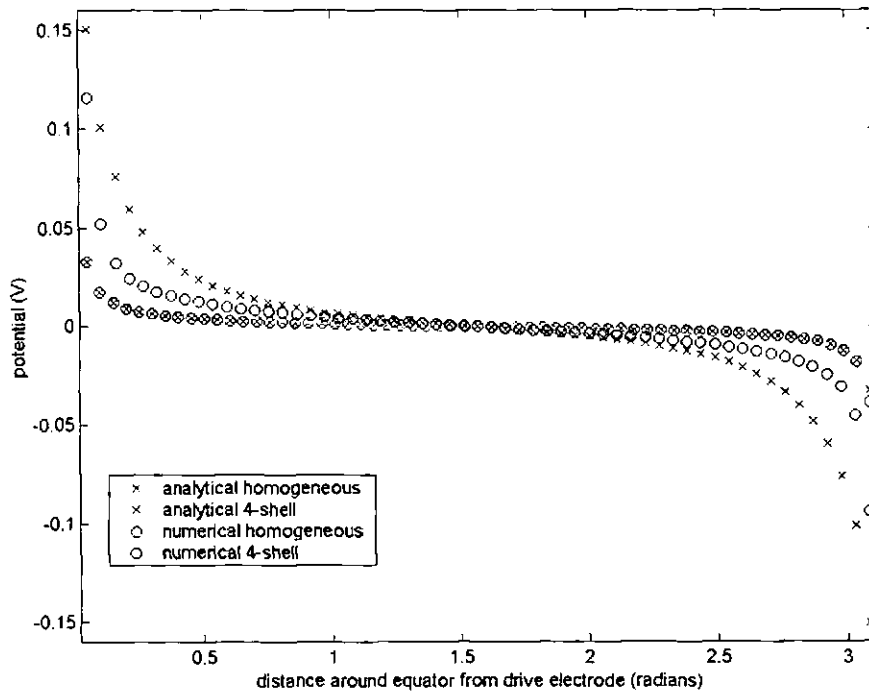
Figure 2-7: Profiles of voltage on the surface of a) a homogeneous sphere (R=100mm, σ=1S m⁻¹)
and b) a sphere made up of four shells (R=80mm, R=82mm, R=87mm, R=92mm, σ_1=0.25 S m⁻¹,
σ_2=1.79 S m⁻¹, σ_3=0.018 S m⁻¹, σ_4=0.44 S m⁻¹). Each profile is taken along the equatorial arc
joining two point electrodes on their surfaces, situated opposite each other and on the x-axis. 1mA
was passed through the sphere in each case.

2.3.1.3   Image Data Sets

2.3.1.3.1   Sampling from Potential Distributions

Figure 2-8 shows a data set, simulated on a homogeneous sphere (R=100mm, σ=1Sm⁻¹) analytically (solid blue line) and numerically, using MaTOAST (red circles). The order in which electrodes were chosen for the 258 4-terminal measurements confounded intuitive understanding of the data set and the reader may find it looks like noise. However, its shape is quite characteristic and will be recognised in chapter 3 when comparison is made between simulated and measured data sets.
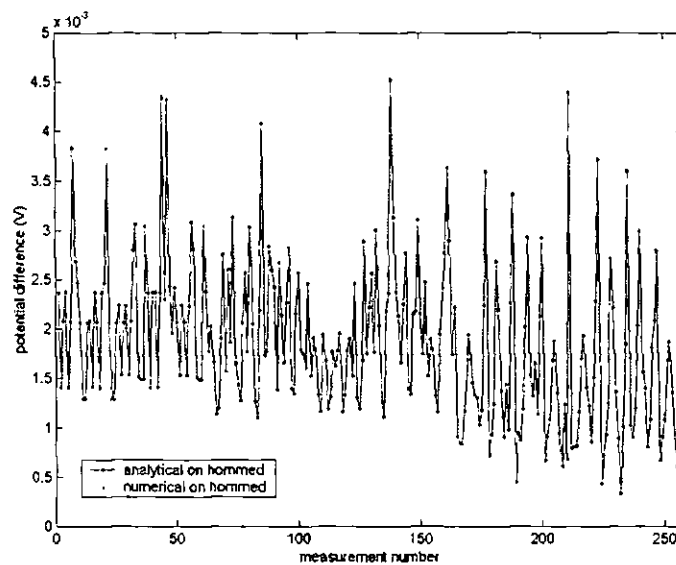
Figure 2-8: 258 voltage measurements, following EIT protocol, on the surface of a homogeneous sphere (R=100mm, σ=1 S m⁻¹), simulated a) analytically and b) numerically using MaToast.

2.3.1.3.2   The Discretized Sensitivity Method – 4-Shell Spheres

The rms difference between the two analytical predictions was 15.5% using the DSM and by direct calculation of surface potentials. When sensitivity coefficients from the lower hemisphere were neglected, the rms differences between the DSM and direct calculation of potentials increased to 43% for analytical data generation.

The rms difference between predictions by the numerical DSM and the analytical solution for potential difference was 41.3%. When the same data was compared with potential differences predicted by the FEM solution for ϕ, the rms difference was 0.18%. This increased to 48.7% when only coefficients from the upper hemisphere were used.

Finally the rms difference between data predicted using the numerical DSM with and without inclusion of the surface coefficients was 5.6%.

2.3.2 The Inverse Problem

2.3.2.1 Condition of Numerical Matrices

It appeared that AA^T was better conditioned than $AC(AC)^T$ and $RAC(RAC)^T$ and that row-normalization didn't make much difference to the condition of the square matrices whether column-normalization had or had not already been implemented.
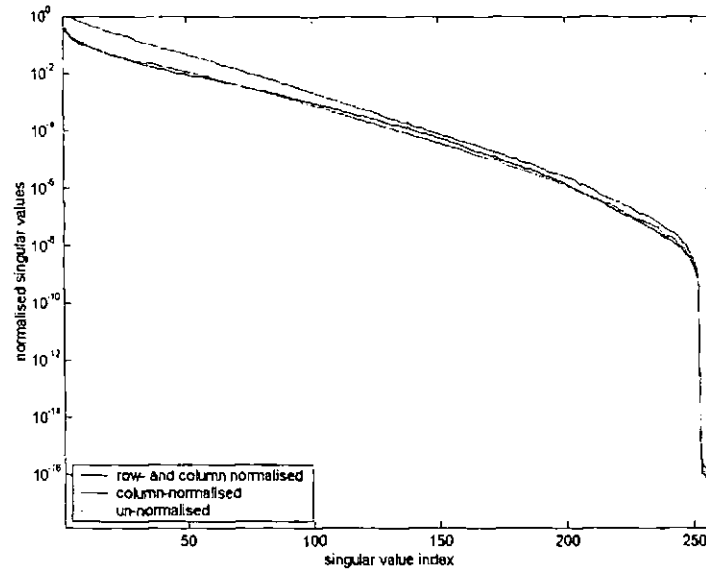
Figure 2-9: Singular values for the homogeneous numerical matrix normalized in different ways: AA^T (green); $AC(AC)^T$ (red) and $RAC(RAC)^T$ (black).
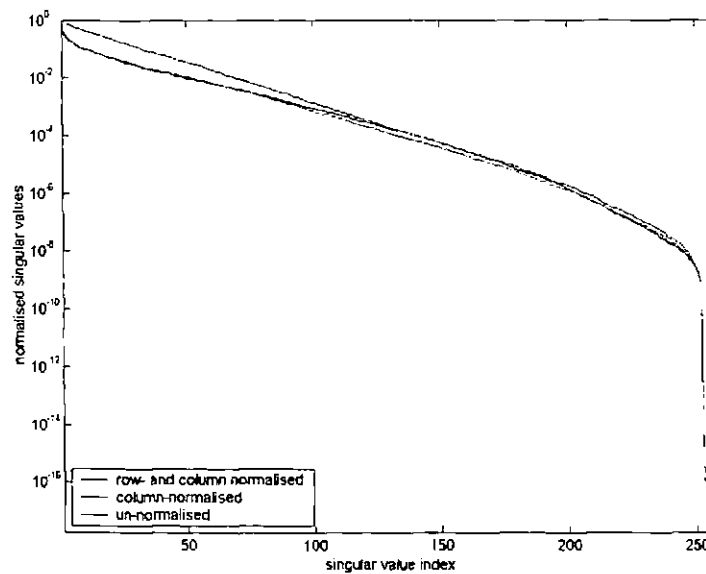
Figure 2-10: Singular values for the 4-shell numerical matrix normalized in different ways: AA^T (green); $AC(AC)^T$ (red) and $RAC(RAC)^T$ (black).

100

2.3.2.2 Condition of Analytical Matrices

Row-normalization had a horrendous effect on the condition of the square matrix for the homogeneous sphere. as can be seen in Figure 2-11. Upon examination of the diagonal of $\mathbf{R}$. it was found to have a large dynamic range as a consequence of some very small data predictions using the DSM (section 2.2.1.8.1). Six measurements were neglected, along with the corresponding rows of the sensitivity matrix. to form reduced matrices $\mathbf{R}_r$ and $\mathbf{A}_r$. Where, before, $\mathbf{R}$ and $\mathbf{A}$ were MxM and MxN matrices. $\mathbf{R}_r$ and $\mathbf{A}_r$ were M_rxM$_r$ and M_rxN matrices, where M_r was the number of included measurements, 252 in this case. This technique will be referred to as *reduced-row-normalization*.

In the case of the homogeneous sphere, it appeared. this time, that $\mathbf{AA}^T$ was worst conditioned, ignoring the first. disastrous attempt at row-normalization. It can be seen in Figure 2-11 that reduced-row-normalization didn't make much difference to the condition of the square matrices when column-normalization had been implemented. The same was the case when column-normalization had not been implemented.

In the case of the 4-shell sphere. it was not necessary to perform reduced-row-normalization since ordinary row-normalization sufficed. Again, this did not make much difference to condition. The decay of singular values for $\mathbf{AA}^T$ was slower initially but became much faster than for the other square matrices after about 50 singular values or decay to about 0.3% of the maximum value.
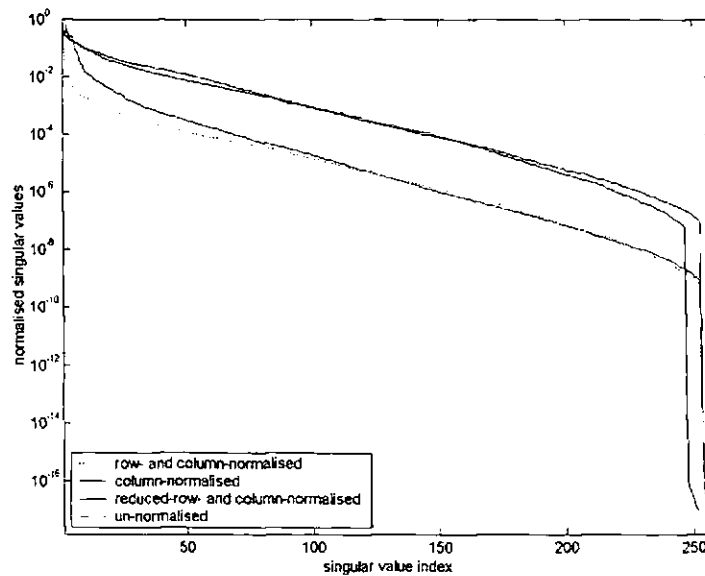
Figure 2-11: Singular values for the homogeneous analytical matrix normalized in different ways: $\mathbf{AA}^T$ (green); $\mathbf{AC(AC)}^T$ (red); $\mathbf{RAC(RAC)}^T$ (black dotted :) and $\mathbf{R}_r\mathbf{A}_r\mathbf{C(R}_r\mathbf{A}_r\mathbf{C)}^T$ (black solid) – see text.
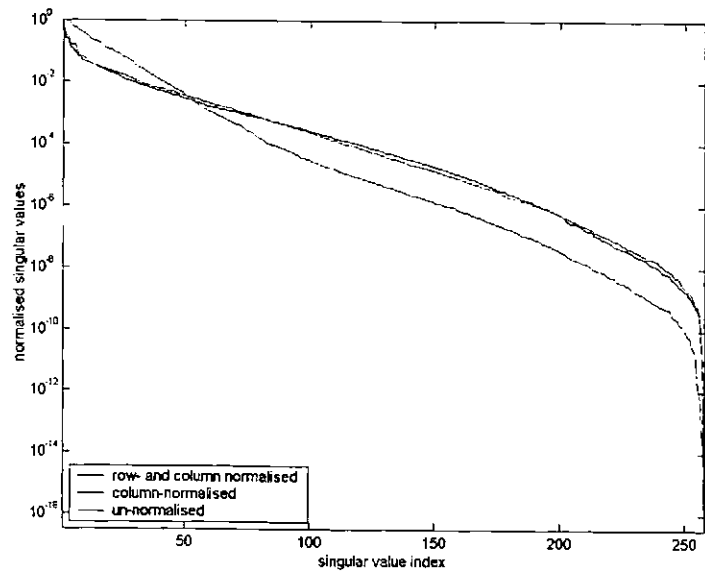
Figure 2-12: Singular values for the 4-shell analytical matrix normalized in different ways: $\mathbf{AA}^T$ (green); $\mathbf{AC(AC)}^T$ (red) and $\mathbf{RAC(RAC)}^T$ (black).

2.4 Discussion

Solutions have been compared for electric current density and potential, as have the sensitivity relationships between conductivity distribution and predicted boundary voltage measurements.

There was a dramatic difference between the two current distributions calculated analytically and shown in Figure 2-5. Shunting occurred in both the scalp and the CSF of the shell model, as expected, and the mean value of current density in the brain region of the 4-shell sphere was about half that in the equivalent region of the homogeneous model whilst the maximum value was about a fifth. Therefore, by using the sensitivity matrix for a homogeneous sphere, a reconstruction algorithm will overestimate the sensitivity of scalp measurements to resistance changes in the brain. The reduction in sensitivity was consistent with Gibson's results (see section 1.7.2.2.1.) for homogeneous image reconstruction of data from a homogeneous and from a shelled hemisphere. He found that the mean peak change in images from the latter was one third that in images from the former (Gibson 2000).

It appeared that there was a discrepancy, however, between predictions of current density throughout the analytical and FEM 4-shell models. The decrease of $|J(r)|$ was monotonic along a line towards the centre from the electrode in the analytical solution while, in the FEM solution, there was a dip in the skull region. There are three possible reasons to doubt the accuracy of the FEM solution in this region. Firstly, a linear method has been used. This is difficult to justify in regions of high field variation as is the case near an electrode and near a boundary between tissues, especially when they are of high resistivity contrast, as in the head. Secondly, each tissue layer is thin and, in the mesh, was only one element thick. Thirdly, in order to obtain the analytical solution for 4-shells, continuity of radial current density was imposed as an internal boundary condition. No such condition is imposed in the MaTOAST FEM solution. To predict $|J(r)|$, electric field was multiplied by the strictly region-specific conductivity values. This would have produced the results seen for numerical predictions, which smoothed the high field variation between regions due to insufficient meshing, order of interpolation and imposition of boundary conditions.

It can be seen in Figure 2-7 and Figure 2-8 that analytical and numerical solutions for ϕ were very similar when calculated for a homogeneous sphere. However, there was a marked difference between analytical and numerical solutions for a 4-shell sphere, as is clear from Figure 2-7. In this, the potential profile on the FEM 4-shell sphere lies somewhere between the analytical profiles for a 4-shell sphere and for a homogeneous sphere. This further

suggests the inability of a linear FEM to take into account the presence of thin, highly contrasting tissue layers, especially when those layers are only one element thick.

Comparison was made of the rigorous and the discretized sensitivity method to generate reference data on the surface of the 4-shell sphere. The analytical sensitivity matrix produced data with an rms difference from the *gold standard* almost 3 times less than did the numerical sensitivity matrix. It was also 3 times less than the rms difference between rigorous predictions, made numerically, and the gold standard. However, the difference was still 15%. This suggests that, although the analytical model may more accurately represent electric field throughout the object, its accuracy is limited when discretization is performed in order to generate the sensitivity matrix. When coefficients from the lower hemisphere were ignored, the rms error increased to 43%, suggesting that it is important to include them.

Data predictions were affected much less by omission of boundary coefficients. Although not published here, reconstructions were performed using the FEM sensitivity matrix with and without surface nodes included. Images were not visibly different.

Examination of the matrices intended for inversion proved to be very fruitful indeed. It was seen that ordinary row-normalization could cause the condition of the sensitivity matrix to deteriorate badly if some measured voltages were close to zero. However, it was shown that row-normalization was still viable if small measurements were left out of the reconstruction process. In future, the measurement protocol may be modified so that there is no risk of small measurements. Results suggested the AA^T was better conditioned in numerical reconstruction, calling into question the need for row normalizing at all. However, the difference was slight and the advantage gained by normalizing was significant enough for analytical reconstruction that the square matrix $RAC(RAC)^T$ (or $R_rA_rC(R_rA_rC)^T$) was inverted in all the following reconstructions.

104

2.5   *Conclusion*

Methods have been described to generate analytical and FEM sensitivity matrices for reconstruction of EIT images of homogeneous and shelled spheres. In the process, the current and potential distributions throughout each system have been shown to be substantially different, both by analytical and by numerical methods, although the difference was more profound by the former method.

Results suggest that the analytical method and the numerical method perform similarly for a homogeneous object of ideal geometry such as a sphere. However, they suggest that the analytical method more accurately reflects reality in the presence of concentric shells of contrasting resistivity.

It remains to be seen how images are affected by the inclusion of shells in the model and to what relative degree analytical and numerical methods take them into account. The method for reconstruction has been described above with a modification, suggested by results from SVD analysis of reconstruction matrices

$$\Delta\sigma_{image} \approx SC(R_rA_rC)^* \Delta v_n \qquad [2\text{-}18]$$

where R_r and A_r are reduced row-normalization and sensitivity matrices. This technique will be used, when necessary, in the following two chapters.

The Effect of Layers

3 The Effect of Layers

3.1   Introduction

3.1.1   Inadequacy of Homogeneous Reconstruction

In the past, many EIT image reconstruction algorithms have assumed homogeneity and ideal geometry even when the object under study is inhomogeneous and is of non-ideal geometry. These were reviewed in section 1.7. Although the human head is a layered structure, images have been published using an algorithm that assumes it to be homogeneous and spherical (Gibson, Tidswell et al. 1999; Gibson 2000; Tidswell, Gibson et al. 2001a; Tidswell, Gibson et al. 2001b). Gibson speculated that, as for EEG inverse dipole modelling (Ary, Klein et al. 1981), the presence of shells could be accounted for if the loci of peak impedance changes were multiplied by a factor of about 1.6.

This was shown to be true, to a certain degree, in image reconstructions from data measured on a 187mm diameter, hemispherical tank containing a simulated hemispherical skull made of Plaster. It can be seen from the results, however, that the position of most eccentric change would require a correction factor >2 (Gibson 2000). It is not clear that it was appropriate to model that hemispherical conductor as a sphere, especially when some electrodes were so close to the flat surface. However, using a reconstruction algorithm based on truncated SVD inversion, he obtained images of an insulator moving through 5 positions, within the tank, with a mean localization error 19±15mm and a full width at half maximum (FWHM) of about 55±15mm in the horizontal plane. Upon application of the correction factor 1.6 to the loci of reconstructed peaks, the localization error can be reduced to 8±8mm. However, his homogeneous algorithm produced images containing information about only six planes in the upper hemisphere. Therefore resolution in the z-direction was only 15mm (8% of the image diameter), by the definition of his sensitivity matrix. Z-localization was not considered and errors quoted previously were effectively 2D. The measures were therefore underestimates of localization error.

3.1.2   Purpose

Rather than to suggest methods to compensate for the presence of the skull using a homogeneous reconstruction algorithm, it is the purpose of this chapter to report the effect on image reconstruction of including concentric layers of contrasting resistivity in the forward model of conduction. Layers were taken into account in both analytical and numerical models, as described in chapter 2, and these were used to reconstruct data simulated on a computer and measured on a tank phantom.

3.1.3   Recent Studies

A similar study was described in work submitted by this group last year (Bagshaw, Liston et al. In press), except reconstruction was made using only numerical models (see section 2.1.3.2.5). In terms of loealization accuracy, no significant effect was revealed, due to the presence of layers in the assumed model, for reconstruction of either FEM-simulated data or spherical-tank data. I reported some preliminary images previously (Liston, Bayford et al. 2002), using an analytical multi-shell model, but these were obtained without use of a uniformity correction, post-weighting or row-normalization. By that method, analytically simulated impedance changes, inside a 4-shell sphere, were localized with errors as large as 32mm using a 4-shell analytical sensitivity matrix. It was hoped that post-weighting and row-normalization would improve that result in the study that follows. This study uses analytical models, as well as FEM models to investigate the effect of layers in a spherical conductor and the reconstruction algorithm was chosen, as described in chapter 2, in order that both methods could be used with confidence.

3.2　Methods

3.2.1　Computer Simulation of Image Data Sets

3.2.1.1　Sensitivity Matrices

Two finely discretized *forward sensitivity matrices* were used for data generation and four for image reconstruction in the computer simulation studies. These are documented in Table 3-1. They were generated analytically and numerically as described in the previous chapter.

It was necessary to generate data with a different matrix from that used for reconstruction in order to avoid committing an inverse crime. Since finer discretization also produces more accurate results, coefficients were assigned to nodes of a fine 4-shell mesh (44588 nodes; 244073 elements) in order to build A_{4fine}^{ANA} and A_{4fine}^{FEM}, the two analytical and numerical forward matrices. Data was not simulated for perturbations in a homogeneous sphere.

The four *reconstruction matrices* were evaluated analytically and numerically on coarser meshes describing a homogeneous sphere (24734 nodes; 130229 elements) and a 4-shell sphere (22420 nodes; 106825 elements).

	Analytical	Numerical
Homogeneous Sphere	A_{hom}^{ANA}	A_{hom}^{FEM}
4-Shell Sphere	A_{4shell}^{ANA}	A_{4shell}^{FEM}
4-Shell Sphere (fine)	A_{4fine}^{ANA}	A_{4fine}^{FEM}

Table 3-1: A summary of the sensitivity matrices for computer simulation studies.

3.2.1.2　Simulation of Image Data Sets

Reference and perturbation data sets were generated as described in section 2.2.1.8.2, using the unchanged sensitivity matrices, A_{4fine}^{ANA} and A_{4fine}^{FEM}, to multiply a reference σ_{ref} and a perturbed conductivity distribution vector σ_{pert}. By this method, perturbation data was generated analytically and numerically. In total, 39 spherical perturbations were simulated, of radius 5mm and magnitude 10%, along the x-, y- and z-axes. As an example, those along the negative y-axis are shown in Figure 3-1. In each case, a different number of nodes fell within 5mm of the centre of the change and hence the volume of the *effective*, discretized

perturbation was not consistent. This variation was reflected in the magnitude of the perturbation in the predicted data set. Therefore, images were normalized according to the number of nodes that had been changed in the conductivity vector, which is reasonable since the magnitude of support is fairly constant along the axes. Data was normalized with respect to the reference data to produce $(\Delta v_n^{ANA4shell})_{i=1,\ldots,39}$ and $(\Delta v_n^{FEM4shell})_{i=1,\ldots,39}$.
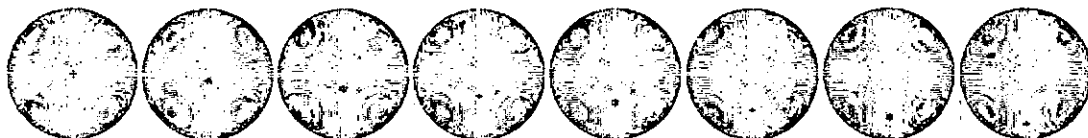
Figure 3-1: Nodes (red) in fine 4-shell mesh on which was imposed a 10% conductivity increase.

3.2.2　Tank Measurements

3.2.2.1　*Construction of the Spherical Tank*

Two hemispherical shells of Perspex, diameter 187mm, were bolted together across a rubber seal and filled with a saturated solution of Calcium Sulphate ($CaSO_4$ - the choice of solution was in order to prevent the simulated skull from dissolving). The tank is shown in Figure 3-2. Measurements of its conductivity σ_{sol} returned a median value of around $0.25Sm^{-1}$ (similar to that of brain tissue) and ranged from $0.21\ Sm^{-1}$ to $0.44Sm^{-1}$. Silver ball electrodes were placed on the inside of the sphere in positions similar to the 10-20 configuration. These were used rather than disc electrodes in order that they closely resembled the point electrode model.

Within the sphere, to simulate the skull, was a spherical shell cast in Plaster of Paris. In practice, core samples were made from many consistencies of plaster until an appropriate mixing ratio was found such that its conductivity was about $0.012Sm^{-1}$ when soaked in the $CaSO_4$ solution. The contrast in resistivity of the shell to its surroundings was therefore about 21:1, a ratio which lies between that reported by Oostendorp *et al.* (2000) and that resulting from comparison of measurements by Saha and Williams (1992) and Geddes and Baker (1967). However, after deciding upon an appropriate ratio, and during construction of the shell, many further core samples were made and their conductivities measured. Compiling the values obtained, and those from further conductivity measurements made on the actual shell, it was found that there existed a range of values, even for cores made from the same batch of plaster mix. It was more realistic to say that the conductivity of the soaked shell was $0.008\ Sm^{-1} - 0.013Sm^{-1}$.

3.2.2.2　*Collection of Data*

Through a hole at the top of the tank and one at the top of the shell, a narrow piece of doweling (2mm) was inserted in order to suspend a $6.3cm^3$ cylinder of Perspex (length 2cm, diameter 2cm) at various positions within the tank, introducing a 100% conductivity decrease. A *baseline-stimulus-baseline* paradigm was adopted. For each position, image data sets were acquired continuously at a rate of about $3s^{-1}$ for a period of 210s using the UCL Mark 1b system operating at 38kHz with constant current injection of 2.2mA. The doweling was present throughout and was used to hold the Perspex for 40 seconds of *stimulus* during this time. By this method, images were obtained of the difference between conductivity during *baseline* and that during stimulus, demonstrating the change due to the Perspex

cylinder alone. Changes were introduced at 29 positions along the x-, y- and z-axes in 29 separate experiments. Data was examined afterwards, from each experiment. and those channels with high levels of noise or drift were set to zero.

For each experiment, data was averaged throughout the baseline epochs before the perturbation was introduced and after it had been removed. This constituted the reference data set V_{ref}. The perturbation data set V_{pert} was found by averaging image data sets acquired throughout the stimulus epoch. The normalized difference between the two $(\Delta V_n^{tank3shell})_{i=1,...,29}$ was saved to file for reconstruction.

(i)   (ii)
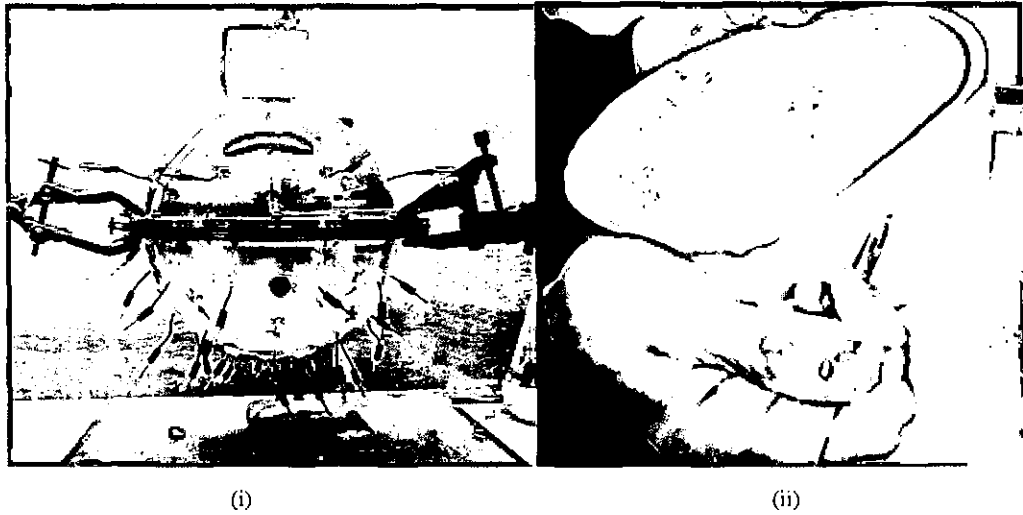
Figure 3-2: (i) The spherical tank phantom, shown for clarity without the presence of the shell to represent the skull and (ii) one half of the Plaster of Paris spherical shell under construction.

3.2.2.3   Comparison of Simulated with Measured Data

3.2.2.3.1   Homogeneous Tank

Initially, data was collected from a homogeneous tank and several perturbation images reconstructed successfully using the old algorithm in order to check acquisition and to check that the electrodes had been manufactured sufficiently well. Data was averaged from 30second baseline epochs before and after the perturbation epoch in one experiment and this was taken as a typical reference image data set.

The image data set was predicted rigorously (section 2.2.1.8.1) using the 4-shell analytical solution for ϕ with σ_{sol} given a range of values from 0.21 to 0.26Sm^{-1}, the outer radius r_4 set to 93.5mm, I set to 2.2mA and boundary conditions imposed at actual, rather than ideal, electrode positions. It was found that measured and predicted data fit best for σ_{sol} = 0.21Sm^{-1}. In this case, discounting the eliminated measurements, the rms error between the

two was 27%, relative to the simulated data, and the median difference 0.3%. The two sets are plotted in Figure 3-3 where it can be seen that 3 measured data points were set to zero due to poor noise levels.
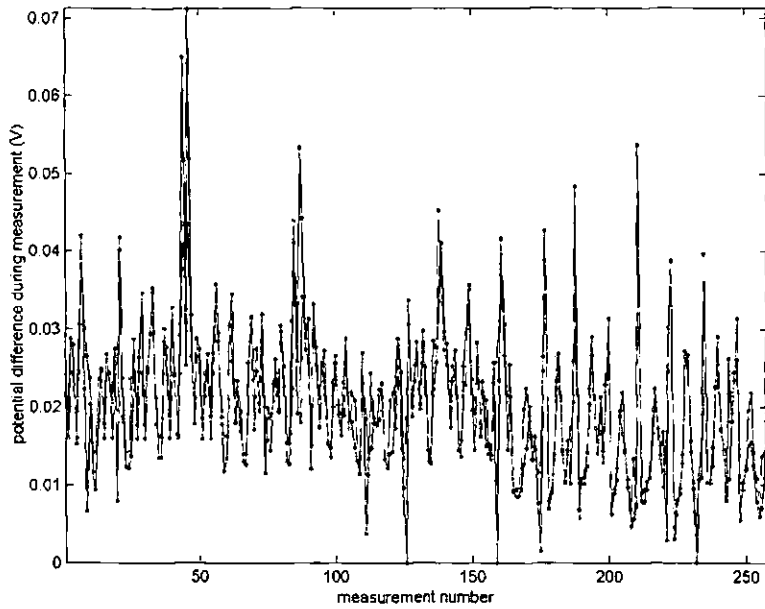
Figure 3-3: Image data set as measured from the homogeneous, spherical tank (black) and as predicted using the analytical equations for potential throughout a 4-shell sphere, with conductivity $\sigma_{1,2,3,4} = 0.21 Sm^{-1}$.

3.2.2.3.2 Shell Tank

A similar exercise was carried out using data from the tank with the plaster shell in place. Parameters were varied in the analytical model in order to provide the best fit between rigorously generated data sets (section 2.2.1.8.1) and measured data. σ_{sol} was varied between $0.21 Sm^{-1}$ and $0.41 Sm^{-1}$ in steps of $0.04 Sm^{-1}$, $\sigma_{plaster}$ was varied between $0.008 Sm^{-1}$ and $0.013 Sm^{-1}$ in steps of $0.001 Sm^{-1}$ and the thickness of the plaster shell $(r_3 - r_2)$ was given values 5mm, 6mm and 7mm. Although the intended thickness of the shell was 5mm, it was difficult to confirm that this had been achieved by measurement. It was likely to be more than 5mm, due to certain processes in its manufacture.

It was found that predicted and measured data fit best when $\sigma_{sol} = 0.25 Sm^{-1}$ and $\sigma_{plaster} = 0.008 Sm^{-1}$. In this case, discounting the eliminated measurements, the rms error between the two was 29%, relative to the simulated data, and the median difference 0.8%. The two sets are plotted in Figure 3-4. Again, three measured data points were set to zero.

113
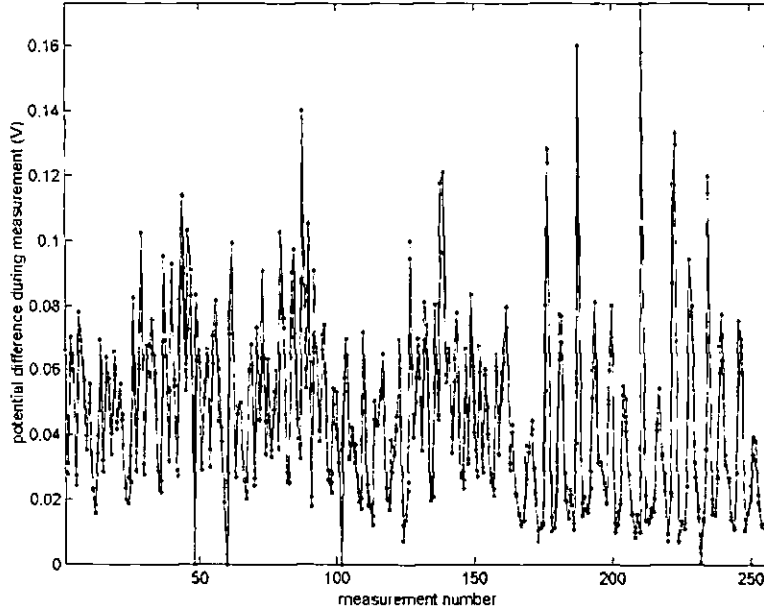
Figure 3-4: Image data set as measured from the spherical tank with simulated skull (black) and as predicted using the analytical equations for potential throughout a 4-shell sphere, with conductivity $\sigma_{1,2,4} = \sigma_{sol} = 0.25\text{Sm}^{-1}$ and $\sigma_3 = \sigma_{plaster} = 0.008\ \text{Sm}^{-1}$.

3.2.2.4 Sensitivity Matrices

For the shell-tank study, new sensitivity matrices were generated taking into consideration the actual, rather than the ideal, electrode positions and, in the case of the multi-shell matrices, to use correct conductivities in the model. Homogeneous matrices $A_{homtank}^{ANA}$ and $A_{homtank}^{FEM}$ were created for reconstructions assuming homogeneity. For multi-shell models, the representative value $\sigma_{sol} = 0.25\text{Sm}^{-1}$ was assigned initially to layers I, II and IV and $\sigma_{plaster} = 0.012\text{Sm}^{-1}$ to layer III. Analytical and numerical sensitivity matrices $^{5mm}A_{3shelltank}^{ANA}$ and $^{5mm}A_{3shelltank}^{FEM}$ were then created and reconstructions performed. It was poor results from this method that drew the attention of the author towards the error minimization study described in the previous section.

That study showed it would be more appropriate to generate a matrix $^{7mm}A_{3shelltank}^{ANA}$ using values $\sigma_{sol} = 0.25\text{Sm}^{-1}$ and $\sigma_{plaster} = 0.008\text{Sm}^{-1}$ and setting the thickness of the skull layer to 7mm instead of 5mm. This modification was implemented only for the analytical model partly for reasons that will become clear in the results and partly because a modified mesh would have been required to produce further FEM solutions. Table 3-2 shows a summary of the sensitivity matrices used in the tank study.

114

	Analytical	Numerical
Homogeneous Sphere	$A_{homtank}^{ANA}$	$A_{homtank}^{FEM}$
3-Shell Sphere	$^{5mm}A_{3shelltank}^{ANA}$	$^{5mm}A_{3shelltank}^{FEM}$
	$^{7mm}A_{3shelltank}^{ANA}$	-

Table 3-2: A summary of the sensitivity matrices for the tank study.

115

3.2.3   Reconstruction of Numerically Simulated Data

$(\Delta v_n^{FEM4shell})_{i=1,...,39}$, the normalized, FEM-simulated data for perturbations in a 4-shell sphere, were reconstructed using A_{hom}^{FEM} and A_{4shell}^{FEM} in order to assess the effect of layers in reconstruction when they are included in the numerical forward model. Two families of solutions were produced, for comparison, from the one family of data as follows

$$\Delta\sigma_{FEMhom} \approx SC(R\,A_{hom}^{FEM}\,C)^{\ast}\,(\Delta v_n^{FEM4shell})_{i=1,...,39} \qquad [3\text{-}1]$$

and $\qquad \Delta\sigma_{FEM4shell} \approx SC(R\,A_{4shell}^{FEM}\,C)^{\ast}\,(\Delta v_n^{FEM4shell})_{i=1,...,39} \qquad [3\text{-}2]$

where **R**, **C** and **S** are as described in the previous chapter and * denotes the square Moore-Penrose inversion (section 1.6.3.4.2). For simplicity, no subscripts or superscripts will be attached with these matrices to describe the mesh or the method of solution. It is tacit that they are simply those normalization and support matrices associated with the labelled **A**.

The condition of each numerical matrix was very similar. The singular value spectra of $RAC(RAC)^{T}$ are plotted for each in Figure 3-5 along with those for analytically generated matrices. Truncation was performed after singular values decayed to 0.1%, as described in section 2.2.2.2 so that 99 singular values were used in the inversion for homogeneous FEM reconstruction and 97 for 4-shell reconstruction.
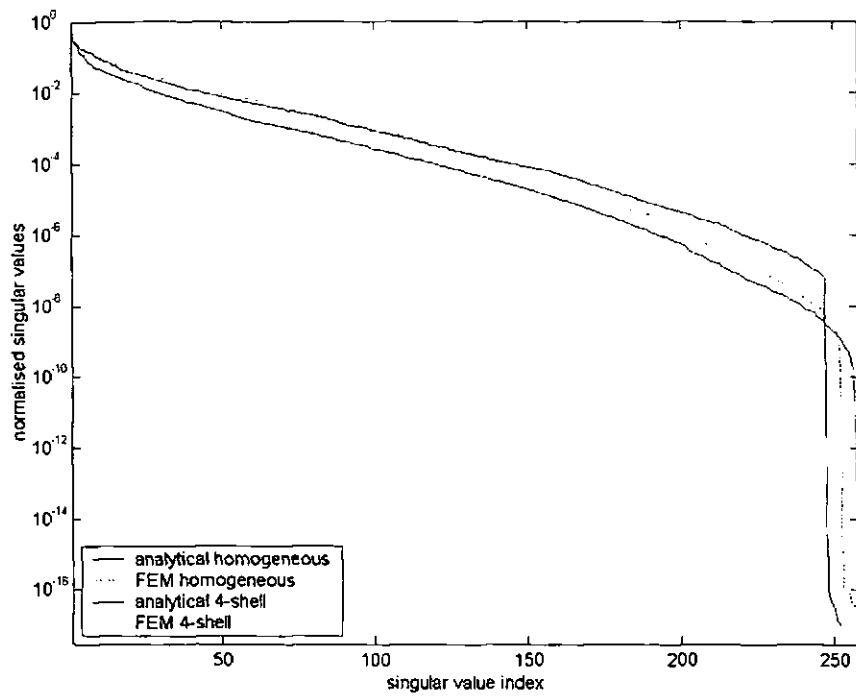
Figure 3-5: Singular value spectra for all matrices $RAC(RAC)^T$ used for reconstructions of computer-simulated data.

3.2.4 Reconstruction of Analytically Simulated Data

$(\Delta v_n^{ANA4shell})_{i=1,...,39}$, the normalized, analytically- simulated data for perturbations in a 4-shell sphere, were reconstructed using A_{hom}^{ANA} and A_{4shell}^{ANA} in order to assess the effect of layers in reconstruction when they are included in the analytical forward model. The same data was also reconstructed using A_{4shell}^{FEM} in order to assess the improvement of the numerical shell matrix over the analytical homogeneous matrix. By this method, three families of solutions were produced, for comparison, from the one family of data as follows

$$\Delta\sigma_{ANAhom} \approx SC(R_r A_{hom}^{ANA} C)^* (\Delta v_n^{ANA4shell})_{i=1,...,39} \qquad [3\text{-}3]$$

$$\Delta\sigma_{ANA4shell} \approx SC(R A_{4shell}^{ANA} C)^* (\Delta v_n^{ANA4shell})_{i=1,...,39} \qquad [3\text{-}4]$$

and $\qquad \Delta\sigma_{FEM4shell} \approx SC(R A_{4shell}^{FEM} C)^* (\Delta v_n^{ANA4shell})_{i=1,...,39} \qquad [3\text{-}5]$

Notice, in equation [3-3], the r subscript after R, indicating reduced-row-normalization, as described in section 2.3.2.2. For reasons explained there, a reduced sensitivity matrix was also used for reconstruction using the analytical model for a homogeneous sphere and the corresponding measurements in $(\Delta v_n^{ANA4shell})_{i=1,...,39}$ were neglected. The 4-shell reconstructions used the entire sensitivity matrices.

Again, truncation was performed after singular values decayed to 0.1% and the singular value spectra of $RAC(RAC)^T$, for the three matrices, can be seen in Figure 3-5. 97, 72 and 97 singular values were used respectively in the inversion for analytical homogeneous and 4-shell and for numerical 4-shell reconstruction.

3.2.5 Reconstruction of Data from the Shell Tank

$(\Delta v_n^{tank3shell})_{i=1,\dots,29}$, the normalized data sets acquired from the 3-shell tank during perturbation experiments, were reconstructed using the two numerical matrices $A_{homtank}^{FEM}$ and $^{5mm}A_{3shelltank}^{FEM}$ and three analytical matrices $A_{homtank}^{ANA}$, $^{5mm}A_{3shelltank}^{ANA}$ and $^{7mm}A_{3shelltank}^{ANA}$, described in section 3.2.2.4. Once more, this was in order to assess the effect of layers in reconstruction when they are included in the forward model.

Truncation was performed at 0.1%. The numbers of singular values included for each reconstruction are listed in Table 3-3 and, in Figure 3-6 is shown the singular value spectra of the row- and column-normalized matrices when they are multiplied by their transpose. Also shown in Table 3-3 is an indication of the improvement made to condition of $RAC(RAC)^T$ by using the reduced-row-normalization method rather than ordinary R-normalization.

	Sensitivity Matrix	Truncation Point	Extra Singular Values
Homogeneous Sphere	$A_{homtank}^{ANA}$	103	24
	$A_{homtank}^{FEM}$	103	-
3-Shell Sphere	$^{5mm}A_{3shelltank}^{ANA}$	82	80
	$^{7mm}A_{3shelltank}^{ANA}$	72	70
	$^{5mm}A_{3shelltank}^{FEM}$	108	-

Table 3-3: A table listing the sensitivity matrices used for tank reconstructions and the corresponding truncation points when these are inverted using the square Moore-Penrose method. Also shown is the number of singular values recovered by use of RR-normalization instead of R-normalization.
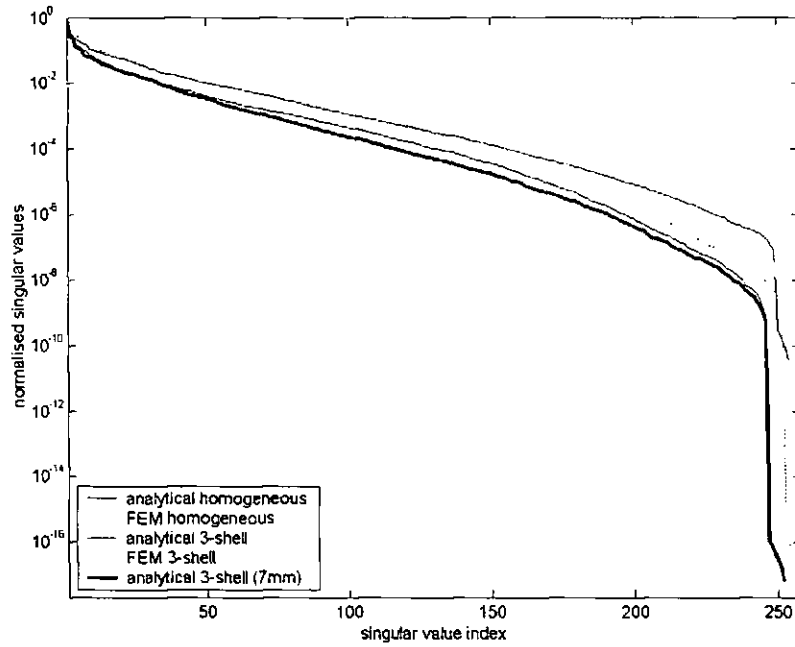
Figure 3-6: Singular value spectra for all matrices $RAC(RAC)^T$ used in reconstructions of tank data.

3.2.6 Analysis of Images

Images were displayed and analysed using TOASTIM, part of the TOAST suite of programmes (Arridge, Hebden et al. 2000), and using Matlab. Three aspects of the different reconstructed images were compared:

- *spatial accuracy* – the loci of peak impedance changes will be plotted and their errors calculated with respect to the loci of the target impedance changes[1].

- *resolution* – since the image is 3-D, the Full-Width at Half-Maximum (FWHM) was found in the xy-plane containing the peak change and also in the z-direction.

- *correlation / image quality* – the percentage correlation of the each reconstructed image $\Delta\sigma^{image}$ and each target image $\Delta\sigma^{target}$ was calculated over k=1,...,N nodes using the following definition

$$corr\% = \frac{\sum_k \Delta\sigma_k^{t\,arg\,et} \cdot \Delta\sigma_k^{image}}{\sqrt{\sum_k \left(\Delta\sigma_k^{t\,arg\,et}\right)^2} \cdot \sqrt{\sum_k \left(\Delta\sigma_k^{image}\right)^2}} \qquad [3\text{-}6]$$

---

[1] All measures of distance were normalized relative to a 92mm sphere for simulations and to a 93.5mm sphere for tank experiments. By this method, results using the 92mm 4-shell sphere model could be compared with those using the 100mm homogeneous sphere, despite their difference in size.

3.3   *Results*

3.3.1   Reconstruction of Numerically Simulated Data

In this section and in subsequent results sections will be shown figures describing image reconstruction for perturbations moving along the x-axis only. These will be tabulated in section 3.3.1.5 along with results for y- and z-movement for ease of understanding.

3.3.1.1   Images

Images are shown in Figure 3-7 of perturbations, simulated numerically, using $A_{4\,fine}^{FEM}$, at positions y = z = 0 and x = [-70, -50, -30, 0, 30, 50, 70]. Four slices were extracted, 15mm apart, with the lowest on the equatorial plane. No significant changes occurred above this. Reconstructed images were normalized, first, according to how many conductivity values were changed in the computer simulation. They were then normalized to the peak of the impedance change in the image. Thus, changes in the images below are seen as having the same magnitude when, in actual fact, for each set of reconstructions, those in the centre were about seven times smaller than those towards the edge. Scales were symmetric about zero for each image.

3.3.1.2   Spatial Accuracy

Results are plotted for reconstructions of perturbations moving along the x-axis of the finely-meshed numerical 4-shell model. In Figure 3-8(i), loci are shown of the peaks in the images reconstructed using A_{hom}^{FEM} (blue) and A_{4shell}^{FEM} (red). These, r_{image}, are projected onto the XZ-plane. A dotted line connects each data point with the corresponding locus of the target perturbation. These loci, r_{target}, are shown in black. Figure 3-8(ii) shows the loci when only the X-coordinate was considered. Again, the target loci are plotted (solid black). Also shown (dotted black) are target loci modified by the correction factor 1.6, suggested by Ary *et al.*(1981) to compensate for the presence of the skull when a homogeneous model is assumed for dipole localization. In general, reconstructed loci lie between these two lines. Localization errors for movement along all axes are summarized in Table 3-4.

HOMOGENEOUS

(i)

4-SHELL

(ii)

Figure 3-7: Normalized images of FEM-simulated perturbations at y = z = 0 and x = [-70, -50, -30, 0, 30, 50, 70] reconstructed using (i) A_{hom}^{FEM} and (ii) A_{4shell}^{FEM}. In each set, rows of images are horizontal slices through the sphere, separated vertically by 15mm, with the lowest through the equator.
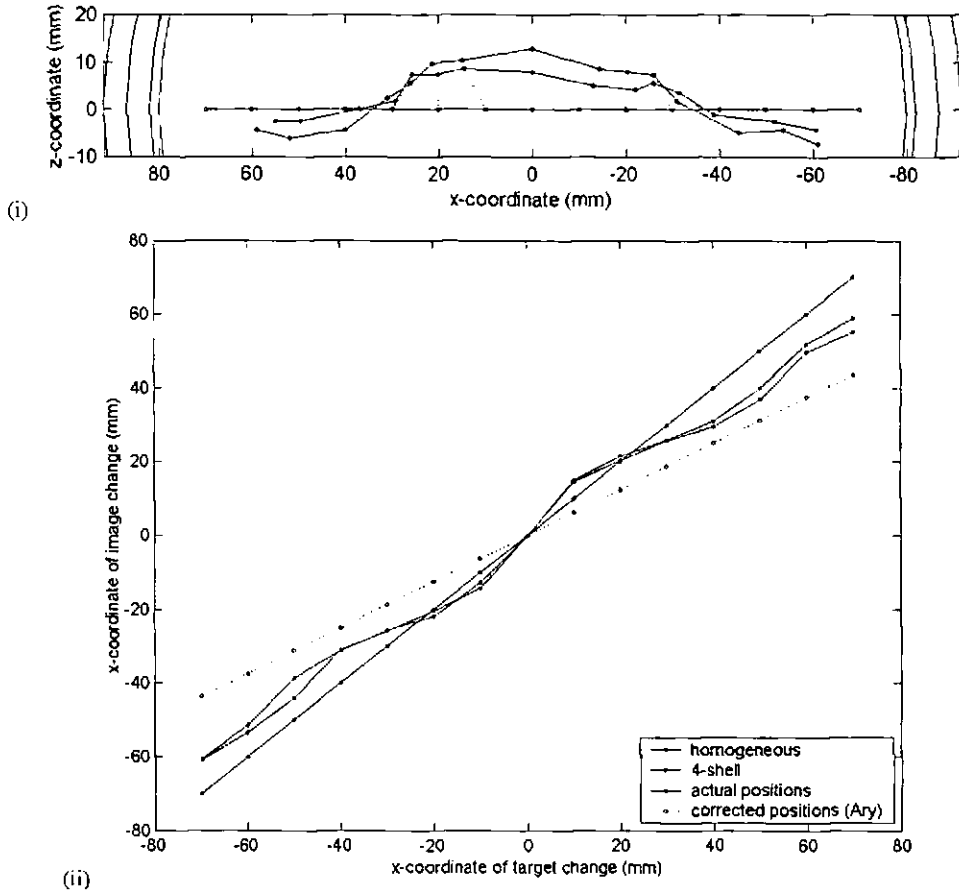
Figure 3-8: (i) 15 target positions (black) along the x-axis and the positions of peaks in 15 images reconstructed using A_{hom}^{FEM} (blue) A_{4shell}^{FEM} (red). (ii) The target x-coordinates and the apparent x-coordinates of peaks in 15 images reconstructed using each matrix. The key in the lower sub-figure applies to both sub-figures.

3.3.1.3   Resolution

Resolution was similar in x- and y-directions in the horizontal XY-plane and results are given as representative of both together. It was much poorer in the vertical z-direction, especially at central locations. Results are shown in Table 3-4 for resolution when target perturbations are moved along all axes. The horizontal and vertical FWHM are shown in Figure 3-9 for movement of a target perturbation along the x-axis only.
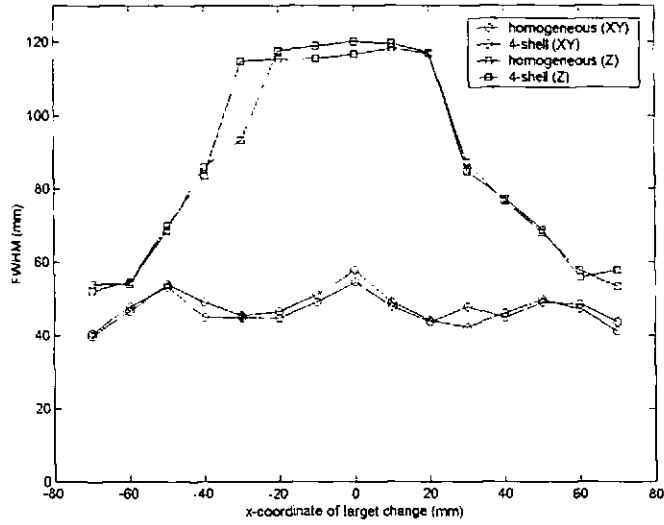
Figure 3-9: The horizontal (circles) and vertical (squares) FWHM for peaks in 15 images reconstructed using A_{hom}^{FEM} (blue) and A_{4shell}^{FEM} (red).

3.3.1.4   Correlation

Percentage correlations are shown in Figure 3-10 of 15 reconstructed images $\Delta\sigma_{image}$ with 15 target distributions $\Delta\sigma_{target}$ of conductivity perturbations moving along the x-axis only. These values were calculated using equation [3-6] and results for all axes are summarized in Table 3-4. Until a radius of about 60mm, correlation appears to improve as the eccentricity of perturbations increases.

Figure 3-10: Percentage correlations of 15 target distributions with 15 images reconstructed using A_{hom}^{FEM} (blue) and A_{4shell}^{FEM} (red).

124

3.3.1.5 *Significance of Results*

Results are summarized in Table 3-4 for reconstructions of simulated movement of a conductivity perturbation in all directions throughout the numerical 4-shell model. Listed are the mean localization error, the FWHM in the XY- and Z-planes and the percentage correlation between target distributions of conductivity change and images reconstructed using the homogeneous and the 4-shell FEM model.

For perturbations simulated in the 4-shell FEM model, there was no significant improvement in localization accuracy when shells were included in the numerical reconstruction and resolution was similar under assumptions of homogeneity and layers.

		Mean localization error (mm)	Mean XY-FWHM (mm)	Mean Z-FWHM (mm)	Mean Correlation (%)
Homogeneous	x	9.7 ± 2.9	47.0 ± 3.8	86.7 ± 26.6	10.0 ± 2.4
	y	10.5 ± 3.4	44.9 ± 6.0	97.2 ± 24.8	8.7 ± 2.7
	z	7.9 ± 4.3	52.7 ± 6.1	72.2 ± 26.2	8.4 ± 3.2
	all	9.6 ± 3.4	47.4 ± 5.2	87.8 ± 25.8	9.2 ± 2.7
4-shell	x	10.0 ± 2.0	47.3 ± 4.7	86.1 ± 26.8	9.9 ± 2.3
	y	10.0 ± 3.1	47.4 ± 7.6	99.0 ± 24.4	8.2 ± 2.9
	z	7.9 ± 3.8	58.9 ± 6.4	74.2 ± 27.8	8.5 ± 3.6
	all	9.5 ± 2.8	49.8 ± 6.4	88.7 ± 26.0	8.9 ± 2.7

Table 3-4: Analysis results for reconstructions using numerical homogeneous and 4-shell models. Data was generated using the numerical 4-shell model for perturbations in 15 positions (-70:70mm), equally spaced along each of the x- and y- axes and 9 positions along the z-axis (-30:70mm).

3.3.2 Reconstruction of Analytically Simulated Data

In this section, again, will be shown figures describing image reconstruction for perturbations moving along the x-axis only. These will be tabulated in section 3.3.2.5 along with results for y- and z-movement for ease of understanding.

3.3.2.1 Images

Images are shown in Figure 3-11 of perturbations, simulated analytically using A_{4fine}^{ANA}, at positions $y = z = 0$ and $x = [-70, -50, -30, 0, 30, 50, 70]$. Four slices were extracted, 15mm apart, with the lowest on the equatorial plane. No significant changes occurred above this.

Reconstructed images were normalized, again, according to how many conductivity values were changed in the computer simulation. They were then normalized to the peak of the impedance change in the image. Thus, changes in the images below are seen as having the same magnitude when, in actual fact, for each set of reconstructions, those in the centre were 2.7, 4.3 and 2.5 times smaller than those towards the edge. Scales were symmetric about zero for each image.

3.3.2.2 Spatial Accuracy

Results are plotted for reconstructions of perturbations moving along the x-axis of the finely-meshed analytical 4-shell model. In Figure 3-12(i), loci are shown of the peaks in the images reconstructed using A_{hom}^{ANA} (blue), A_{4shell}^{ANA} (red) and A_{4shell}^{FEM} (green). These, r_{image}, are projected onto the XZ-plane. A dotted line connects each data point with the corresponding locus of the target perturbation. These loci, r_{target}, are shown in black. Figure 3-12 (ii) shows the loci when only the X-coordinate was considered. Again, the target loci are plotted (solid black), as are those modified by the correction factor 1.6 (dotted black), suggested by Ary *et al.*(1981). In general, reconstructed loci lie between these two lines. Localization errors for movement along all axes are summarized in Table 3-5. Also shown in Figure 3-12 is a plot of the localization error $|r_{target} - r_{image}|$ between expected and reconstructed positions by each reconstruction method.

HOMOGENEOUS

(i)

4-SHELL

(ii)

4-SHELL (FEM)

(iii)

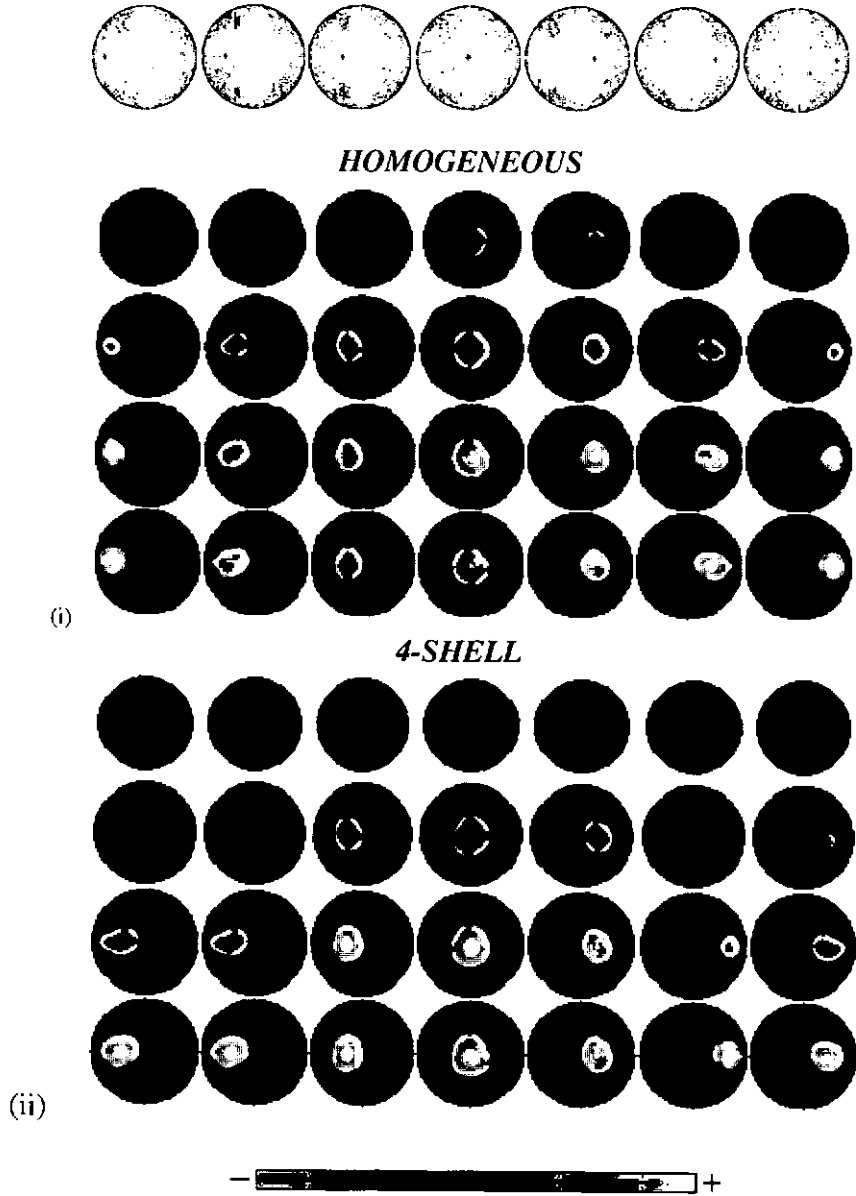$- \;\blacksquare\;\;\;\;\;\;\;\;\;\;\;\; +$

Figure 3-11: Normalized images of analytically-simulated perturbations at y = z = 0 and x = [-70, -50, -30, 0, 30, 50, 70] reconstructed using (i) A_{hom}^{ANA}, (ii) A_{4shell}^{ANA} and (iii) A_{4shell}^{FEM}. In each set, rows of images are horizontal slices through the sphere, separated vertically by 15mm, with the lowest through the equator.

127
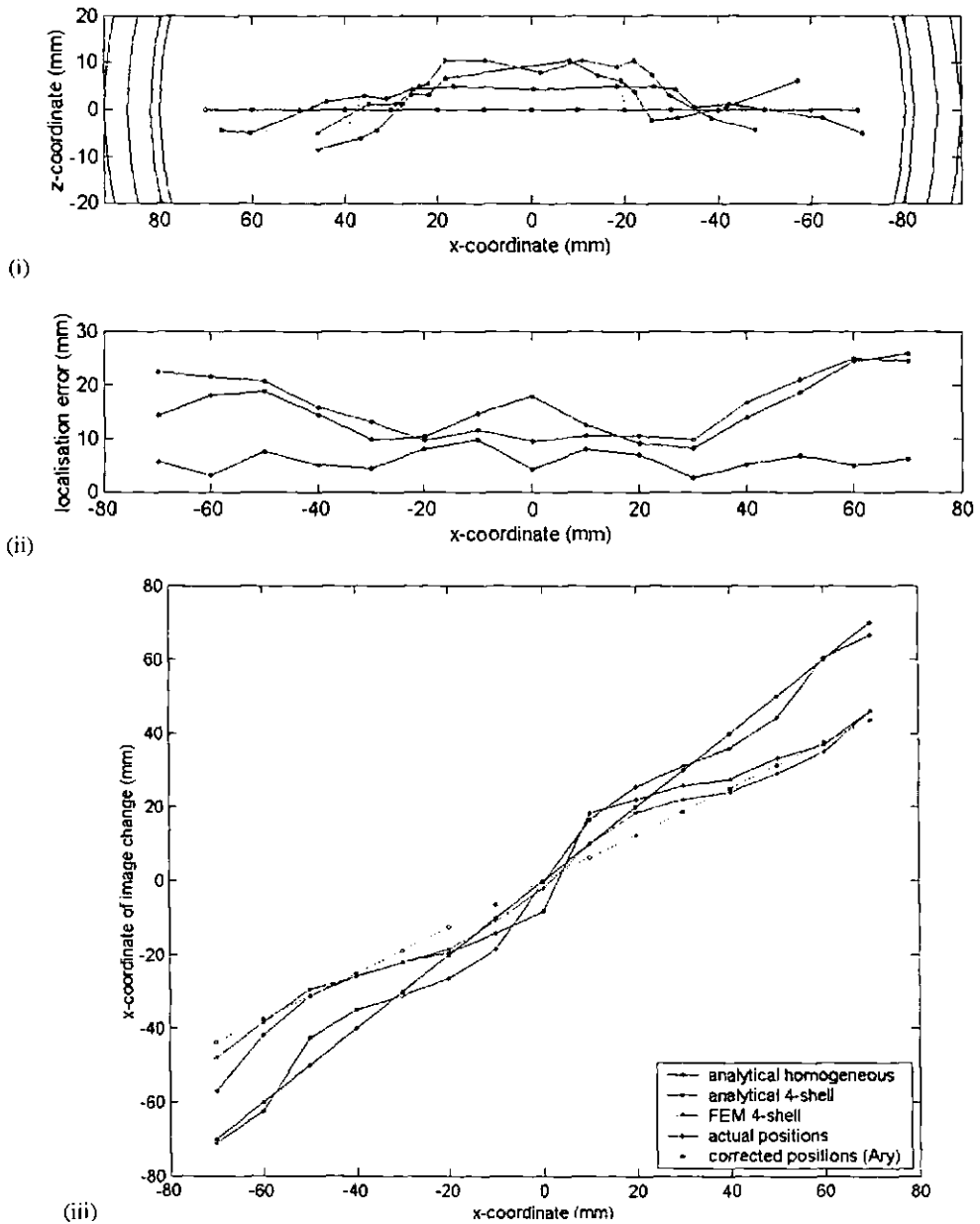
Figure 3-12: (i) 15 target positions (black) along the x-axis and the positions of peaks in 15 images reconstructed using A_{hom}^{ANA} (blue), A_{4shell}^{ANA} (red) and A_{4shell}^{FEM} (green). (ii) The distance between image loci and target loci for reconstructions using each model. (iii) The target x-coordinates and the apparent x-coordinates of peaks in 15 images reconstructed using each model. The key in the lower sub-figure applies to all three sub-figures.

3.3.2.3　Resolution

Again, resolution was similar in x- and y-directions in the horizontal XY-plane so results are given as representative of both together. They are shown in Table 3-5 for resolution in each set of reconstructed images when target perturbations are moved along all axes. The horizontal and vertical FWHM are shown in Figure 3-13 for movement of a target perturbation along the x-axis only.
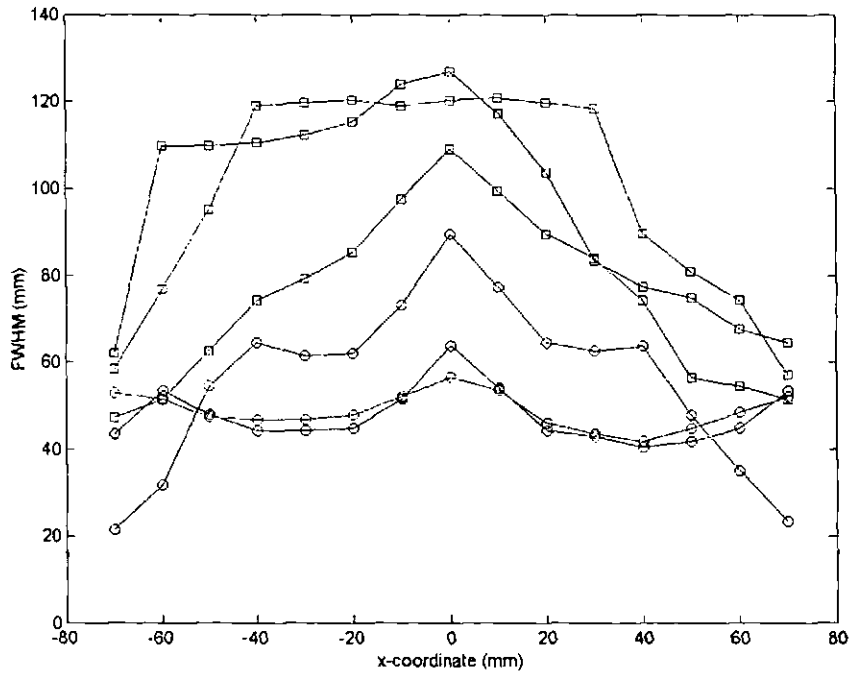
Figure 3-13: The horizontal (circles) and vertical (squares) FWHM for peaks in 15 images reconstructed using A_{hom}^{ANA} (blue), A_{4shell}^{ANA} (red) and A_{4shell}^{FEM} (green).

3.3.2.4　Correlation

Percentage correlations are shown in Figure 3-14 for each set of 15 reconstructed images $\Delta\sigma_{image}$ with 15 target distributions $\Delta\sigma_{target}$ of conductivity perturbations moving along the x-axis. These values were calculated using equation [3-6] and results for all axes are summarized in Table 3-5. Until a radius of about 60mm, correlation appears to improve as the eccentricity of perturbations increases.
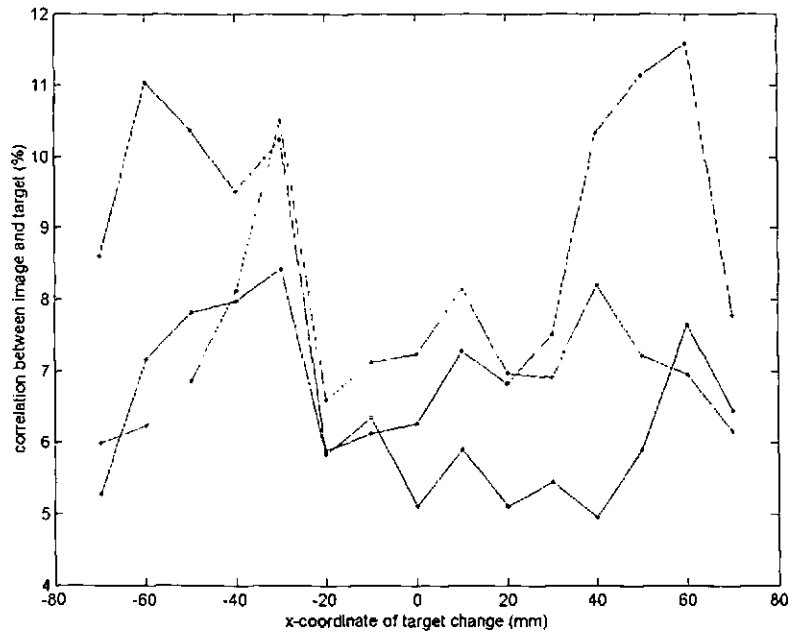
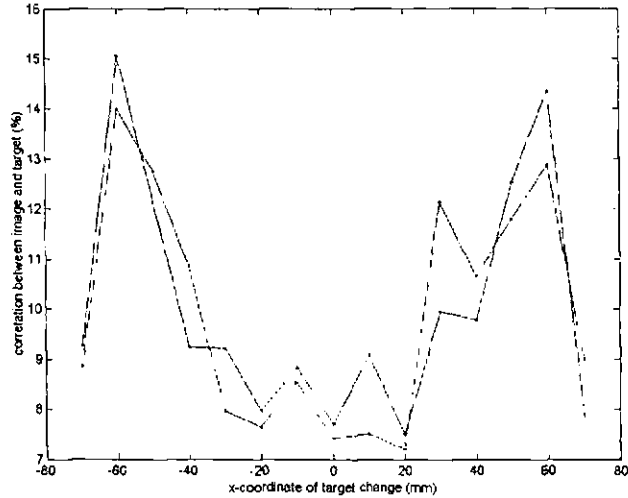**Figure 3-14:** Percentage correlations of 15 target distributions with 15 images reconstructed using A_{hom}^{ANA} (blue), A_{4shell}^{ANA} (red) and A_{4shell}^{FEM} (green).

3.3.2.5 Significance of Results

Results are summarized in Table 3-5 for movement of a conductivity perturbation in all directions throughout the analytical 4-shell model. Listed are the mean localization error, the FWHM in the XY- and Z-planes and the percentage correlation between target distributions of conductivity change and images reconstructed using the homogeneous and 4-shell analytical models and the 4-shell FEM model.

For perturbations simulated by the analytical 4-shell model and reconstructed using both A_{hom}^{ANA} and A_{4shell}^{ANA}, the mean localization error was reduced significantly from $15.8 \pm 6mm$, in the former, to $5.8 \pm 2.2mm$ in the latter($p = 1.7 \times 10^{-11}$ - two-tailed, paired T-test), using a significance level of 5%. No improvement was offered by A_{4shell}^{FEM} over A_{hom}^{ANA} ($p = 0.12$) and it was worse than using A_{4shell}^{ANA} ($p = 1.1 \times 10^{-8}$).

XY-resolution was significantly poorer when A_{4shell}^{ANA} was used ($p = 3.7 \times 10^{-4}$) than when A_{hom}^{ANA} was used. In this case, the FWHM was increased from $49.5 \pm 7.0mm$ (27% of the image diameter) to $57.8 \pm 14.7mm$ (31% of the image diameter). There was no difference in XY-resolution for shelled-FEM reconstruction. Z-resolution was similar using A_{hom}^{ANA} and A_{4shell}^{FEM} but was better than both using A_{4shell}^{ANA} ($p = 0.022$ and $p = 0.004$ respectively).

Inclusion of shells improved correlation in both analytical and FEM reconstructions (p_{ana} = 1.6×10^{-10}; p_{FEM} = 5.9×10^{-7}) from 5.6 ± 1.5% in the homogeneous reconstruction to 8.5 ± 2.2% and 7.2 ± 1.8%, respectively. Correlation by the analytical method was significantly higher than by FEM ($p = 2.6\times10^{-4}$).

		Mean localization error (mm)	Mean XY-FWHM (mm)	Mean Z- FWHM (mm)	Mean Correlation (%)
Homogeneous (analytical)	all	15.9 ± 6.0	49.5 ± 7.0	97.5 ± 22.0	5.6 ± 1.5
4-shell (analytical)	all	5.8 ± 2.2	57.8 ± 14.7	90.6 ± 22.0	8.5 ± 2.2
4-shell (numerical)	all	14.9 ± 6.0	51.1 ± 5.2	98.8 ± 23.1	7.2 ± 1.8

Table 3-5: Analysis results for reconstructions using the analytical homogeneous and 4-shell models and the numerical 4-shell model. Data was generated using the numerical 4-shell model for perturbations in 15 positions (-70:70mm), equally spaced along each of the x- and y- axes and 9 positions along the z-axis (-30:70mm).

3.3.3 Reconstruction of Data from the Shell Tank

3.3.3.1 Images

Images are shown in Figure 3-15, of tank perturbations at positions $y \approx z \approx 0$ and $x = [$-75, -55, -35, 25, 45, 65]. Four slices were extracted, 15mm apart, with the lowest on the equatorial plane. No significant changes occurred above this. Reconstructed images were normalized to the peak of the impedance change in the image. Thus, changes in the images below are seen, again, as having the same magnitude. In reality, for each set of reconstructions, those in the centre of the FEM reconstructions were each 1.8 times smaller than those towards the edge and those in analytical reconstructions, 1.8, 2 and 2,5 times smaller as the effect of the shell became greater. Scales were symmetric about zero for each image. Finally, images were multiplied by −1, which is why changes appear as conductivity increases.

3.3.3.2 Spatial Accuracy

Results are plotted for reconstructions of the Perspex as it moved along the x-axis of the 3-shell tank. In Figure 3-16(i) and (ii), loci are shown of the peaks in the images reconstructed using homogeneous, $A_{homtank}^{FEM}$ and $A_{homtank}^{ANA}$ (blue), and 3-shell $^{5mm}A_{3shelltank}^{FEM}$ and $^{5mm}A_{3shelltank}^{ANA}$ (red) and $^{7mm}A_{3shelltank}^{ANA}$ (green) matrices. These, r_{image}, are projected onto the XZ-plane, a dotted line connecting each data point with the corresponding locus of the target perturbation. These loci, r_{target}, are shown in black. Also shown (Figure 3-16(iii)) is a plot of the localization error $|r_{target} - r_{image}|$ between expected and reconstructed positions using each reconstruction method. Figure 3-16 (iv) shows the loci when only the X-coordinate was considered. Again, the target loci are plotted (solid black). Localization errors for movement along all axes are summarized in Table 3-6.
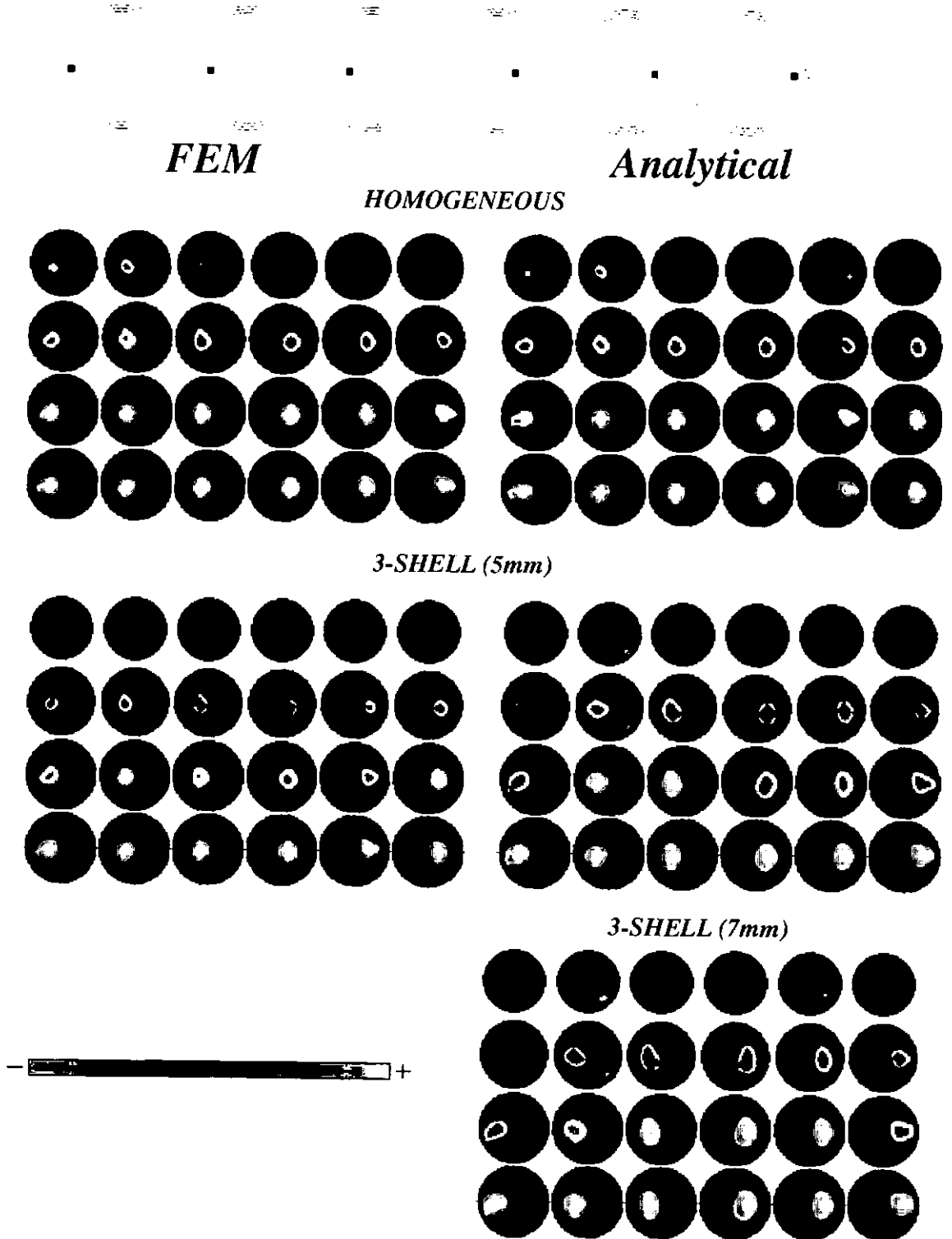
Figure 3-15: Normalized images of Perspex in the shell-tank at x = [-75, -55, -35, 25, 45, 65] reconstructed using two FEM-generated matrices and three analytically-generated matrices. In each set, rows of images are horizontal slices through the sphere, separated vertically by 15mm, with the lowest through the equator.
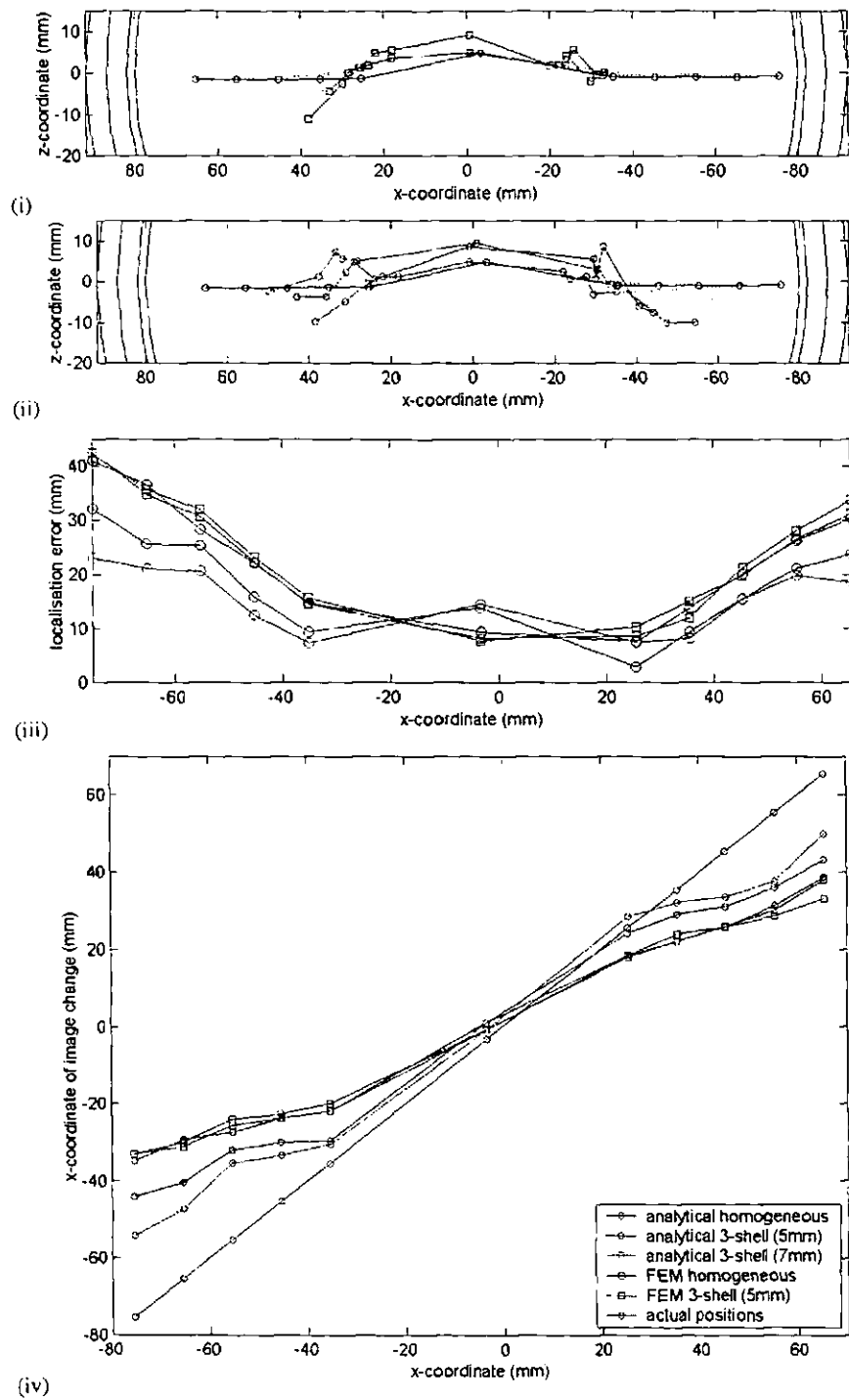
Figure 3-16: Loci of peak impedance changes in images of Perspex reconstructed using (i) $A_{homtank}^{FEM}$ and $^{5mm}A_{3shelltank}^{FEM}$ and (ii) $A_{homtank}^{ANA}$, $^{5mm}A_{3shelltank}^{ANA}$ and $^{7mm}A_{3shelltank}^{ANA}$. (iii) The distance between image loci and target loci for reconstructions using each model. (iv) The target x-coordinates and the apparent x-coordinates of peaks in 11 images reconstructed using each model. The key in the lower sub-figure applies to all three sub-figures.

3.3.3.3 Significance of Results

Results are summarized in Table 3-6 for movement of a Perspex object in all directions throughout the 3-shell tank. Listed are the mean localization error, the FWHM in the XY- and Z-planes and the percentage correlation between target distributions $\Delta\sigma_{target}$ of conductivity change and images $\Delta\sigma_{image}$ reconstructed using the homogeneous and 3-shell analytical and FEM models.

Localization error was not reduced significantly when shells were incorporated in the FEM model for reconstruction ($p = 0.29$). It was significantly lower when shells were incorporated into the analytical model for reconstruction, both when the shell was modelled to be 5mm thick with a conductivity $\sigma_{plaster} = 0.012$ Sm^{-1} and 7mm with conductivity $\sigma_{plaster} = 0.008$ Sm^{-1} ($p_{5mm} = 9.2 \times 10^{-5}$; $p_{7mm} = 6.0 \times 10^{-5}$), in which cases the mean error fell from 20.3 ± 9.9mm to 16.4 ± 7.6mm and 14.0 ± 5.8mm. The 7mm analytical model provided better localization than did the 5mm analytical model ($p = 6.3 \times 10^{-4}$).

XY-resolution was reduced significantly when $^{5mm}A^{ANA}_{3shelltank}$ and $^{7mm}A^{ANA}_{3shelltank}$ were used ($p_{5mm} = 3.1 \times 10^{-13}$; $p_{7mm} = 3.3 \times 10^{-9}$). In these cases, the mean FWHM was increased from 25% of the image diameter to 29% and then 31% as the thickness and resistivity of the shell was increased. The inclusion of shells in the numerical model improved resolution by about 1mm and all FEM reconstructions had significantly better XY-resolution than the shelled analytical reconstructions. All FEM reconstruction gave Z-resolution similar to the analytical reconstruction when a homogeneous sphere was assumed, but analytical shell models gave worse Z-resolution than the homogeneous model.

For tank reconstructions, inclusion of shells did not offer a significant improvement in correlation. For the FEM shell model, correlation was actually slightly lower than for the FEM homogeneous model.

	Mean localization error (mm)	Mean XY-Resolution (mm)	Mean Z-Resolution (mm)	Mean Correlation (%)
ANALYTICAL				
Homogeneous	20.3 ± 9.9	46.1 ± 5.0	78.9 ± 19.0	5.6 ± 2.6
3-shell (5mm)	16.4 ± 7.6	53.1 ± 7.1	84.8 ± 22.3	6.0 ± 2.2
3-shell (7mm)	14.0 ± 5.8	57.7 ± 8.9	81.6 ± 17.5	6.2 ± 1.6
FEM				
Homogeneous	21.1 ± 10.3	45.8 ± 5.3	80.3 ± 20.8	5.6 ± 2.7
3-shell (5mm)	20.8 ± 10.3	44.8 ± 4.3	79.4 ± 20.7	5.2 ± 2.9

Table 3-6: Analysis results for images reconstructed using homogeneous and 3-shell matrices calculated analytically and numerically. Images described Perspex perturbations in the spherical 3-shell tank phantom placed at 29 different locations along the x-, y- and z-axes.

3.4 Discussion

3.4.1 Comparison with Previous Results

It was possible, using the analytical method, to reconstruct images of conductivity perturbations inside a tank phantom with a mean localization error of about 14±6mm and a FWHM of 58±9mm, corresponding to an elliptical half-sensitivity volume (HSV) of about 33% the volume of the object. Resolution was similar to that reported by Gibson for 2-D errors in 3-D hemispherical tank reconstructions using a homogeneous sphere algorithm. However, the spread of error values in the present study was only slightly over one third that reported by Gibson. This suggested less spatial variation of localization accuracy, an asset in a reconstruction algorithm. The mean was 5mm less for the new reconstruction technique but, because of the large spread of values he reported, it was not significantly less. It is unclear how the inclusion of z-error in his results would affect the comparison.

3.4.2 Shells in the Linear FEM

The inclusion of shells made no difference to spatial accuracy and little to resolution when a linear FEM model was used for inverse solutions. The only notable improvement over the homogeneous assumption came for reconstruction of analytically simulated data, when correlation was slightly higher. This suggests that inclusion of layers, by this method, had the effect of reducing noise slightly in the images since the locations and spreads of the peaks were similar. This result concurred with that reported by Bagshaw *et al.* (In press) using a reconstruction algorithm without the post-weighting stage. It was apparent also, by comparison of the two sets of images, that electrode artefact was less using the reconstruction algorithm described above. This is not surprising since the post-weighting process was used here and suppresses heavily changes that occur close to the electrodes. Meshing issues aside, (section 3.2.2.4), I decided not to modify the FEM model similarly to the analytical model, for tank studies, because so little improvement had been gained in reconstruction of simulated data.

The author had more confidence in the analytical than the numerical predictions for the effect of shells on current density. No difference was made to resolution when they were included numerically, which leads him to further doubt the ability of the linear FEM to account for their presence adequately. Further to this, the analytical model predicted the image data set substantially better than did the FEM shell model.

3.4.3　Improvements with the Analytical Shell Model

3.4.3.1　Localization

When an analytical model was used to account for shells in the reconstruction process, spatial accuracy was improved by 10mm and 6mm in analytical simulation and tank studies. The maximum localization error was 9.5mm for movement along the y-axis, as compared with 32mm, reported previously (Liston, Bayford et al. 2002), so it would appear that post-weighting and correct row-normalization improved reconstruction. When only the radial displacement was considered, it was seen in Figure 3-12(iii) and Figure 3-16(iv) that peaks were located too centrally, as was expected, when homogeneity was assumed. A correction factor 1.6 was applied to the target loci to give theoretical corrected loci. These were plotted in Figure 3-12(iii) along with those loci for homogeneous and FEM 4-shell reconstructions. Those reconstructed loci appeared to be closer to the corrected loci than to the original target loci. However, although this suggests that either of these models could be assumed for reconstruction if a factor was applied afterwards, none of the loci plotted above described straight lines. Further to this, were the factor to have been applied to the homogeneous- and FEM 4-shell-reconstructed loci, several of the most eccentric loci would have described a perturbation outside the skull. Therefore, it is unwise to apply a correction factor blindly.

The correction factor was not necessary when the analytical shell model was assumed to reconstruct analytically simulated data. For analytical reconstruction of tank data, the inclusion of shells improved localization but, although peaks were less central than for homogeneous reconstruction, they were still slightly more central than the target perturbations. Again the loci did not describe a straight line and blind application of a correction factor may have located perturbations outside the skull. It may have been that imperfections in the manufacture of the spherical shell introduced error to the results but the experiment revealed the tendency of the analytical, layered model to locate impedance changes less centrally and more accurately than a homogeneous model for measured data in the presence of shells.

3.4.3.2　Resolution

Large *out-of-plane* changes were seen in Figure 3-7 and Figure 3-15. In other words, changes were observed in the images, relating to the target perturbation, in planes other than that which contained that target perturbation. This was the case because Z-resolution was very poor in all reconstructions, as a result of the arrangement of electrodes. Whilst there

were electrodes placed symmetrically around the z-axis, giving reasonable XY-resolution, there were only 4 electrodes below the equator (Figure 2-1(iii) and (iv)) so it was impossible to attain the same resolution in the z-direction.

For tank and computer simulation, the mean spread in the XY-plane was increased by a few percent when shells were included, analytically, in the reconstruction. The FWHM was increased from about one-quarter to almost one-third the image diameter. The difference can be seen clearly upon inspection of the images. Resolution is already known to be low in EIT. When surface electrodes are used to study an object, it is higher near the surface, where current density is high, than deeper inside. It is not surprising that, since current density in the brain is reduced by the presence of a skull, as seen in the previous chapter, the work above has shown resolution also to be reduced.

3.4.3.3   Correlation

Although correlation was improved by the inclusion of shells in an analytical, spherical model, it was still not remarkably high. Study of planes below the equator revealed smoothly varying changes of a high magnitude relative to those in the upper hemisphere. The process of post-weighting amplified changes in regions of low sensitivity while suppressing those in regions of high sensitivity, as seen in Figure 2-4. Since the truncated inversion process loses information, these may have been exaggerated when C-normalization was applied to the inverted matrix in compensation for the C-normalization before inversion. When only the upper hemisphere was considered, correlation rose by several percent in all instances. It is likely that an iterative solution would improve these figures further by reducing the noise in regions distant to the perturbation.

3.5   Conclusion

In conclusion, for ideal geometry, it is desirable to include shells in a reconstruction algorithm when they are present in the object under study. It does not appear, however, that a linear FEM takes shells into account as well as an analytical shell model, which outperforms not only a homogeneous model, but also the FEM shell model for both tanks and simulations. Whilst reducing resolution, the inclusion of layers in an analytical model for reconstruction draws changes towards the surface and, as a result leads to higher localization accuracy for single impedance changes within concentric spherical shells.

The Effect of Geometry

4 The Effect of Geometry

4.1 Introduction

4.1.1 Analytical versus FEM

In Chapter 3, by imaging perturbations inside concentric spheres, benefits were shown of using an analytical model over a linear FEM model in a reconstruction algorithm intended to account for layers. One might reasonably ask, not simply whether it could provide better images from human data than could a homogenous sphere model, but whether it could perform similarly or better than a full, linear, FEM head model, which incorporated both layers and correct geometry. Although the analytical model contains incorrect information about the geometry of the head, it may account for the effect of layers more successfully than could the FEM model. It is not clear which effect will dominate.

4.1.2 Layers and Realistic Geometry

A review can be found in section 1.7.3.2 of investigations into the effects of including geometry and layers in EEG inverse modelling. There is only one preliminary study to report of their inclusion in EIT (Bagshaw, Liston et al. In press) for data from a realistic, head-shaped tank. However, it did not use the post-weighting method described in section 2.1.5.3 and the row-normalization method was not ideal (section 2.5.1.2). A further inadequacy of the study was that models assumed electrode positions as in the previous chapter for an ideal sphere (Figure 2-1(iii) and (iv)), whereas they should have been as measured in the head-shaped tank and shown in Figure 4-5. The actual positions are tilted so that the anterior electrodes are almost 30mm above the equator and the posterior electrodes over 10mm below it. The z-error dominated localization error for posterior targets in that study and it is likely that this was contributed to significantly by inaccurate definition of electrode positions.

In the past, for homogeneous, spherical reconstructions of tank images, where the tank had realistic geometry and contained a real human skull, peak changes were too central and localization could have been improved by application of a radial correction factor (Tidswell, Gibson et al. 2001b). When human images were reconstructed by this method, results were less easy to interpret. It was not obvious that they could have been improved by the inclusion of shells alone in the model. If that were to have been the case, images may have made more physiological sense merely by application of such a correction factor.

Gibson (2000) included a realistic FEM model of the head for reconstruction of both tank and human images but found no improvement over the homogeneous sphere model in localization or interpretability. However, he was concerned about the quality of the mesh he used to produce the FEM solution. Use of a higher quality mesh is likely to represent the capabilities of FEM more justly. Such a mesh was used by Polydorides *et al.* (2001) and he reported successful reconstructions of simulated impedance changes in the back of the head. However, by his method two-thirds of the electrodes were concentrated near the region of interest, thus biasing the solution towards that region. No localization accuracy was reported and no comparison was made to spherical reconstruction.

It is unclear exactly how modelling both shells and realistic geometry will affect EIT of non-spherical, inhomogeneous objects but it was seen in Chapter 3 that a more accurate forward model produced more accurate inverse solutions. If the advantage of including layers outweighed the advantage of including geometry, it would be sensible to use the analytical multi-shell sphere model for functional imaging of human brain function. If the opposite was the case, the full linear FEM model would be more appropriate, even if it took into account the presence of layers only partially, as suggested in the previous chapter.

4.1.3   The Target Image for Human Studies

It is easy to predict the desired result for reconstruction of tank images since the internal conductivity perturbation is known. However, from the evidence of functional brain imaging studies (see section 1.2.2.2.11), prediction becomes more difficult for study of human subjects using EIT since it relies on precise knowledge of changes in CBV. From brain anatomy and from fMRI and PET studies, visual stimuli are expected to result in increased activity in the *visual cortex*, which lies in the occipital lobe (see section 1.2.2.1) at the back of the brain. Less is known about changes elsewhere due to increased activity or suppression of activity in other regions although they have been observed in PET studies (Mentis, Alexander et al. 1997). It is possible, that the changes in CBV accompanying evoked responses could occur throughout the brain, having opposite polarity, even in regions adjacent to one another. EIT of evoked responses will obtain images that reflect this but a measure of their accuracy will be difficult to make in comparison with tank images for which the target image is well known.

4.1.4 Purpose

It is the purpose of this chapter to report the effect on image reconstruction of including geometry in the forward model of conduction when the object under study is layered and non-spherical. In doing so will be assessed the relative benefits of including layers and including realistic geometry.

4.1.5 Design

Image data was acquired, by Dr Tom Tidswell, a former member of this research group, from a tank phantom made in the shape of a real human head. To investigate the effect of geometry alone, the tank was filled with saline and a perturbation placed at different locations. Images were then reconstructed using an analytical model of a homogeneous sphere and a FEM model of a realistically-shaped homogeneous head.

To investigate the effect of geometry in the presence of shells, a perturbation was moved inside a real human skull, placed inside the head-shaped phantom. Reconstructions were then performed using two analytical sphere models (homogeneous and layered) and two realistically shaped FEM models (homogeneous and layered). The dual effect of geometry and shells was further investigated by reconstruction of human data acquired during evoked response (EP) experiments performed by Dr Tidswell.

No computer simulations were performed in this study since these must rely on the FEM model and it was unlikely, therefore, that these would have taken into account the presence of shells to the degree required for the proposed tests.

4.2   Methods

4.2.1   Tank Data

4.2.1.1   The Head-Tank

A head-shaped phantom was constructed by Dr Tidswell and Dr David Holder from a silicone rubber cast of a head shaped model made from a human skull covered with clay. Thirty-one Ag/AgCl electrodes of 1 cm diameter were embedded into the inner walls of the tank during the casting process. These can be seen in Figure 4-1. The upside-down tank was homogeneous and was filled through the neck with 0.2% saline which had a resistivity 2.37±0.02Ωm (Tidswell *et al* 2001b), similar to that of the brain.

4.2.1.2   The Skull-Tank

The same head-shaped phantom was used to investigate the effect of the skull on reconstructed images (Figure 4-1). Inside the tank was placed a human skull whose resistivity, measured at nine different positions, was 208.0±2.1Ωm (Tidswell, Gibson et al. 2001a).

4.2.1.3   Collection of Data

Through the neck a narrow piece of doweling was inserted in order to suspend a 6.3cm^3 cylinder of Perspex (length 2cm, diameter 2cm) at various positions within the head tank, introducing a 100% conductivity decrease as for tank studies in the previous chapter. The doweling was present throughout the baseline and stimulus epochs.

For experiments in the skull-tank, data were measured using the Hewlett-Packard 4284A-based EIT system, described in section 1.5.3, and delivering a current of 1-3mA at 10kHz (Tidswell, Gibson et al. 2001a). For homogeneous experiments, data were collected using the UCLH Mark 1b EIT system, delivering 2.2mA at 38 kHz (Yerworth *et al* 2002). As in the previous chapter, those channels with high levels of noise or drift were set to zero.

Changes were introduced, with and without the skull, at 12 positions along the anterior-to-posterior direction and at 10 positions from left to right, all measured relative to the position of the foramen magnum (Figure 4-1).

Figure 4-1: The head shaped tank phantom shown with the two halves separated and a human skull inside.

4.2.2   Human Data - Visual Evoked Responses (VER)

For *visual evoked response* (*VER*) experiments, 14 normal volunteers were studied. Each was presented with an 8Hz alternating chequerboard at a distance of 30cm., a baseline reading was taken for 150 s, followed by stimulus for 75 s and then recovery for a further 150 s. 12 experiments were performed on each. However, experiments were only considered for reconstruction if more than three-quarters of the image data set showed satisfactory noise and drift characteristics over time. Since it was not possible to average over time (due to low sampling fs=0.04Hz), it was necessary to average over experiments for each subject. Therefore, if less than 6 experiments could be considered for any one subject, that subject was not included. 7 subjects had to be eliminated from the study so only 7 are considered here.

4.2.3   The Forward Problem

4.2.3.1   Physical Models and Meshing

Three further geometries were required for meshing, further to the homogeneous and 3- and 4-shell spheres described in the previous chapter. These were a homogeneous head-shape (*homogeneous-head*), the same head-shape containing a human skull (*skull-head*) and that of a full, layered human head containing brain, CSF, skull and scalp (*full-head*). The full head model also contained a cavity to represent the air-space behind the nose.

I-DEAS was used to generate meshes describing realistic head geometry with linear, tetrahedral elements (Bayford, Gibson et al. 2001). The head shaped meshes were produced by Andrew Tizzard using a solid model generated using lofted, 2-D non-uniform rational B-spline (NURB) surfaces of the head, skull, CSF and brain (Figure 4-2). The NURB outlines were obtained by segmentation of MRI image slices. The skull used segmented MRI section data as a basis for the form but these proved inadequate in themselves for generating accurate surfaces for the jaw, eye socket and nasal cavity geometry. Additional data were acquired in the form of photographs of anatomical models and reconstructed images from the Visible Human Project and these were used *creatively* to complete the generation of internal surfaces. These were cast as image planes for surface modelling (www.nlm.nih.gov/research/visible/visible_human.html). These data also enabled more realistic modelling of the brain and spinal column to be carried out, as well as some idealised representation of vertebrae from C1 to C3. It was again necessary to partition the geometrical volume, although this was done by a different method than for the spherical meshes. It was not as apparent when a plot was made of the nodal support throughout the head, as in section 2.2.1.3.

The surface meshes for the four compartments, described above, are shown in Figure 4-2, and nodal clouds, in Figure 4-3, colour-coded for tissue type, for the skull-head mesh, the 4-shell sphere mesh and the full, layered head mesh. The numbers of nodes and elements are listed for each in Table 4-1, along with the ratio of largest-to-smallest element, a measure of mesh quality. Larger values indicate poor quality. The layered meshes of realistic head geometry were poorest but these compared well with the linear and quadratic meshes used by Gibson (2000) (ratios 40,000 and 170,000 respectively).

	Number of nodes	Number of elements	Ratio of largest-to-smallest element-volume
Homogeneous Sphere	24734	130229	49
4-Shell Sphere	22420	106825	66
Homogeneous Head-Shape	13610	63992	179
Head-Shape with Skull	16983	86775	2050
Full Head with 4 layers	19773	103606	1605

Table 4-1: Listed are the five meshes used in this chapter, the number of nodes and elements in each and the ratio of largest-to-smallest element size in each, a measure of their quality. A smaller value is desirable.
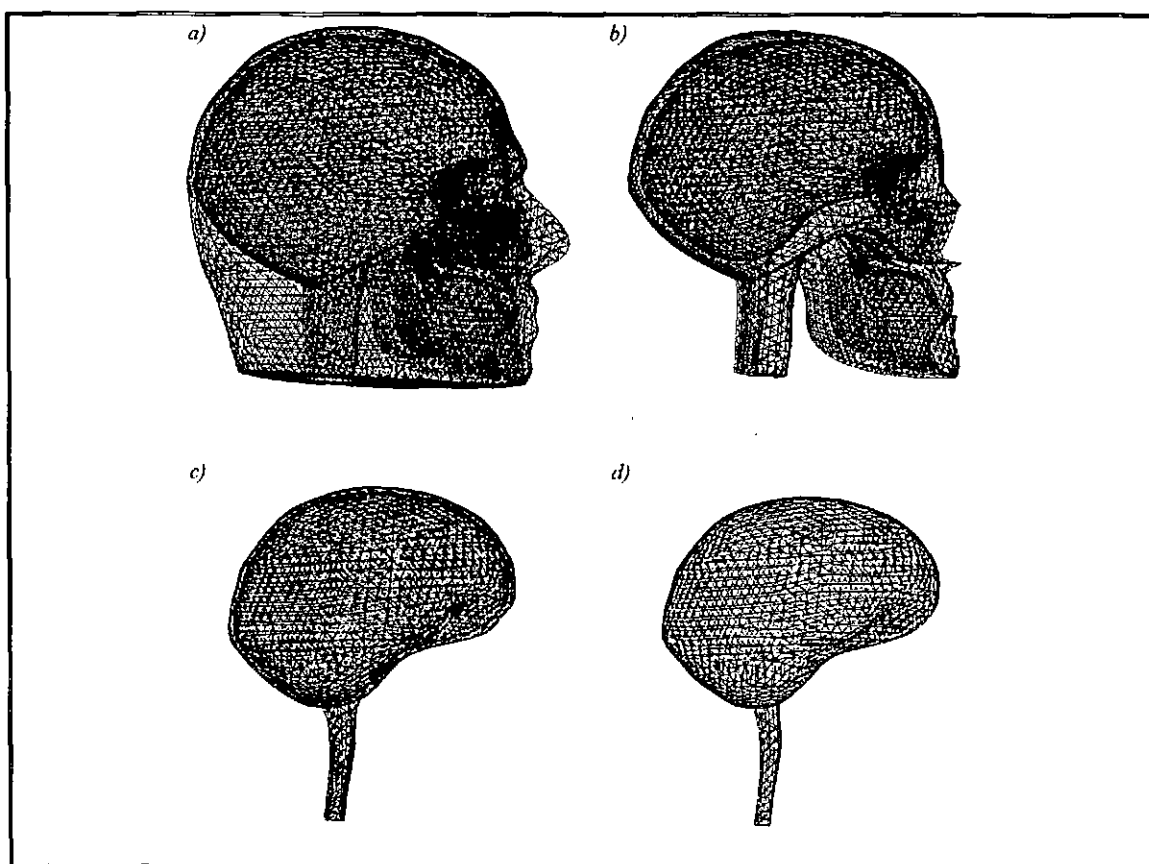
Figure 4-2: The element faces on the surfaces of the four parts of the full, layered head mesh a) the scalp. b) the skull, c) the CSF and d) the brain region. The scalp region contains 8067 nodes, the skull region 6122 nodes, the CSF region 2018 nodes and the brain region 3566 nodes.
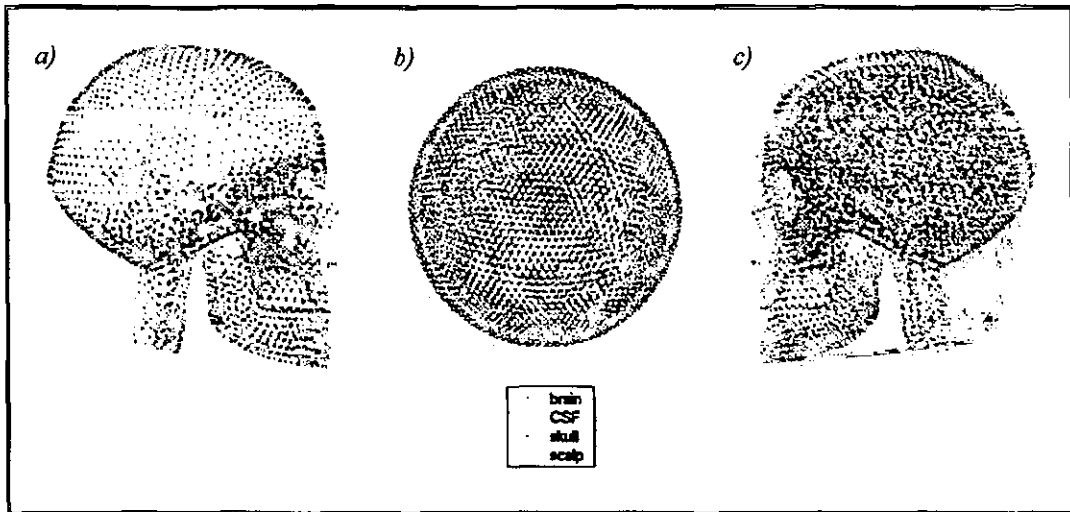
Figure 4-3: The nodal clouds describing a) the head-shaped mesh with skull compartment. b) the four-shell mesh and c) the full, layered head mesh. The different tissues are colour-coded as shown in the key.
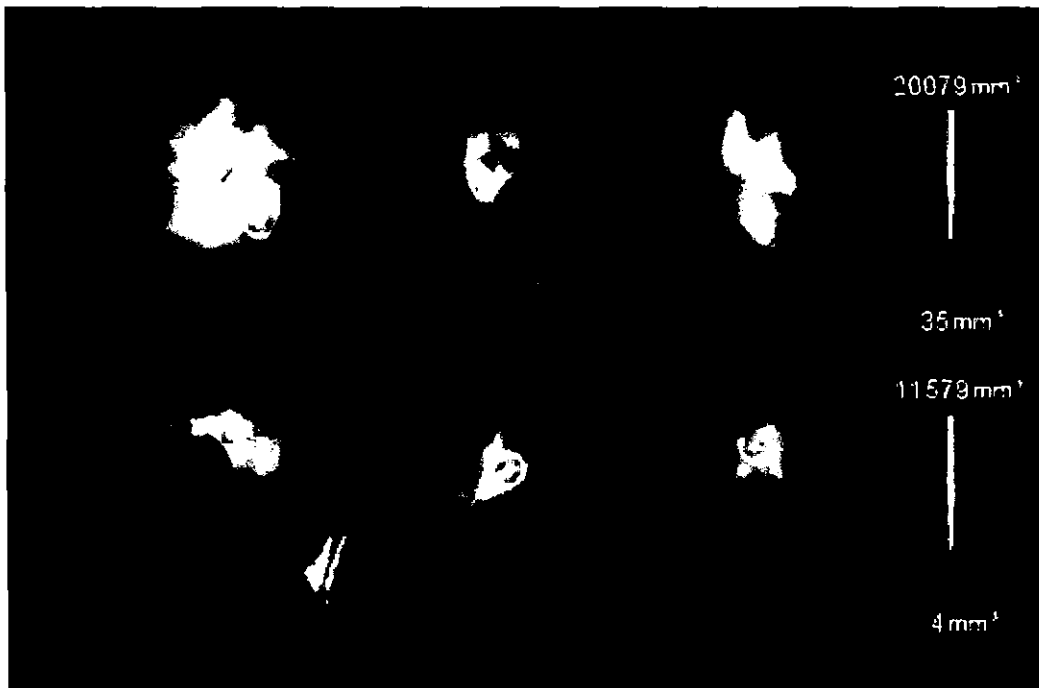
Figure 4-4: The figure is a representation of the *support* throughout the full, layered head mesh (divided by 4 so that its sum is equal to the total volume of the sphere) and through the homogeneous head-mesh.

148

4.2.3.2 Electrode Positions, Mesh Co-Registration and Warping

The electrode positions were measured on the inside of the head tank with 3-D digitising arm. It was assumed that these would represent the positions of electrodes on human subjects better than would the ideal positions for a sphere (section 2.1.2.4), which have been used in the past for human studies and tank studies (Tidswell, Gibson et al. 2001b; Bagshaw, Liston et al. In press). The measured positions were translated and rotated so that they were no longer upside-down, so that the front of the head faced in the negative y-direction and so that the origin was defined as the mid-point of the line joining electrodes 17 and 13. These then defined the x-axis and will be referred to as the *orienting electrodes*.

The centre O_{sphere} and radius R_{sphere} were found for the sphere best described by the new positions of the 31 electrodes. The mean distance from the electrodes to the best-fitting spherical surface was 6.1±4.0mm. For solution to the analytical forward problem, O_{sphere} was subtracted from the positions and they were then multiplied by $100/R_{sphere}$ or $92/R_{sphere}$ so as to fit to the surfaces of the homogeneous and 4-shell meshes respectively. In both analytical and FEM solutions, the boundary node nearest each magnified real-electrode position was defined as the new model-electrode position. The mean distance between each measured electrode position and the node assigned to that electrode, on the surface of the head mesh, was 4.7±1.4mm.

A geometrical correction, or *warping*, was then introduced for the spherical meshes, similar to that suggested by Yvert *et al.* (1997). Y-coordinates less than zero were multiplied by 1.195, the ratio of the mean y-coordinate of the two most anterior electrodes in the head model and the sphere model. Y-coordinates greater than zero were multiplied by 1.032, the ratio of the mean y-coordinate of the two most posterior electrodes in each model. All x-coordinates were multiplied by 0.885, the ratio of the x-coordinate of orienting electrode 13 in each model.

Figure 4-5(i) shows the nodes of the mesh and the model-electrode positions for the FEM solution (black) and those for the homogeneous analytical solution, translated by O_{sphere} and magnified by $R_{sphere}/100$ (red) for co-registration. The resultant, warped mesh, and the corresponding, warped electrode positions, are shown in Figure 4-5(ii). The forward solution was calculated using the spherical mesh but reconstructed images were projected onto the warped mesh for image analysis.
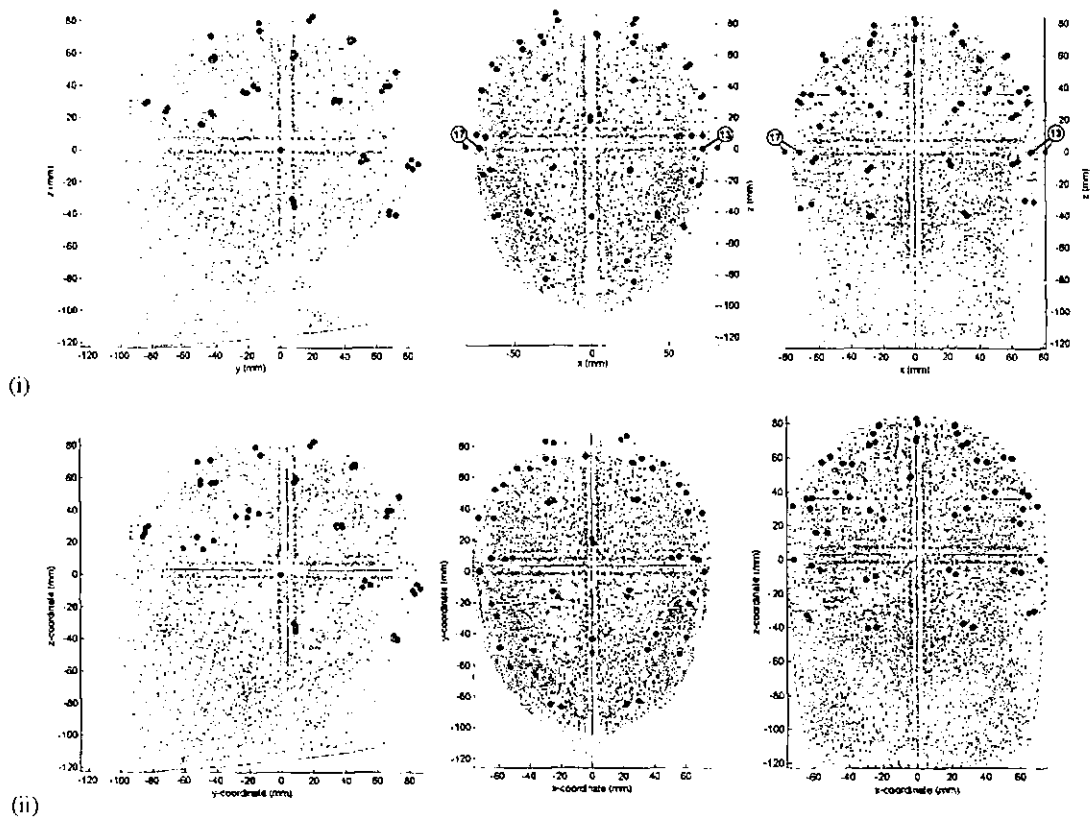
Figure 4-5: (i) The head-shaped mesh (black), the spherical mesh (red) and the corresponding electrode positions used to solve the forward problem for each. Meshes and electrode positions are coregistered so that their origin is the mid-point of the line joining electrodes 17 and 13. (ii) The head-shaped mesh (black), the warped spherical mesh (red), and the electrode positions, coregistered in the same way.

4.2.3.3   Current Density

The current density was calculated for injection through electrodes 17 and 13 and the distribution of its magnitude is shown in Figure 4-6 for the four-layered head model. It can be seen that it differs from the analytical solution for concentric spheres in the same fashion as did the numerical solution presented in Chapter 3 (Figure 2-6).
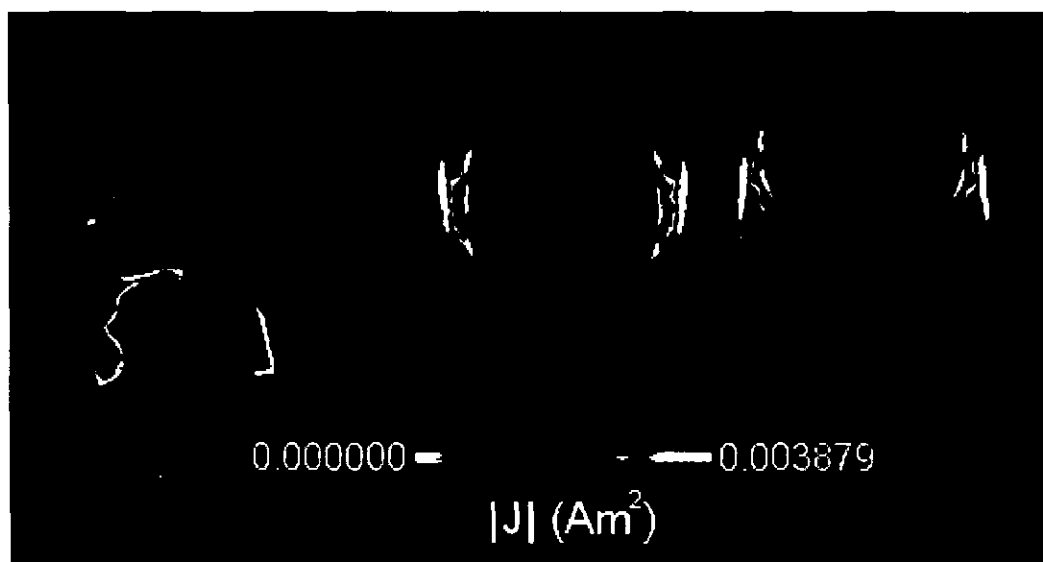
Figure 4-6: Plots (on a log colour scale) of |J| through three orthogonal cross-sections of the full-head mesh, calculated numerically using the linear, MaTOAST FEM implementation.

4.2.3.4   Sensitivity Matrices

For the head tank and human studies, new sensitivity matrices were generated for all geometries, taking into consideration the measured electrode positions in the head tank and using correct conductivity values. These values were as listed in section 4.2.1 for the tank matrices and as listed in Table 1-2 for human studies. For tank studies, homogeneous matrices $A_{headtank}^{ANAhomsphere}$ and $A_{headtank}^{FEMhomhead}$ were generated for reconstruction assuming homogeneity and shell-matrices $A_{headtank}^{ANA3shellsphere}$ and $A_{headtank}^{FEMskullhead}$, assuming layers. Matrices $A_{human}^{ANA4shellsphere}$ and $A_{human}^{FEMfullhead}$ were generated for reconstruction of human data assuming 4 layers. All sensitivity matrices used in this chapter are listed in Table 4-2.

4.2.4 Reconstruction

4.2.4.1 Spherical & Homogeneous ⇒ Head-shaped & Homogeneous

$(\Delta v_n^{homheadtank})_{i=1,...,22}$, the normalized data sets acquired from the homogeneous tank during perturbation experiments, were reconstructed using the numerical matrix $A_{headtank}^{ANAhomsphere}$ and $A_{headtank}^{FEMhamhead}$ described in the previous section. This was in order to assess the effect of geometry alone in reconstruction when it was included in the forward model.

All the following reconstructions were by square Moore-Penrose inversion (section 1.3.4.2) of a reduced matrix, as described by equation [2-18] with truncation performed at 0.1%, as in the previous chapter. The condition of each matrix was similar when homogeneity was assumed. For spherical reconstruction, 100 singular values were included and for head-shaped, 90. The numbers of singular values included for all reconstructions are listed in Table 4-2.

4.2.4.2 Spherical & Homogeneous ⇒ Head-shaped & Layered

4.2.4.2.1 Skull-Tank

$(\Delta v_n^{skulltank})_{i=1,...,22}$, the normalized data sets acquired from the skull-tank during perturbation experiments, were reconstructed using the homogeneous matrices $A_{headtank}^{ANAhomsphere}$ and $A_{headtank}^{FEMhamhead}$ and the 3-layer matrices $A_{headtank}^{ANA3shellsphere}$ and $A_{headtank}^{FEMskullhead}$, described in the previous section. This was in order to assess the effect of geometry and layers when they were included in the forward model.

All matrices were similarly conditioned except that for the analytical shell model, which required truncation after just 56 singular values (Table 4-2).

4.2.4.2.2 Human Data

Visual evoked response data were reconstructed using the homogeneous matrices $A_{headtank}^{ANAhomsphere}$ and $A_{headtank}^{FEMhamhead}$ and the 4-layer matrices $A_{human}^{ANA4shellsphere}$ and $A_{human}^{FEMfullhead}$ in order to assess further the effect of including layers and geometry.

The analytical shell model again produced the most poorly conditioned matrix, and required truncation after 72 singular values (Table 4-2).

	Sensitivity Matrix	Truncation Point	To reconstruct...
Homogeneous Sphere	$A_{headtank}^{ANAhomsphere}$	100	All data
Homogeneous Head-Tank	$A_{headtank}^{FEMhomhead}$	90	
3-Shell Sphere	$A_{headtank}^{ANA3shellsphere}$	56	Data from skull-tank only
Head-Tank with Skull	$A_{headtank}^{FEMskullhead}$	104	
4-Shell sphere	$A_{human}^{ANA4shellsphere}$	72	Human data only
Human Head	$A_{human}^{FEMfullhead}$	91	

Table 4-2: A table listing the sensitivity matrices used for reconstructions of tank and of human data and the corresponding truncation points when these were inverted using the square Moore-Penrose method.

4.2.4.3   Analysis of Images

Before analysis, spherical images were projected onto the egg-shaped mesh described in section 4.2.3.2. All nodal images were then rasterized onto a grid of 3mm cubic voxels and displayed using an imaging suite called Nim, developed for Matlab by Dr Tom Tidswell.

For tank images, spatial accuracy was considered in the localization of Perspex, as was the resolution of the peak. For visual evoked response images, a different approach was adopted since the target image was not so well defined. The Nim display program allowed the user to pick a voxel and could then perform a search for a local peak. The search algorithm was not highly sensitive so, on several occasions, it was necessary to perform the search manually by scanning through image slices. The locations of secondary peaks were recorded if their magnitudes were over about one-quarter that of the peak change. Loci were examined for consistency between algorithms for the same subject and for consistency with the expected neurophysiological response. Since the target image was not known, and multiple changes may have occurred in the same vicinity, qualitative measures of resolution were made in order to compare reconstruction using different models.

4.3 Results

4.3.1 Reconstruction of Data from Homogeneous Tank

4.3.1.1 Images

Images are shown in Figure 4-7 of the Perspex insulator inside the homogeneous head-phantom at positions y = 43mm, z = 2 and x = [-45, -25, -5, 5, 25, 45] relative to orienting electrodes 17 and 13. They were reconstructed using $A_{headtank}^{ANAhomsphere}$ and $A_{headtank}^{FEMhomhead}$. Four slices were extracted, 15mm apart, with the lowest on the plane containing the orienting electrodes. No significant changes occurred above the highest slice. Each image was normalized to the peak of the impedance change in that image. Thus, peaks in the images below appear to have the same magnitude when, in actual fact, for each set of reconstructions, those in the centre were about one-third and two-thirds those towards the edge. Scales were symmetric about zero for each image.

The images reconstructed using $A_{headtank}^{ANAhomsphere}$ are shown projected onto a warped version of the homogeneous spherical mesh. This was in order not to bias the eye further than is necessary when comparing the sets of images and proves useful for blind testing of human images.

4.3.1.2 Spatial Accuracy

Results are plotted for reconstructions of the Perspex as it moved in the left-to-right and anterior-to-posterior directions. In Figure 4-8(i) and (ii), are shown the loci of peaks in images reconstructed using matrices for a homogeneous sphere, $A_{headtank}^{ANAhomsphere}$ (blue), and for a homogeneous head-shape, $A_{headtank}^{FEMhomhead}$ (red). The loci, r_{image}, were projected onto the XZ-plane and the YZ-plane, a dotted line connecting each data point with the corresponding locus of the target perturbation. These loci, r_{target}, are shown in black. For spherical reconstruction, results are shown for the peak position after application of a geometrical correction (see section 4.2.3.2).

PERSPEX IN HOMOGENEOUS PHANTOM

SPHERICAL

(i)

HEAD-SHAPED

(ii)
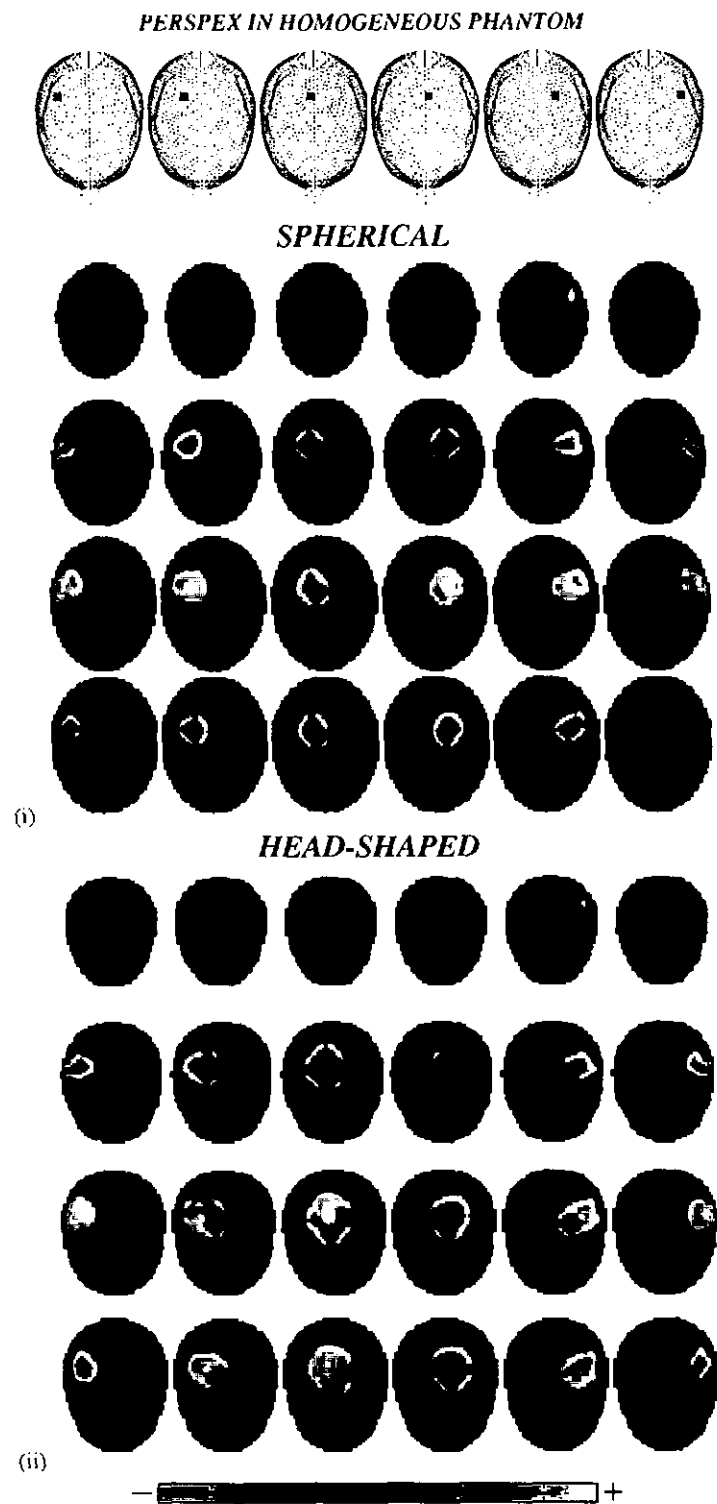
Figure 4-7: Normalized images of Perspex in the homogeneous head-phantom at x = [-45, -25, -5,

5, 25, 45] reconstructed using (i) $A_{headtank}^{ANAhomsphere}$ (ii) and $A_{headtank}^{FEMhomhead}$. In each set, rows of

images are horizontal slices through the model, separated vertically by 15mm, with the lowest

through the orienting electrodes 13 and 17.

155
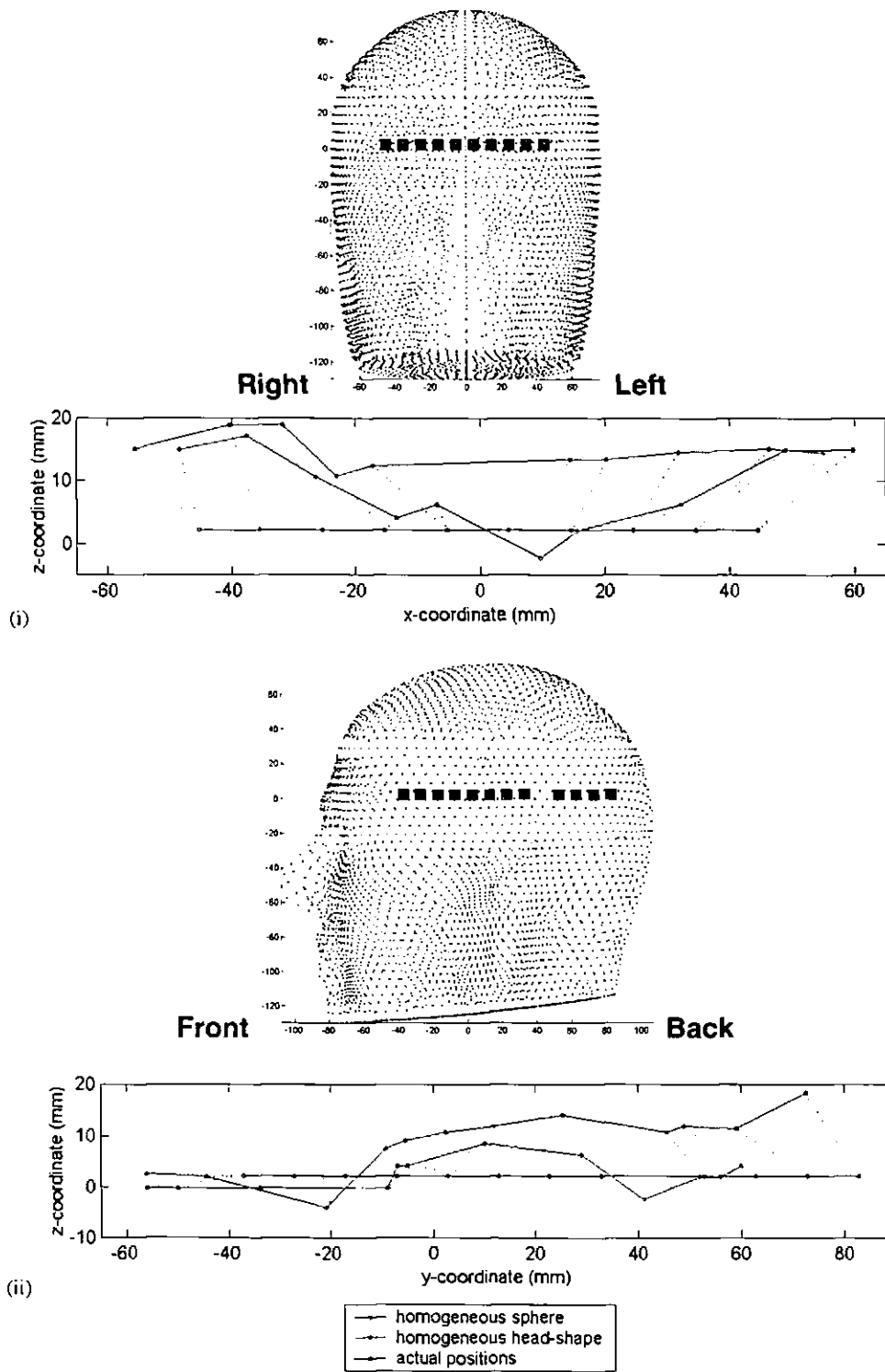
Figure 4-8: (i) 10 target positions (black) from left to right and (ii) 12 from the anterior to the posterior of the head and the corresponding positions of peaks in images reconstructed using $A_{headtank}^{ANAhomsphere}$ (blue) $A_{headtank}^{FEMhomhead}$ (red).

4.3.1.3   Resolution

As in the reconstructions described in the previous chapter, resolution was similar in both the x- and y-directions and was significantly worse than both, in the z-direction. In the XY-plane, the mean FWHM was 27.5±3.6mm and 44.1±7.2mm, respectively for spherical and head-shaped reconstruction and, in the z-direction, it was 35.3±9.2mm and 84.3±36.0mm.

4.3.1.4   Significance of Results

Listed in Table 4-3 are mean values of localization error and the FWHM in the XY-plane and the z-direction for images of Perspex moving in the homogeneous head phantom, reconstructed using $A_{headtank}^{ANAhamsphere}$ and $A_{headtank}^{FEMhomhead}$. Images for the former were analysed on a mesh warped according to the scheme in section 4.2.3.2.

For perturbations in the homogeneous, head-shaped tank, there were no significant improvements gained by incorporation of realistic geometry. For left-to-right movement, mean localization error was 15.0±3.9mm and 16.8±2.1mm respectively for head-shaped and warped-spherical reconstruction. For anterior-to-posterior movement it was 14.9±5.8mm and 14.6±4.1mm. The mean localization error for all measured positions was 14.9±5.0mm and 15.6±3.7mm. When the spherical image was not warped, $A_{headtank}^{FEMhomhead}$ did provide greater localization accuracy for perturbations moving left-to-right ($p = 2.6 \times 10^{-3}$ - two-tailed, paired T-test), but the overall mean localization error, for all positions, 15.6±5.6mm, was no better.

Use of FEM for reconstruction greatly decreased the resolution of images. The mean FWHM in the XY-plane was about 17mm less over 10 positions of Perspex from left to right ($p = 1.6 \times 10^{-5}$), and the FWHM less in the z-direction by about 50mm ($p = 3.5 \times 10^{-4}$).

	MEAN LOCALIZATION ERROR (MM)	MEAN XY-FWHM (MM)	MEAN Z- FWHM (MM)
Homogeneous Sphere (warped)	15.6±3.7	27.5±3.6	35.3±9.2
Homogeneous Head-Shape	14.9±5.0	44.1±7.2	84.3±36.0

Table 4-3: Analysis results for reconstructions of data from the homogeneous head-shaped tank.

4.3.2 Reconstruction of Data from the Skull Tank

4.3.2.1 Images

Images are shown in Figure 4-9 of the Perspex insulator placed inside the skull cavity at positions y = 43mm, z = 2 and x = [-45, -25, -5, 5, 25, 45] relative to orienting electrodes 17 and 13. They were reconstructed using $A_{headtank}^{ANAhomsphere}$, $A_{headtank}^{ANA3shellsphere}$, $A_{headtank}^{FEMhomhead}$ and $A_{headtank}^{FEMskullhead}$. Again, four slices were extracted, 15mm apart, with the lowest on the plane containing the orienting electrodes. Each image was normalized to the peak of the impedance change in that image. For spherical reconstructions, those in the centre had magnitudes 0.8 and 0.9 times those at the edge for homogeneous and layered models respectively. For head-shaped reconstructions, their magnitudes were 1.6 and 1.2 times those at the edge! Scales were symmetric about zero for each image. The images reconstructed using $A_{headtank}^{ANAhomsphere}$ and $A_{headtank}^{ANA3shellsphere}$ were again shown projected onto a warped version of the homogeneous spherical mesh.

4.3.2.2 Spatial Accuracy

Results are plotted for reconstructions of the Perspex as it moved in the left-to-right and anterior-to-posterior directions. In Figure 4-10(i) and (ii), are shown the loci of peaks in images reconstructed using all four matrices. The loci, r_{image}, were projected onto the XZ-plane and the YZ-plane, a dotted line connecting each data point with the corresponding locus of the target perturbation. These loci, r_{target}, are shown in black. For spherical reconstruction, results are shown for the peak position in the warped image.

4.3.2.3 Resolution

Resolution was studied for 5 positions of Perspex from the middle to the left-hand side. It was similar in each of the x- and y-directions for each reconstruction method and was significantly worse in the z-direction by all methods. In the XY-plane, the mean FWHM was significantly better for reconstruction with $A_{headtank}^{ANAhomsphere}$ than with $A_{headtank}^{ANA3shellsphere}$ (p=0.00028) and with $A_{headtank}^{FEMhomhead}$ (p=0.0056) but not $A_{headtank}^{FEMskullhead}$ (Figure 4-9). Values are summarized in Table 4-4. The analytical 3-shell sphere model gave

Analytical Spheres   *FEM Head-Geometry*

HOMOGENEOUS

3-LAYERS
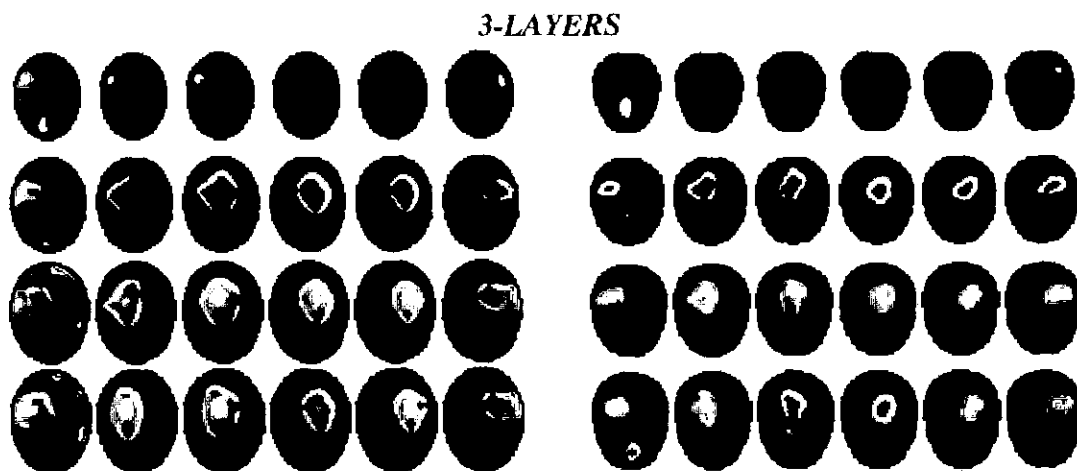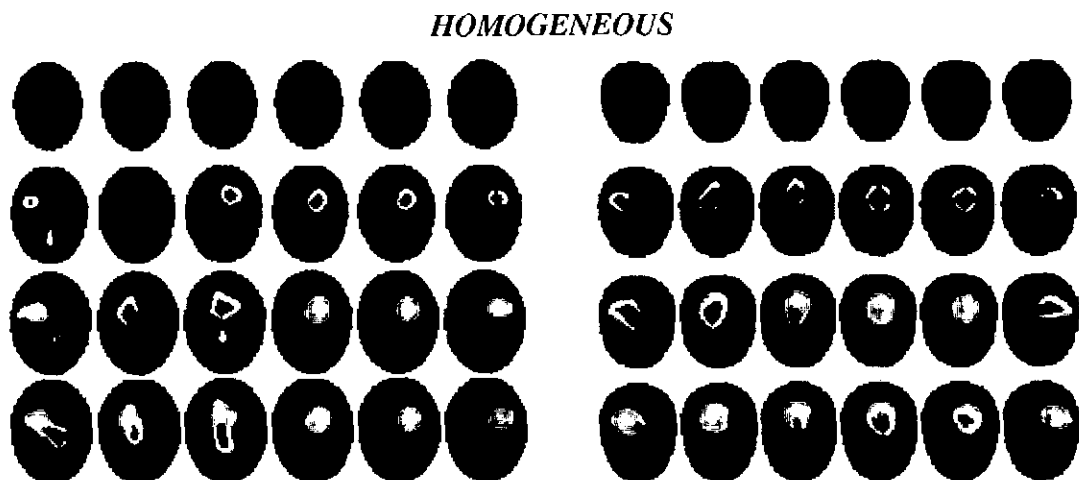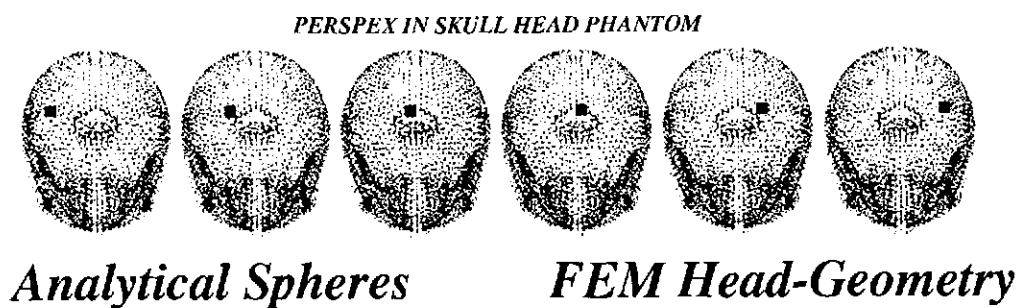
Figure 4-9: Normalized images of Perspex moving right to left in the skull-tank: x = [-45, -25, -5, 5, 25, 45] reconstructed using homogeneous matrices $A_{headtank}^{ANAhomsphere}$ and $A_{headtank}^{FEMhomhead}$ and layered matrices $A_{headtank}^{ANA3shell}$ and $A_{headtank}^{FEMskullhead}$. In each set, rows of images are horizontal slices through the model, separated vertically by 15mm, with the lowest through the orienting electrodes 13 and 17.

159

worse XY-resolution than the FEM homogeneous head (p=0.007). Z-resolution was best using the homogeneous sphere model but it was better using the 3-shell sphere model than the homogeneous head-shaped model (p=0.019). The resolution of both sets of FEM reconstructions was similar.

4.3.2.4   Significance of Results

Listed in Table 4-4 are the mean values of localization error and FWHM in the XY-plane and the z-direction for images of Perspex moving in the skull tank, reconstructed using $A_{headtank}^{ANAhomsphere}$, $A_{headtank}^{ANA3shellsphere}$, $A_{headtank}^{FEMhomhead}$ and $A_{headtank}^{FEMskullhead}$. Images for spherical reconstructions were analysed after projection onto the warped spherical mesh.

For reconstruction assuming realistic geometry, mean localization error was 20.8±5.9mm and 16.4±7.7mm respectively for the skull matrix and the homogeneous matrix. For spherical reconstruction, it was 14.3±4.7mm and 15.7±6.7mm with and without inclusion of layers (Without warping, the mean error was slighter higher in both cases but not significantly). The mean localization error was less by 6.5mm using the analytical 3-shell sphere model than using the FEM skull-head model, which included realistic geometry and conductivity. After performing six T-tests between results from all reconstruction methods, these were the only significantly different sets of localization errors (p = 0.035). Therefore, no algorithm provided significantly better or worse localization accuracy than did all the others for the skull tank.

XY-resolution was significantly better using $A_{headtank}^{ANAhomsphere}$ than $A_{headtank}^{ANA3shellsphere}$ and $A_{headtank}^{FEMhomhead}$ ($p_{3shellsphere}$ = 3.6x10^{-3}; $p_{homhead}$ = 2.8x10^{-3}) and both FEM reconstructions gave better XY-resolution than use of $A_{headtank}^{ANA3shellsphere}$ ($p_{homhead}$ = 0.030; $p_{skullhead}$ = 0.010).
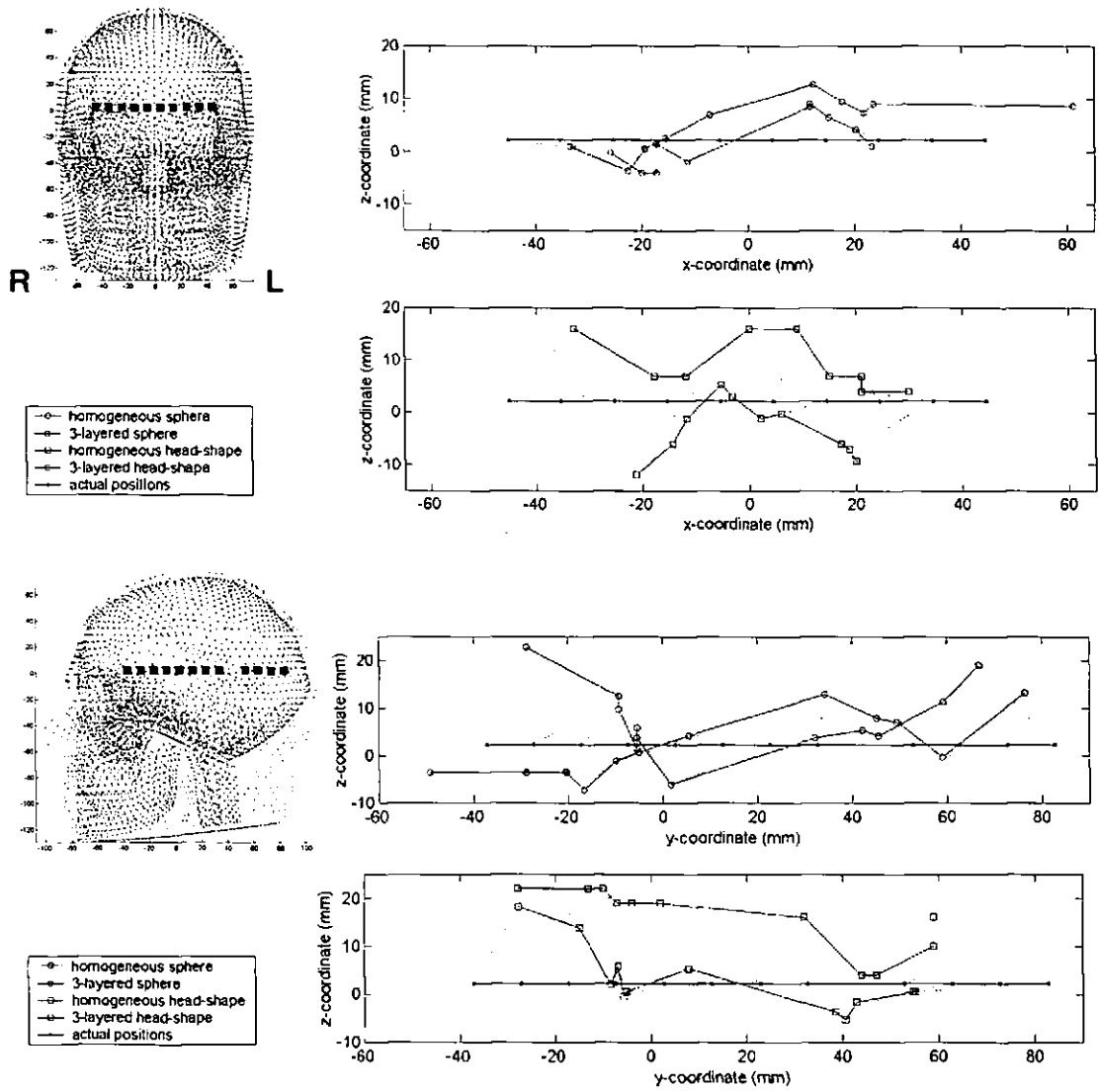
Figure 4-10: (i) 10 target positions (black) from left to right and (ii) 12 from the anterior to the posterior of the head in the skull tank and the corresponding positions of peaks in images reconstructed using homogeneous matrices $A_{headtank}^{ANAhomsphere}$ and $A_{headtank}^{FEMhomhead}$ (blue) and 3-layer matrices $A_{headtank}^{ANA3shell}$ and $A_{headtank}^{FEMskullhead}$ (red).

	Mean localization error (mm)	Mean XY-FWHM (mm)	Mean Z- FWHM (mm)
Homogeneous Sphere (warped)	15.7±6.7	34.2±2.7	52.2±2.7
3-Shell Sphere (warped)	14.3±4.7	55.2±5.5	65.4±2.5
Homogeneous Head-Shape	16.4±7.7	43.8±4.6	81.0±9.5
3-Shell Head-Shape	20.8±5.9	44.2±9.1	79.8±21.2

Table 4-4: Analysis results for reconstructions of data from the homogeneous head-shaped skull tank.

4.3.3 Reconstruction of Human Data

Although significant impedance changes occurred in the 4-terminal measurements (Gibson 2000; Tidswell, Gibson et al. 2001b) during visual stimulation, only images from five subjects, out of the seven considered, gave pixel values during stimulus that were significantly larger than the noise in the pixel values during baseline. At least one algorithm located a posterior impedance decrease, whether primary or secondary, in all five subjects and an accompanying posterior increase in three.

Examples are shown in Figure 4-11 of the time course and peak locations of impedance changes imaged during visual evoked response experiments on two subjects. A slice is shown, 15mm above the orienting electrodes, for reconstruction using the homogeneous matrices $A_{headtank}^{ANAhomsphere}$ and $A_{headtank}^{FEMhomhead}$ and the 4-layer matrices $A_{human}^{ANA4shellsphere}$ and $A_{human}^{FEMfullhead}$. The two subjects were chosen to give examples of a primary increase and a primary decrease of similar magnitude. In each, the change occurred deep in the brain. However, in each subject, these were accompanied by significant changes elsewhere of equal and opposite polarity and with similar or greater magnitude depending on which model was assumed for reconstruction. A *primary change* is defined, nominally, as that which had the highest magnitude in most, if not all, reconstructions. A *secondary change* is defined as that which was significant but had a lesser magnitude in most, if not all, reconstructions. Resolution can be observed, qualitatively in each set of images.

The magnitudes of the changes were similar across subjects for each algorithm but within subjects between algorithms due to such factors as element sizes in the different meshes used. Without investigating further the precise relationship between image impedance change and actual impedance change I simply showed the images in Figure 4-11 with a symmetric colour scale normalized to the peak of the primary impedance change

In the first set of images, the magnitude of the primary, mid-brain resistivity increase was significantly higher than that of the posterior decrease for reconstruction assuming spherical models. Their magnitude was similar when realistic geometry was assumed. In the case of homogeneous-head reconstruction, the decrease was greater in magnitude than the increase.

In the second set of images, the primary mid-brain resistivity decrease was not detectable assuming four concentric spheres but was the most significant change assuming all other models. A significant decrease was also seen in all, on the right of the brain, and with similar magnitude. A decrease on the left was only seen assuming spherical models though these were of similar magnitude to the primary decreases. A significant increase was seen in the posterior of the brain assuming all models. The frontal increase was only observed when homogeneous models were assumed though its magnitude was similar to that of other changes.

SUBJECT 1

stimulus

time (seconds)

R   L

transverse   sagittal
significant increase

transverse   sagittal
significant decrease

SUBJECT 2

stimulus

resistivity increase
- homogeneous sphere
- homogeneous head
- 4-shell sphere
- full-head

resistivity decrease
- homogeneous sphere
- homogeneous head
- 4-shell sphere
- full-head

transverse   sagittal
significant decrease

transverse   sagittal
significant increase

Figure 4-11: The time-course and loci of impedance changes, during visual evoked response experiments on two subjects (data averaged from 6 experiments in each), reconstructed using all algorithms. The time-course is shown on a single slice only, 15mm above the orienting electrodes. For each subject, the first set of transverse and sagittal plots describe the loci of the primary impedance changes and the second, the secondary changes.

164

4.4   Discussion

Reconstruction algorithms were presented, based on the finite element method, which incorporated realistic geometry and conductivities in the forward model. Also presented were algorithms based on the analytical method, one of which incorporated the effect of layers. All algorithms assumed point electrodes attached to the mesh surface at a point closest to the electrode positions measured accurately on the head-shaped tank.

4.4.1   Spherical & Homogeneous ⇒ Head-shaped & Homogeneous

It was seen that, for reconstructing images of a Perspex perturbation in a homogeneous, head-shaped tank, no benefits were obtained by accurately modelling the realistic geometry of the head. Since resolution was hampered by use of the FEM, the analytical, spherical algorithm performed better, when spherical images were projected onto a spherical mesh warped according to the measured electrode positions. The FEM model accounts for a much larger volume than does the spherical model, as can be seen in Figure 4-5. Much of the volume is also at considerable distance from the electrodes causing there to be a region of low sensitivity even more extensive than for the sphere. As a result, the largest post-weighting coefficients (section 2.2.2.1) were 5 orders of magnitude higher than the smallest, whereas values for the sphere covered 3 orders of magnitude. This latter factor is likely to degrade the image by weighting it towards those regions, as described in section 3.4, and is responsible for some of the very high values of FWHM in the z-direction, which had adverse effect on the mean.

The realistic mesh also had about half as many nodes (Table 4-1). This fact alone would suggest that the mesh was less dense. However, the ratio between largest and smallest elements was 30 times greater than for the homogeneous sphere mesh so, whilst there were regions meshed to a similar density, there were also regions meshed much less densely. It was found that the node corresponding to the largest value of support s, and therefore representing the largest discrete volume, existed in the centre of the head volume. This is obvious from inspection of Figure 4-4 and is shown diagrammatically in Figure 4-12. Those in the homogeneous mesh existed in the centres of each octant of the mesh (for discussion of partitioning, see 2.2.1.2). If these discrete volumes were approximated to be spherical (which is reasonable – see Figure 2-2(ii)), those for the sphere would have diameters 20mm and that for the head-shape 34mm. It may be that mesh density was the limiting factor to resolution in the case of each reconstruction method since the ratio of these volumes is 0.59 and that of the mean FWHM was 0.625 in the XY-planes of the two sets of images. It is not wise to

conclude on the relative resolution of the two methods in this plane until calculations are performed again with a FEM sensitivity matrix generated on a mesh that is finer in the region of interest.

4.4.2 Spherical & Homogeneous ⇒ Head-shaped & Layered

4.4.2.1 Skull-Tank

The mean localization error was lowest for reconstruction of skull-tank data when a 3-shell spherical model was assumed and solved analytically but it was not significantly lower than for assumption of the homogeneous sphere or the homogeneous head-shaped models. The highest mean localization error was found when the 3-layered, realistically shaped model was assumed for reconstruction but it was only significantly higher than errors when the 3-shell sphere model was assumed.

The homogeneous models returned very similar impedance change loci for both left-to-right and anterior-to-posterior movement, as can be seen in Figure 4-10. As in the previous chapter, the analytical shell model appeared to localize the changes less centrally than the homogeneous sphere model, again seen in Figure 4-10. It also appeared to localize them less centrally than did either realistically shaped model. In particular, the analytical, spherical shell model reconstructed frontal perturbations more frontally and more accurately than did all other models. Over most of its surface, the skull was represented by only one layer of nodes and this result suggested that the linear FEM, once again, did not take into account the effect of thin layers as well as did the analytical method. In all reconstructions, the layered FEM model localized peaks higher up in the head than did the homogeneous FEM. Plotted in Figure 4-12 are the positions of the node with maximum support in each FEM mesh. This occurs lower down in the homogeneous model and may have acted to draw impedance changes towards it. The variation of support may also explain the fact that the magnitude of central changes was larger than for superficial changes in FEM reconstructions (section 4.3.2.1). Whilst smoothing, by multiplication of support was intended to reduce the artefacts in reconstructed images due to inhomogeneities in the mesh, these results would suggest that it is important to produce solutions on meshes with little variation of density throughout the regions of interest. They also suggests that it is difficult to determine whether the bias of the full-head model towards the centre, in comparison to the analytical shell model, is due to the effect of layers in the latter or to the effect of mesh density in the former.

Resolution was better in the XY-plane using the homogeneous sphere model than the spherical shell model and the homogeneous head-shaped model. This was as expected from

the results of Chapter 3 and from arguments in section 4.4.1 respectively. Resolution was not significantly worse using the layered head model. This was because, although the mean FWHM was 10mm more, the spread of FWHM values was 9.1mm, almost twice as high as that for the homogeneous head-shaped reconstructions. It can be seen in Figure 4-4 that the variation of support is much greater throughout the region of interest in the full-layered model, which could be responsible for the variation in resolution. Higher resolution can be seen for these reconstructions in Figure 4-9, near the inner surface of the skull, and lower resolution towards the centre of the skull cavity. Z-resolution was best, again, using the homogeneous sphere model and was better using the shelled sphere model than the homogeneous head-shaped model. As described in the previous section, gain, the effect of post-weighting on the latter was to draw the distribution of a peak impedance change towards the low sensitivity regions around the neck and chin, giving very large values for FWHM in the z-direction for some positions of the inhomogeneity.
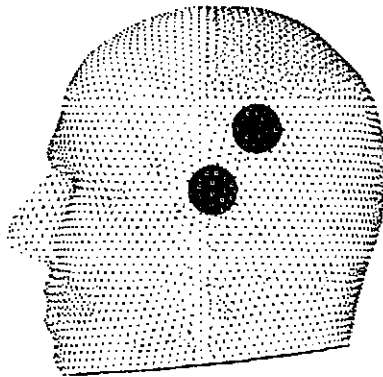
Figure 4-12: The positions of the node with maximum support s in the homogeneous (red) and the layered (green) head-shaped mesh

4.4.2.2   Human Data

By each method, in its present state, reconstruction of human data gave images that were recognizable as the same evoked response and primary or secondary impedance changes were found at the posterior of the brain in all five subjects whose images showed changes greater than baseline noise. However, there was no consistency in the location or polarity of primary impedance changes between functional images of the subjects during VER experiments. For one subject, peaks could not be localized at all using the 4-shell sphere algorithm. In general, for any particular subject, reconstructions using each algorithm returned peak changes of the same polarity and in the same hemisphere to within about 40mm. There was more consistency between peak loci in spherical reconstructions and between those in head-shaped reconstructions than there was between either of these two sets of reconstructions. There was

167

no noticeable bias of any method towards regions of low mesh density but further conclusion was confounded by inter-subject variability. It is difficult to know whether the localization errors were the result of the approximations made in the forward models or whether they were due to the physiological mechanisms underlying the conductivity changes in the brain during functional activity, since a PET or an MRI study on each of the patients may well have yielded similarly variable results (section 4.1.3).

Over all 5 subjects, the homogeneous sphere algorithm appeared, consistently, to give the best resolution, sometimes separating peaks when they were absorbed into one, larger peak in the other algorithms. For less central changes, the full-head algorithm appeared to give slightly better resolution than the homogeneous-head algorithm, consistent with the arguments above concerning support. The shelled sphere algorithm, in general, gave the poorest resolution.

4.5   Conclusion

It was thought that the introduction of correct geometry would improve image reconstruction in head-tank studies, as compared to reconstruction assuming spherical geometry. In their present state, however, reconstruction by both methods was similar in homogeneous tank studies and no benefit was gained by incorporating realistic geometry into the forward model. In skull-tank studies, there was an advantage reconstructing frontal changes using the analytical, shelled-sphere model though, overall, it was no better than the homogeneous sphere or homogeneous head-shaped model and resolution was best with the homogeneous sphere model. The layered head model gave the highest mean localization error and results suggested that the inclusion of geometry and layers would not benefit reconstruction of EIT images when the object under study is layered and non-spherical.

Since the density of the realistically shaped meshes was about one-fifth that of the spherical meshes in the regions of interest, it is not strictly fair to compare localization accuracy and resolution in reconstructions assuming these different models. Conclusion cannot therefore be made, from these studies, on the effect of geometry, in the presence of layers, in images that might be obtained if higher density meshes were to be used. However, the studies carried out in this chapter revealed the significant influence of mesh density and heterogeneity on localization and resolution in image reconstruction. The effects were large enough to mask any improvements that might have been gained by inclusion of accurate geometry and conductivity distributions. It will not be difficult to produce new meshes with a finer and more homogeneous distribution of nodes throughout the brain. It will be possible to make more confident assertions on the benefits of the realistic FEM model when these are used to reconstruct the same head-tank data using the algorithm described above.

In the EIT problem, it would appear, from the above, that the introduction of a more complicated geometry cancels, to some extend, the benefits of using of an analytical sphere model to account for the presence of layers. The homogeneous model, has high resolution, and the use of the 3-shell sphere model, for the skull-tank, improves localization accuracy in the front of the head (and gives slight improvement overall). But in every other respect, all models perform similarly whether they include layers and/or realistic geometry, so no one model in particular, as it stands, would be recommended for use in a clinical setting. However, the differences in information given by reconstruction of human images suggest that one model may give insight into the images given by another and it would be of benefit to use all four, in their present state, in order to improve interpretation of results.

Imaging Neuronal Depolarization

5 Imaging Neuronal Depolarization

5.1 Introduction

Electroencephalography, EEG, has excellent temporal resolution but a poor spatial resolution, especially for changes deep within the brain. PET and fMRI have good spatial resolution, of several millimetres, but a time resolution that is only sufficient to measure the metabolic changes associated with neuronal activity, occurring over a few seconds (section 1.2.2.2). It would be of great use could an imaging technique combine the level of spatial resolution they demonstrate with the temporal resolution of electrophysiological methods in order to map neuronal activity itself, rather than its consequences. EIT could offer this possibility.

5.1.1 Physiological Background

Much work has been done over the century to model the electrical properties of the tubular structures (*cell processes - axons* and *dendrites* – see Figure 5-1) which extend from the main cell body (*soma*) of each neuron and of bulk grey matter (Cole and Hodgkin 1939; Hodgkin and Rushton 1946; Hodgkin 1947; Ranck 1963; Rall 1975; Okada, Huang et al. 1994; Rall 1999). All of their models required the application of cable theory and presented results with which the medical world today is reasonably well satisfied.

The bulk resistivity of cortex has been reported as having values ranging from 208Ωcm to 321Ωcm at various frequencies between 3000Hz and 5Hz (Freygang and Landau 1955; VanHarreveld and Ochs 1956; Ranck 1963; VanHarreveld, Murphy et al. 1963; Ranck 1966). Several measurements have been made of localized cortical resistance changes during activity, ranging from 0.005%, at 10kHz using depth electrodes (Klivington and Galambos 1968), to –0.03%, at DC using electrodes placed on the cortical surface (Boone 1995). These were summarized in section 1.4.2.3. A crude estimate was made of the relation between the local change and the change in a 4-terminal measurement on the scalp (Boone 1995). A ratio of 10:1 was suggested since cortical resistivity changes of Δ5%, related to blood volume changes, caused Δ0.5% mean, negative voltage changes on the scalp in previous EIT measurements (Gibson, 2000). However, the maximum changes had magnitudes between 1% and 2%, so a ratio 5:1 could be assumed to estimate the maximum scalp signals due to neuronal impedance changes.
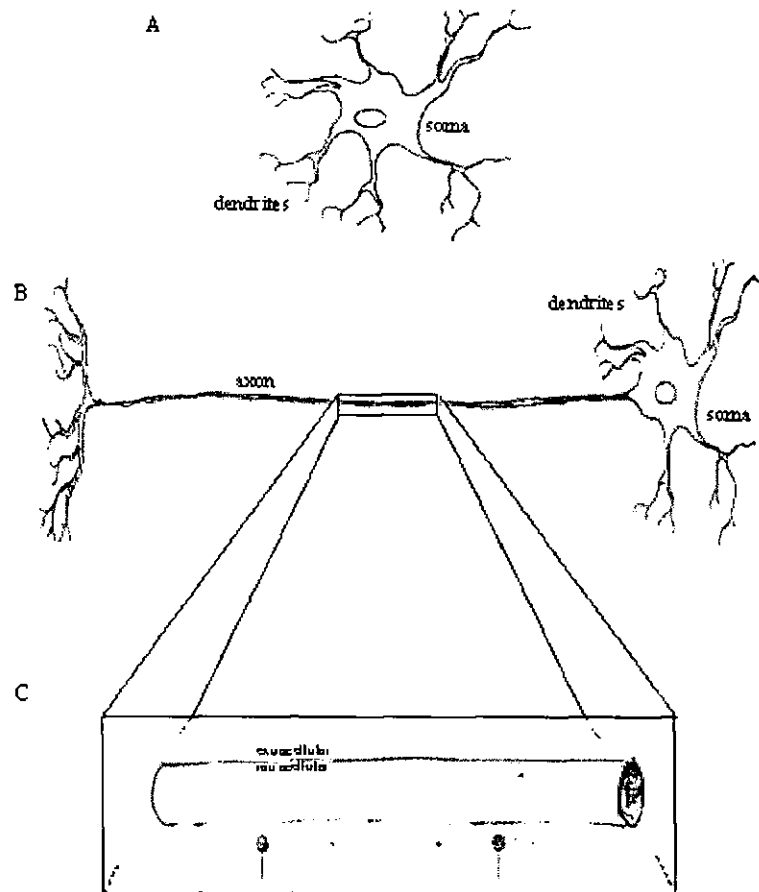
Figure 5-1: A - A glial cell with dendritic processes extending from the cell body or soma B - A neuron (motoneuron) with dendritic and axonal processes extending from the cell body or soma. C - A section of the motoneuron axon. An intracellular electrode provides current, which flows parallel to the axis of the process and 'leaks' out into the extracellular space with increasing distance from the source.

5.1.2 Purpose

The purpose of this work was to estimate the change that might be observed in a four-terminal scalp impedance measurement during neuronal depolarization. From this result, it was intended to assess the possibility that EIT might combine the temporal resolution of EEG and a spatial resolution more similar to fMRI and PET in order to image neuronal depolarization directly.

5.1.3 Design

The current flow through neuronal tissue is governed by *cable theory*. This was originally applied to the problem of transatlantic telegraph cables. Applied to neuronal conduction, the theory suggests electrical circuits equivalent to cell membranes and processes and it reduces the problem from three dimensions to one. The cell membrane is equivalent to a resistor and capacitor in parallel and this forms part of a ladder-like circuit, which is equivalent to the extended, cylindrical cell process.

Although it was my wish to predict the resistive behaviour of the cortex during activity, I first applied cable theory to that of a peripheral crab nerve. The geometry of the problem is quite simple for the case of the peripheral nerve. Reasonable assumptions could be made in the development of a mathematical model and experimental verification was relatively straightforward. All but one of the assumptions were identical to those in the model developed by Boone (Boone 1995). However, a more appropriate boundary condition was used in the model reported here.

The geometry of cortical neurons is more complex than that of the peripheral axon and experimental verification of predictions is difficult. However, several of the assumptions made in the *peripheral model* were also appropriate when modelling cortical neurons. Additional assumptions were made to produce an appropriate *cortical model* describing the resistive behaviour first of individual neurons and then of bulk cortical tissue during depolarization. A further complication is that the parameters required by the models are not well known. There are, however, ranges published and these were used to estimate margin of error in the results.

This chapter describes a model developed to estimate the size of the local impedance change associated with the depolarization of a population of neurons. The peripheral model is presented first, with its experimental validation. The cortical model is then presented. It is similar to that developed by Boone (Boone 1995) but with several changes, which will be highlighted as they occur. Further to this, using 3D models of the head, described previously in this thesis, this microscopic cortical model was extended to predict the signal that might be measured on a single channel of an EIT system. The change was expected to be much smaller than those described and imaged in the previous chapter.

5.2 Methods

5.2.1 The Peripheral Model

The nervous system is divided into two sub-systems, the central, which extends inside the spinal column and includes the brain, and the peripheral, which innervates the rest of the body. Cable theory applies to conduction in both but the simplest case of core conduction in the nervous system is that in the unmyelinated peripheral nerve axon, whose form resembles that in Figure 5-I(b) and whose geometry is described by Figure 5-2.
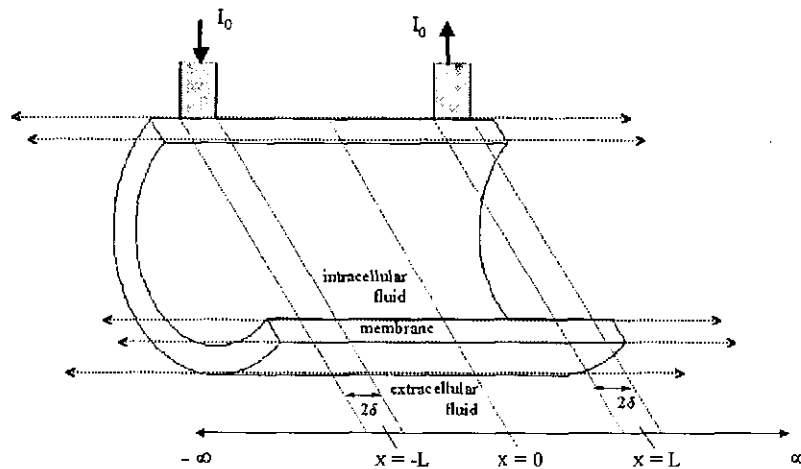
Figure 5-2. A cut-away diagram showing the geometry of the nerve fibre model. See text for explanation of symbols

5.2.1.1 Assumptions and Approximations

In the following, the assumptions used for the peripheral model are labelled with a P and those for the cortical model, later, with a C.

[P1] The nerve axon was assumed to be a uniform cylinder consisting of purely resistive *intracellular fluid* surrounded by a capacitive and resistive *membrane* bathed in a resistive *extracellular fluid* which occupied a fraction α of the overall tissue volume (Figure 5-2).

[P2] r_m, c_m and r_i were assumed to be constant on each branching cable and the cell passive and linear with respect to the testing current. This assumption was justified by Hodgkin and Rushton (Hodgkin 1947) and is necessary for application of classical linear cable theory.

[P3] Measuring electrodes were placed some distance $2L$ apart along the length of the nerve, and the axon assumed to be sufficiently thin that the electric field in the intra- and extracellular space was parallel to the fibre.

174

[P4] The extrapolar length of the axon was sufficient to be assumed infinite so the axon was assumed to be 'open-ended'. Boone assumed the axon to be 'closed ended' (see assumption [C8])

[P5] The nerve was assumed to exist in two steady resistance states, *resting* and *depolarising*. In the former state, the longitudinal resistivity was calculated using the expression derived below and all the relevant parameters. In the latter state, this was repeated with membrane resistivity multiplied by a factor $(1/D_p)$.

5.2.1.2 Notation

Variables:

x distance (m) along axon

i_e extracellular current (A)

i_i intracellular current (A)

I total current flowing through the axon and extracellular fluid ($I = i_e + i_i$)

i_m current (A cm^{-1}) passing into axon through the membrane

V_e potential (V) of extracellular fluid with respect to a distant point: $V_e = -\int_{-\infty}^{x} r_e i_e dx$

V_I potential (V) of intracellular fluid with respect to a distant point: $V_i = -\int_{-\infty}^{x} r_i i_i dx$

V_m the potential difference (V) across the surface of the membrane   ($V_m = V_e - V_i$)

Constants:

a radius (cm) of axon

α proportion of tissue considered to be extracellular

$2L$ the separation (cm) of the electrodes

2δ the width (cm) of the electrodes – to be made vanishingly small

ρ_m resistance x unit area of the surface membrane (Ω cm^2)

C_m the capacity per unit area (F cm^{-1}) of the surface membrane in the axon

D the factor by which membrane resistivity decreases during depolarization

ρ_i specific resistivity of the intracellular fluid (Ω cm)

ρ_e specific resistivity of the extracellular fluid (Ω cm)

r_e resistance per unit length (Ω cm^{-1}) of extracellular fluid ($\rho_e(1-\alpha)/\alpha\pi a^2$)

r_i resistance per unit length (Ω cm^{-1}) of intracellular fluid ($\rho_i/\pi a^2$)

r_m resistance x unit area (Ω cm) of the surface membrane in the axon ($\rho_m/2\pi a$)

c_m the capacity per unit length (F cm^{-1}) of the surface membrane in the axon ($C_m \times 2\pi a$)

λ length constant = $\sqrt{[r_m / (r_i + r_e)]}$

τ_m time constant = $r_m c = \rho_m C_m$

5.2.1.3   Theory

Following the definitions, it is possible to write down two equations demonstrating Ohm's Law

$$\frac{\partial V_e}{\partial x} = -r_e i_e \qquad \text{[5-1]}$$

$$\frac{\partial V_i}{\partial x} = -r_i i_i \qquad \text{[5-2]}$$

and

$$\frac{\partial V_m}{\partial x} = (r_e + r_i)i_i - Ir_e \qquad \text{[5-3]}$$

Rearranging [5-3] and, since V_m and $V_e = 0$ at $x = 0$, for the intrapolar region, integrating with respect to x

$$V_m = \left(\frac{r_e + r_i}{r_e}\right)V_e + r_i \int_0^x Idx \qquad \text{[5-4]}$$

Membrane current can be expressed in terms of current conservation and as a sum of capacitive and resistive currents

$$i_m = \frac{\partial i_i}{\partial x} \qquad \text{[5-5]}$$

$$i_m = c\frac{\partial V_m}{\partial t} + \frac{V_m}{r_m} \qquad \text{[5-6]}$$

Hence

$$\frac{V_m}{r_m} + c\frac{\partial V_m}{\partial t} = \frac{\partial i_i}{\partial x} \qquad \text{[5-7]}$$

Substitution for i_i from [5-3] gives

$$\frac{V_m}{r_m} + c\frac{\partial V_m}{\partial t} = \frac{1}{r_e + r_i}\frac{\partial^2 V_m}{\partial x^2} + \frac{r_e}{r_e + r_i}\frac{\partial I}{\partial x} \qquad \text{[5-8]}$$

The last term vanishes everywhere except under the electrodes since $I=0$ and I_0 in the extrapolar and intrapolar regions. Hence for regions x = $-\infty \rightarrow (-L-\delta)$, $(-L+\delta) \rightarrow (L-\delta)$ and $(L+\delta) \rightarrow \infty$ we obtain the *cable equation*

$$-\lambda^2 \frac{\partial^2 V_m}{\partial x^2} + \tau_m \frac{\partial V_m}{\partial t} + V_m = 0 \qquad \text{[5-9]}$$

where λ and τ are as defined above. Since we are studying the steady state, the second term is zero and, defining a new variable $X = x / \lambda$

$$\frac{\partial^2 V_m}{\partial X^2} = V_m \qquad [5\text{-}10]$$

Certain boundary conditions must be imposed in order to solve equation [5-10]. One is that membrane voltage $V_m \to 0$ as $x \to -\infty$. This gives us two solutions for V_m

for $\dfrac{\delta - L}{\lambda} < X < \dfrac{L - \delta}{\lambda}$ $\qquad V_m = Ae^X + Be^{-X} \qquad\qquad [5\text{-}11]$

for $-\infty < X < \dfrac{-\delta - L}{\lambda}$ $\qquad V_m = Ce^{(X + \frac{\delta + L}{\lambda})} \qquad\qquad [5\text{-}12]$

Another boundary condition for the intrapolar region is that the voltage distribution is anti-symmetric. Hence $V_m(X) = - V_m(-X)$ and $A = -B$ so that

for $\dfrac{\delta - L}{\lambda} < X < \dfrac{L - \delta}{\lambda}$ $\qquad V_m = Ae^X (1 - e^{-2X}) \qquad\qquad [5\text{-}13]$

There are also two continuity conditions that must be observed. Both V_m and i_i are continuous functions of x. Since this is the case, as δ becomes vanishingly small, we can equate [5-12] and [5-13] either side of the electrode i.e. $V_m(-L-\delta) = V_m(-L+\delta)$ so that

$$C = Ae^{\frac{\delta - L}{\lambda}} (1 - e^{-2\frac{\delta - L}{\lambda}})$$

and therefore,

for $-\infty < X < \dfrac{-\delta - L}{\lambda}$ $\qquad V_m = Ae^{(X + \frac{2\delta}{\lambda})}(1 - e^{-2\frac{\delta - L}{\lambda}}) \qquad\qquad [5\text{-}14]$

The constant A can be found by evaluating [5-3] at either side of the electrode at $X = -L$

$$\left(\frac{\partial V_m}{\partial x}\right)_{x = \delta - L} - \left(\frac{\partial V_m}{\partial x}\right)_{x = -\delta - L} = (r_e + r_i)\{(i_i)_{x = \delta - L} - (i_i)_{-\delta - L}\} - r_e(I_{x = \delta - L} - I_{-\delta - L}) \qquad [5\text{-}15]$$

But $\{(i_i)_{x = \delta - L} - (i_i)_{-\delta - L}\} = 0$ from continuity of i_i, $I_{x = -\delta - L} = 0$ and $I_{x = \delta - L} = I_0$

so that

$$\left(\frac{\partial V_m}{\partial X}\right)_{X = \frac{\delta - L}{\lambda}} - \left(\frac{\partial V_m}{\partial X}\right)_{X = \frac{-\delta - L}{\lambda}} = -r_e I_0 \lambda \qquad [5\text{-}16]$$

A is found by substituting [5-13] and [5-14] into [5-16] so that

for $\dfrac{\delta - L}{\lambda} < X < \dfrac{L - \delta}{\lambda}$ $\qquad V_m = -\dfrac{r_e I_0 \lambda}{2} e^{\frac{(x + \delta - L)}{\lambda}} (1 - e^{\frac{2x}{\lambda}}) \qquad [5\text{-}17]$

177

In order to calculate the potential difference between the two electrodes, something must be known about V_e at these points. Evaluating [5-17] at the inner extreme of the electrodes, in order to substitute into [5-4],

$$V_m(L - \delta) = \left(\frac{r_e + r_i}{r_e}\right) V_e(L - \delta) + r_i \int_0^{L-\delta} I dx \qquad [5\text{-}18]$$

and

$$V_m(\delta - L) = \left(\frac{r_e + r_i}{r_e}\right) V_e(\delta - L) + r_i \int_0^{\delta - L} I dx \qquad [5\text{-}19]$$

As $\delta \to 0$, the integrals tend to Lr_iI_0 and $-Lr_iI_0$ and therefore the applied voltage is

$$V_0 = V_e(-L) - V_e(L) = \left(\frac{r_e}{r_i + r_e}\right)\left(V_m(-L) - V_m(L)\right) + \frac{2Lr_ir_e}{r_i + r_e} I_0 \qquad [5\text{-}20]$$

Substituting for V_m from [5-17], under conditions of $\delta \to 0$,

$$V_0 = \frac{r_e^2 I_0 \lambda}{r_i + r_e}(1 - e^{-\frac{2L}{\lambda}}) + \frac{2Lr_ir_e}{r_i + r_e} I_0 \qquad [5\text{-}21]$$

This is the voltage generated between two electrodes placed on a peripheral nervous tissue of total cross-sectional area $\pi a^2/(1-\alpha)$ separated by a distance 2L. Expressed in terms of specific resistivities and hyperbolic trigonometric functions, the resistivity of the peripheral nervous tissue, found by dividing [5-21] by $[2LI_0(1-\alpha)]/\pi a^2$, is therefore

$$P_0^P = \frac{\rho_i \rho_e}{[(1-\alpha)\rho_e + \alpha\rho_i]} + \frac{\rho_e^2(1-\alpha)}{\alpha[(1-\alpha)\rho_e + \alpha\rho_i\left(\frac{L}{\lambda}\right)} e^{-\frac{L}{\lambda}} \sinh\left(\frac{L}{\lambda}\right) \qquad [5\text{-}22]$$

5.2.1.4   AC Impedance

Returning to equation [5-9], we can see that, if the injected current is not DC, then, when the steady state has been reached, [5-10] becomes

$$\frac{\partial^2 V_m}{\partial X^2} = V_m\left(1 + j\omega\tau_m\right) \qquad [5\text{-}23]$$

where ω is the frequency of current injection. In all subsequent solutions, λ is simply replaced by $1/F$, where

$$F = \frac{\sqrt{1 + j\omega\tau_m}}{\lambda} \qquad [5\text{-}24]$$

178

Therefore all the expressions for conductivity reported in this chapter are valid at frequencies greater than zero if λ is replaced by $1/F$.

5.2.1.5   Parameters and Evaluation

To evaluate expression [5-22], it was necessary to know the values of the parameters associated with the crustacean peripheral nerve. These are listed in Table 5-1. P_0^P was then calculated for 'resting' membrane resistivity and 'depolarising' membrane resistivity and the percentage difference ΔP_0^P % found.

5.2.1.6   Realistic Considerations

The suggestion of a two-state system assumed that the impedance reached a steady state during the time in which the tissue was depolarized underneath the measuring electrodes. This cannot be the case for low ($\ll 1/\tau$) measuring frequencies. The impedance measurement cannot reach steady state during the depolarization because the capacitive characteristics of the membrane act to resist a change in voltage. In two simulations, constant current I was driven through a resistor R and capacitor C in parallel. One network had a time constant, RC, of 0ms and the other 8ms, representative of a peripheral nerve (Hodgkin, 1947). R represented the resting membrane resistance and C its capacitance. A resistance change ΔR was imposed, taking the shape of a descending half cycle of a sine wave, lasting 1ms, having a minimum at a value $(1/D_p)*R$. During a resistance decrease, the time course was calculated for the voltage generated across the capacitor for each of the time constants. The reduction in amplitude of the maximum voltage change from the first to the second simulation was described by a factor $(1/T_p)$. This was taken as the multiplicative factor by which the measured impedance signal would be reduced.

Another factor to consider is *dispersion*. Because there were several axons in the nerve bundle, several action potentials were propagated. The collective name for these is a *Compound Action Potential (CAP)*. In reality, there is a distribution of fibre diameters in the bundle, causing individual fibres to conduct action potentials with a distribution of velocities. There is theoretical (*e.g.* Noble, 1979) and experimental (*e.g.*, Hodgkin, 1954) evidence that unmyelinated fibres conduct at a rate proportional to $2a$ so larger fibres conduct the action potential more quickly. As a consequence the magnitude of the CAP decreases with distance along the nerve as its temporal spread increases. Since the individual action potentials reach the measurement region at different times, there is incomplete depolarization there. The

model accounts for this reduction to provide a more accurate estimate of the change to be measured on an actual peripheral nerve.

The fibre diameters also effect the size of each axon's contribution to the signal when it is measured by an extracellular electrode. Since the intracellular and extracellular resistances act as a potential divider, the ratio of extracellular to intracellular volume determines the size of the action potential and larger fibres generate a larger extracellular action potential.

It was assumed that, at any given instant in time during depolarization, the voltage developed by a class of fibres was proportional to (i) the radius of fibres in that class, and (ii) the proportion these fibres occupy of the overall nerve area. Individual action potentials were modelled as pulses and the ratio C_p found of predicted CAP with and without the dispersion effects. $(1/C_p)$, to a first approximation, would be the same as the ratio of the measurable resistance decrease to that predicted by the two state model above for full depolarization.

As a result of these considerations, the model predicted a resistivity change of $(1/T_pC_p)*\Delta P_0\%$ to be measured on a depolarising sample of the walking leg peripheral nerve of a crab.

Peripheral Neurons			Cortical Neurons		
Parameter	Value	Source	Parameter	Representative Value (Range)	Source
ρ_I	90 Ωcm	(Hodgkin and Rushton 1946)	ρ_i	70 Ωcm (50-100Ωcm)	(Rall 1975)
ρ_m	8000 Ωcm^2	(Hodgkin and Rushton 1946)	ρ_m	2500 Ωcm^2 (10^3-$10^4\Omega$cm^2)	(Rall 1975) (motoneuron)
C_m	1.0 μF/cm^2	(Hodgkin and Rushton 1946)	C_m	2μF/cm^2 (1-4μF/cm^2)	(Rall 1975)
τ_m	8ms	from ρ_m and C_m	τ_m	5ms (1-40ms)	from ρ_m and C_m
1-α	0.75	(Keynes and Lewis 1951)	1-α	0.45	(1-β)/ 2
ρ_e	20 Ωcm	(Hodgkin and Rushton 1946)	ρ_e	60 Ωcm	(Ranck 1963)
α	0.25	(Keynes and Lewis 1951)	β	0.1	(Ranck 1963)
-	-	-	ρ_{ie}	70 Ωcm (50-100Ωcm)	assumed equal to ρ_i
-	-	-	γ	0.45	(1-β)/ 2
2L	1mm	electrode spacing	2L_e	1.5 (1-2)	(Rall 1975)
A	4 μm	(Keynes and Lewis 1951)	a	17μm (11-50)	(Rall 1975)
D_p	40	(Cole and Curtis 1939)	D_c	(9 - 5.5)	(Araki and Terzuolo 1962)

Table 5-1: Parameters, taken from the literature, necessary for calculating conductivity of unmyelinated crab peripheral nerve tissue and cortical tissue.

180
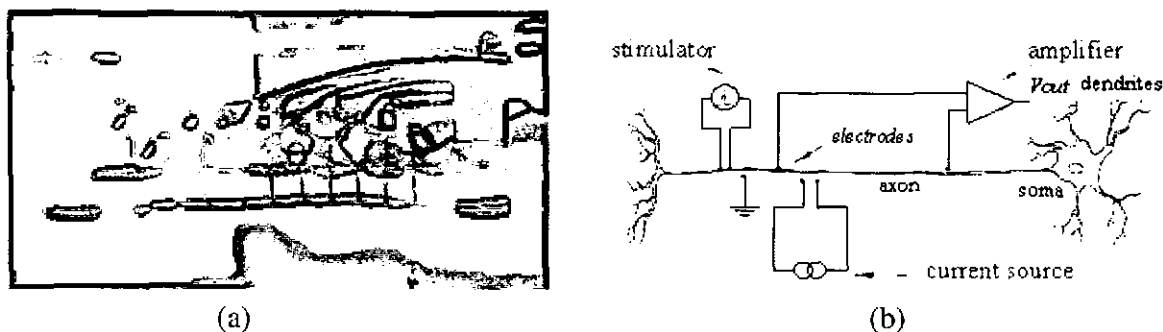
Figure 5-3. (a) Photograph and (b) diagram of experimental set-up for measurement of longitudinal resistance changes in unmyelinated crab peripheral nerve axons. The *axon* of the crab nerve was suspended on silver electrodes and the *dendrites* can be seen in (b) extending from the cell body or *soma*.

5.2.1.7 Experimental Procedure

A method was developed to measure the longitudinal impedance change during the depolarization of the nerve bundle extracted from the walking leg of a crab, *Cancer Pagurus*. As can be seen in Figure 5-3(a), this was suspended by a series of silver electrode hooks at various distances from each other (Boone 1995). It was lowered into an ice-cooled bath of Ringer's solution (an electrolyte) between measurements for preservation purposes.

Two impedance measurements were made alternately. For the first, the *odd* measurement, DC was driven one way in the region of interest between two *driving* electrodes separated by 1mm. A battery-powered current generator was used and was triggered via an optical isolator. The potential difference was measured simultaneously between two *measurement* electrodes, one placed several millimetres more proximal to the site of nerve stimulation than the driving electrodes and the other placed several centimetres more distal. The amplifier used for the voltage measurement was isolated from the controlling PC and from its mains power supply. The nerve was attached to a common ground at a point between the 4-terminal measurement electrodes and the stimulating electrodes, as shown in Figure 5-3(b). The *even* measurement was made whilst driving DC in the opposite direction to that in the odd measurement so that the delivered current took the form of a square wave.

The collective depolarization of the nerve fibres generated a compound action potential (CAP), which propagated along the nerve. The shape of the CAP near the stimulator resembled that of an action potential (AP) that may be seen on an individual fibre. However, the magnitude of the CAP decreased and its spread increased due to dispersion as it passes along the nerve. The placing of one measurement electrode close to the stimulating electrodes and another at a large distance ensured that the measured CAP was monophasic and the

181

placing of the former several length constants upstream of the proximal drive electrode ensured that the current injection did not have an effect on the shape of the measured CAP. This enabled separation of that part of the recorded signal that was the CAP and that which was the associated resistance change.

The CAP was initiated at the same time during each half-period of the current cycle using an isolated, battery-powered pulse generator and about 150 full cycles were recorded. During each half-cycle, the CAP generated an increase in the voltage, whereas the change in resistance caused a simultaneous decrease in its magnitude. For this reason we subtracted each even section of the trace from each odd section in an averaging process that cancelled the CAP's but preserved the resistance decreases. A baseline was fitted to the averaged half-cycle and the resistance change was seen as a deviation from the baseline.

5.2.2 The Cortical Model

Dendrites are the most prevalent neuronal processes in the cortex. These are randomly oriented and branch off into tree-like structures, or *arborisations*, which can be seen in Figure 5-3(b). *Glial cells* also make up a proportion of cortical volume comparable to neurons. They have a geometry similar to that of the neurons and must be accounted for as a third compartment in the model. Blood also makes up 2% of cortical volume (Ranck 1963) but was not included in the following model.
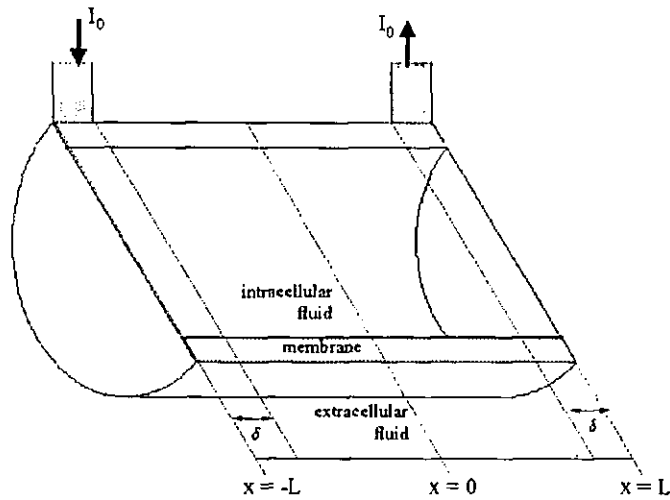
Figure 5-4: A cut-away diagram showing the geometry of the cortical nerve fibre model.

5.2.2.1   Assumptions and Approximations

(C1) As Rall (Rall 1975) proposed, a dendritic arborisation was represented by a single, equivalent (*virtual*) cable of electrotonic length $L_e=(L/\lambda)$, conduction in which was governed by simple cable theory.

(C2) Each of these cables is equally likely to have any orientation and its midpoint to have any co-ordinate. When integration is performed over a solid angle of 2π, it can be seen, and was assumed, that the collective resistivity of a population of these cables is 3 times that of a population which is randomly distributed but parallel (Ranck 1963). This result holds when the region of interest lies greater than 300μ from the current source, in which case Ranck suggested that field lines were nearly parallel.

(C3) r_m, c_m and r_i were again assumed to be constant on each branching cable and the cell passive and linear with respect to the testing current.

(C4) The nerve process, a uniform, virtual cylinder was assumed to consist of purely resistive *intracellular fluid* surrounded by a *membrane*. When glial cells were considered, the

183

cable was bathed not only in *extracellular fluid* (resistivity p_e Ω.cm) but surrounded also by the conductive *glial cells*. It was assumed that the effects of blood vessels and of connective tissue are negligible in grey matter and we considered only neurons, interstitial space and glial cells. These constituted two resistive components in parallel surrounding the neuronal process. Since the neuroglial fibres are many times longer than their length constants (a few microns), it was assumed that the longitudinal resistivity of the glial component may be considered to be equivalent to that of its intracellular fluid (resistivity ρ_{gi} Ω.cm). However, since glial transverse resistivity is much higher than this, and the fibres were assumed to be oriented randomly, the overall glial resistivity was assumed to be three times the longitudinal value.

(C5) Extracellular resistance was increased by a factor of $U = 1.42$ due to the increased path length of current flowing around each cable (Ranck 1963).

(C6) Ranck (Ranck 1963) proposed that the virtual cable representing a dendritic arborisation constituted one half of a longer cable with sealed ends, the other half of which extended from the other side of the cell body and was equivalent to another arborisation. It was assumed therefore that the average arborisation on one side of a plane through the soma was the same as that on the other side. Further to this, the cell body was assumed to have no effect on the longitudinal resistance of this cable (Ranck 1963), which seems reasonable since the surface area of dendritic trees is about 20 times that of the soma (Rall 1975). The axon was omitted in the model.

(C7) Assumption (C6) suggested the placement of the measuring electrodes in the model for a single process. They were situated $x=\pm L$ $\therefore$ $\pm L_e \lambda$ apart along the length of the cable, with the soma at $x=0$ and the axon assumed to be sufficiently thin that the electric field in the intra- and extracellular space was parallel to the fibre.

(C8) The extrapolar length of the axon was therefore zero and the cable was assumed to be 'sealed-ended' i.e. $i_i(\pm L)= 0$.

(C9) The process was again assumed to exist in two steady states, *resting* and *depolarising*. In the former state, the longitudinal conductivity was calculated using the expression derived below and all the relevant parameters. In the latter state, this was repeated with membrane resistivity multiplied by a factor $(1/D_c)$.

5.2.2.2   Notation

Additional Variables

$\tilde{i}_e$ total extracellular current (A), including that passing through glial cells

$\tilde{I}$ total current flowing through the axon and extracellular fluid ($\tilde{I} = \tilde{i}_e + i_i$)

$\tilde{V}_e$ potential (V) of extracellular fluid with respect to a distant point: $\tilde{V}_e = -\int_{-\infty}^{x} r_e \tilde{i}_e dx$

$\tilde{V}_m$ the potential difference (V) across the surface of the membrane ($\tilde{V}_m = \tilde{V}_e - V_i$)

Additional Constants

β proportion of tissue consisting of extracellular fluid

γ proportion of tissue consisting of glial cells

α proportion of tissue not consisting of neurons ($\beta + \gamma$)

U a factor 1.42, to include the effect of tortuosity (Ranck 1963)

ρ_g specific resistivity of the glial intracellular fluid (Ω cm)

$\tilde{r}_e$ effective resistance per unit length (Ω cm^{-1}) of tissue surrounding neurons

$\tilde{\lambda}$ length constant $= \sqrt{[r_m / (r_i + \tilde{r}_e)]}$

These new constants allowed us to consider the longitudinal resistance of three compartments using the same approach as for two compartments but replacing the variable r_e in that approach with $\tilde{r}_e$. The constant $\tilde{\alpha}$, which will be introduced below, suggests an 'effective' extracellular volume. As described in section 5.2.1.4, expressions for conductivity reported in the remainder of this chapter are valid at frequencies greater than zero if $\tilde{\lambda}$ is replaced by $1/\tilde{F}$.

5.2.2.3   Theory

Each of the parallel conductors are present in proportions of $(1-\alpha)$, β and γ. It is necessary to define the resistance per unit length (Ω cm^{-1}) of each compartment separately.

$$r_i = \frac{\rho_i}{\pi a^2}, \; r_e = \frac{U(1-\alpha)\rho_e}{\beta \pi a^2} \text{ and } r_g = \frac{3(1-\alpha)\rho_{gi}}{\gamma \pi a^2}$$

where the factors of 3 and U are included for and random orientation tortuosity, as explained in assumptions (3.1) and (3.2).

Adding these resistances in parallel, the resistance that appears as extracellular to the neurons is

185

$$\tilde{r}_e = \frac{3U(1-\alpha)}{\pi a^2}\left(\frac{1}{3\beta\rho_{gi} + U\gamma\rho_e}\right)\rho_{gi}\rho_e$$ [5-25]

This could be expressed more simply as

$$\tilde{r}_e = \frac{U(1-\alpha)}{\tilde{\alpha}\pi a^2}\rho_e$$ [5-26]

where [5-27]

$$\tilde{\alpha} = \left(\beta + \frac{\gamma U\rho_e}{3\rho_{gi}}\right)$$

acts as an 'effective' extracellular tissue proportion ($1-\alpha$) remains the geometric proportion of tissue classed as intracellular neuronal space. $\tilde{r}_e$ and $\tilde{\lambda}$ are substituted for r_e and λ in all the relationships between current and voltage in section 2.1.

Since, again, the voltage distribution must be anti-symmetric between the electrodes, the solution to the DC steady state cable equation is

for $\frac{\delta - L}{\lambda} < X < \frac{L - \delta}{\lambda}$ $\qquad V_m = Ae^X(1 - e^{-2X})$ [5-28]

It follows that

$$\frac{\partial V_m}{dX} = Ae^X(1 + e^{-2X})$$ [5-29]

Using the new variable X, [5-3] becomes

$$\frac{\partial V_m}{dX} = \tilde{\lambda}(\tilde{r}_e + r_i)i_i - I\tilde{r}_e\tilde{\lambda}$$ [5-30]

[5-29] and [5-30] can be equated for $x = -L+\delta$ but when $\delta \to 0$, $i_i(-L+\delta) \to 0$ ("sealed-end" boundary conditions) so that

$$A = -\frac{\tilde{r}_e I_0\tilde{\lambda}}{1 + e^{\frac{2L}{\tilde{\lambda}}}} e^{\frac{L}{\tilde{\lambda}}}$$ [5-31]

[5-30] is rearranged so that

$$\frac{\partial V_m}{dX} = -\tilde{\lambda}(\tilde{r}_e + r_i)i_e + Ir_i\tilde{\lambda}$$ [5-32]

And this is integrated between X = -L / λ and L / λ when $\delta \to 0$. Using [5-1], we obtain

$$\frac{2\tilde{r}_e I_0 \tilde{\lambda} e^{\frac{2L}{\tilde{\lambda}}}}{1+e^{\frac{2L}{\tilde{\lambda}}}}\left(1-e^{-\frac{2L}{\tilde{\lambda}}}\right) = \frac{(\tilde{r}_e + r_i)}{\tilde{r}_e}\left[V_e\left(-\frac{L}{\tilde{\lambda}}\right) - V_e\left(\frac{L}{\tilde{\lambda}}\right)\right] - 2Lr_i I_0 \qquad [5\text{-}33]$$

The term in square brackets is equivalent to the applied voltage V_0 so, if [5-33] is rearranged in the same way as is [5-21] to produce [5-22], we obtain the specific resistance of a volume made up of parallel neurons, extracellular fluid with included tortuosity effects and randomly oriented glial cells

$$P_0^C = \frac{U\rho_e \rho_i}{[(1-\alpha)U\rho_e + \tilde{\alpha}\rho_i]} + \frac{(U\rho_e)^2(1-\alpha)\sinh\left(\frac{L}{\tilde{\lambda}}\right)}{\tilde{\alpha}[(1-\alpha)U\rho_e + \tilde{\alpha}\rho_i]\left(\frac{L}{\tilde{\lambda}}\right)\cosh\left(\frac{L}{\tilde{\lambda}}\right)} \qquad [5\text{-}34]$$

This model accounts for 'sealed end' boundary conditions and there is a $\cosh^{-1}$ term replacing the exponential term in the 'open end' solution [5-22]. In all other respects, the two are virtually the same except that ρ_e is replaced by $U\rho_e$ and every α that occurs outside of the $(1-\alpha)$ parenthesis (representing the neuronal proportion) is replaced with an 'effective' extracellular proportion $\tilde{\alpha}$.

5.2.2.4   Parameters and Evaluation

It is common (Ranck 1963; Boone 1995) to consider the specific admittance of cortical tissue to be the simple sum of (a) the admittance of the neuronal compartment ($[1-\alpha]^*y_n$), (b) the admittance of the neuroglial compartment ($Y_{gi} = \gamma / 3\rho_{gi}$), and (c) the admittance of the extracellular fluid ($Y_e = \beta / U\rho_e$) when each are considered to be "in parallel".

$$Y_0^{par} = (1-\alpha)y_n + \frac{\beta}{U\rho_e} + \frac{\gamma}{3\rho_{gi}} \equiv \frac{1}{P_0^C} \qquad [5\text{-}35]$$

or

$$y_n \equiv \left(\frac{1}{(1-\alpha)}\right)\left(\frac{1}{P_0^C} - \frac{\tilde{\alpha}}{U\rho_e}\right) \qquad [5\text{-}36]$$

From assumption (C2), the overall conductivity of cortical tissue, in which the dendritic processes are randomly oriented, is therefore

$$Y_0^{rand} = \frac{1}{3}\left(\frac{1}{P_0^C} - \frac{\tilde{\alpha}}{U\rho_e}\right) + \frac{\tilde{\alpha}}{U\rho_e} \equiv \frac{1}{P_0^{C(rand)}} \qquad [5\text{-}37]$$

As can be seen in Table 5-1, there are ranges of reported values for the parameters required to evaluate [5-37]. N_p permutations of several plausible values were used in order to calculate N_p values of $\Delta P_{0n}^{C(rand)}\%$ where $n=1,...,N_p$. Our reported value of $\Delta P_0^{C(rand)}\%$ was calculated using representative values of each parameter and the error by looking at the maximum and minimum values of $\Delta P_{0n}^{C(rand)}\%$.

5.2.2.5   Realistic Considerations

This time, to account for the reductive effect of membrane capacitance as the system switched between 'resting' and 'depolarising' states, a factor of $(1/T_c)$ was calculated using a time constant $\tau_m = 5\text{ms}$ (1ms-40ms), calculated using the parametric values in Table 5-1, and a resistance drop to $(1/D_c)$.

Since the model of cortical resistivity above applies when the entire neuronal population depolarizes, a factor $(1/C_c)$ was introduced to account for those neurons which do not depolarize. The effect is to reduce the signal to a fraction equal to the proportion of cells which are active. This is not known but Elul (1967) proposed that the simultaneous activity of 10-20% of the neuronal population produces an evoked potential, or EEG signal. The evidence for this is unclear but, for the purposes of this study, a conservative estimate was made and a figure of 10% was used. A larger proportion may be recruited during more vigorous activity such as an epileptiform spike

The impedance signal on the scalp will be further reduced because of the distance of the measurement electrodes from the change and because between the two lies the highly resistive skull. The model only predicts a localized resistivity change. A method will be described in the next section to predict scalp signals it causes.

5.2.3   Prediction of Scalp Measurements

It was attempted to use the realistic FEM model to predict signal changes on the scalp,
since the visual area could be well defined in the brain region of the mesh (Figure 5-5). It was
defined as all those nodes in the brain behind a vertical plane 20mm in front of the extreme
posterior of the brain and between horizontal planes 20mm above and below z=0. The total
volume represented by this change was about 10cm^3. Simulations were carried out using
equation 1-14 and the sensitivity matrix $A_{human}^{FEMfullhead}$. Appropriate conductivity values were
changed, first, by 5%, the conductivity changes expected due to increased blood flow. This
was in order to test the predictions against data measured during the VER's, described in the
previous chapter. If the two compared well, the model would seem reasonable and, since
equation [1-14] is linear, the predicted changes would be multiplied by $\Delta\sigma_{neuronal}\%$ / 5%,
assuming that the change due to neuronal depolarization occupied a similar volume to the
blood flow change.
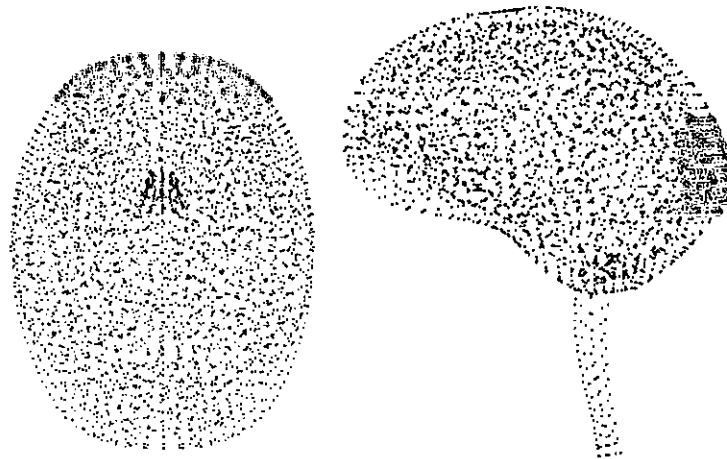
Figure 5-5: The nodes in the head mesh defined as the brain (black .) and those also defined as the visual
cortex for simulation.

It was found that predictions for scalp impedance changes, using the FEM model, were
about an order of magnitude smaller than the values actually measured on human subjects.
Predictions for the skull tank (4.2.3.4) were more consistent with measurements, when the
head shaped mesh was used, but poor results were obtained using the spherical models.
Revisiting the experiments in chapter 3, predicted changes were several orders of magnitude
smaller than measured changes using both analytical and numerical models. These difficulties

were not resolved so I assumed the crude reduction factor 0.1 suggested above in order to estimate the mean, negative changes and 0.2 to estimate the maximum change.

5.3   Results

5.3.1   Predictions of the Peripheral Model

For an electrode spacing of 1mm, the ideal *peripheral model* predicted a DC resistance decrease of 22.3%. When the effects of capacitance $(1/T_p)$ = 0.62 and incomplete depolarization $(1/C_p)$ = 0.2 are taken into account, the model predicts a measured decrease of 2.8%. Figure 5-6 shows the frequency variation of the solution and Figure 5-7 the capacitive effect on the measured signal.
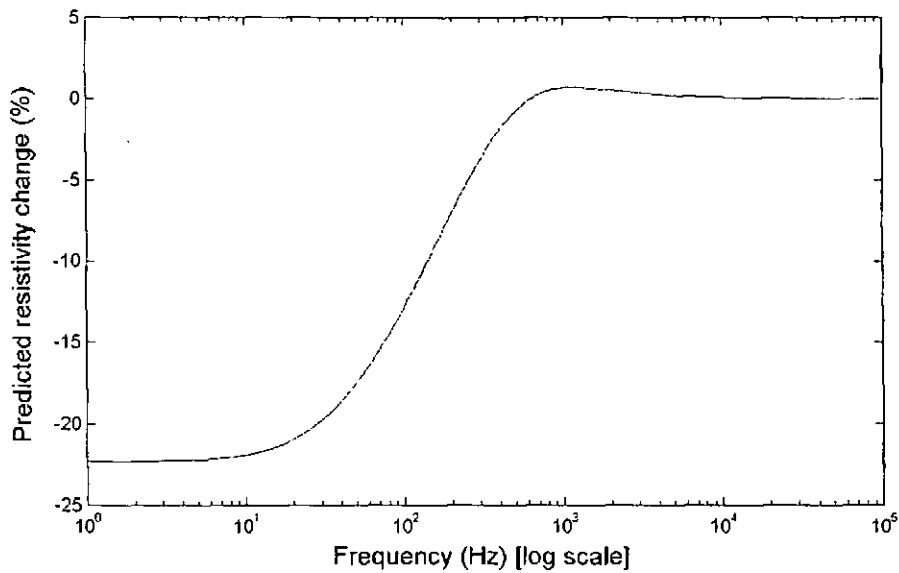
Figure 5-6. The predicted change in resistivity versus frequency during depolarization of a uniform peripheral nerve sample (4μm radius) for an electrode spacing of 1mm. This prediction does not take into account any of the realistic considerations discussed above.
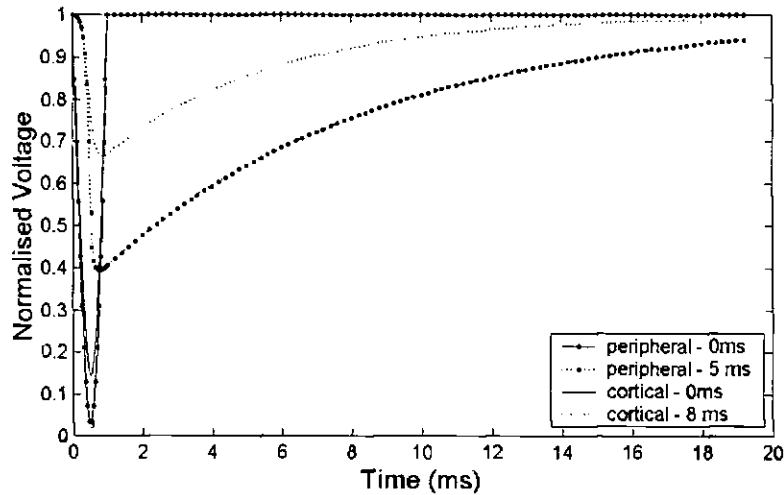
Figure 5-7. The time course of voltages simulated across RC circuits as R is varied to represent depolarising peripheral nerve membrane (8ms) and cortical nerve membrane (5ms). These are shown with the voltage that would be developed id the time constant were 0ms in each case. All voltages were normalized relative to the steady state voltage IR.

5.3.2 DC Resistance Changes as Measured on Peripheral Nerves

Using the technique described above and an excitation electrode spacing of 1mm, (Boone 1995) measured a DC resistance change of −1.0%±0.6% at the peak of depolarization in peripheral nervous tissue. Barbour (Barbour 1998) repeated these experiments and reported a change of −1.1%±0.1%. An example trace is shown in Figure 5-8. Using a larger current electrode spacing and measuring further from the stimulus, Holder (Holder, 1989) reported a longitudinal resistance change of −0.3%.
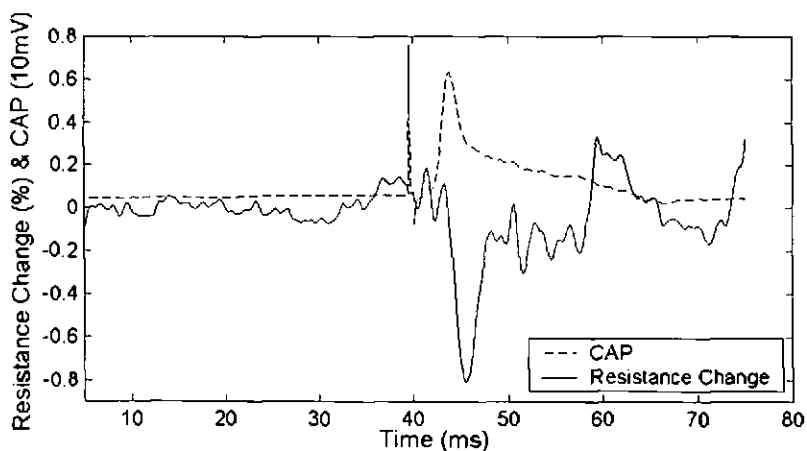
Figure 5-8. A typical trace showing the Compound Action Potential and the percentage resistance change observed when a measurement is made on crab peripheral nerve in the fashion described above.

5.3.3   DC Predictions of the Cortical Model

Using representative values and ranges of parameters, the *cortical model* predicted a bulk resistivity of 270Ωcm (203 – 353Ωcm). The ideal model predicted a resistivity decrease of 15.6% (11.1-18.4%).

When the effects of capacitance $(1/T_c) = 0.39$ (0.05-0.93) and incomplete depolarization $(1/C_c) = 0.1$ were taken into account, the model predicted an effective decrease of 0.6% (0.06-1.7%).

5.3.4   Scalp impedance changes

Mean scalp signal changes were estimated assuming a reduction factor of 0.1 and maximum changes assuming a reduction factor of 0.2 (section 5.1.1). If local changes were as quoted in the previous section, this translates into predicted mean scalp signal decreases of 0.06% (0.006-0.17%) for impedance measurements made there. Maximum signals would have magnitude 0.12% (0.012-0.34%).

5.4   Discussion

It can be seen in Figure 5-6 that the resistivity change is maximal at DC. At this frequency, the new *peripheral model* predicted a resistance decrease of about 2.8% rather than 3.7%, as suggested by Boone (1995). The model assumed boundary conditions more appropriate to those during measurement of a 1% decrease, as described above. During measurement, it was possible (a) that the nerve tissue was not completely depolarized at the stimulating electrodes, (b) that remnants of Ringer's solution were absorbed by the fascicles of the nerve while it was submersed and (c) that the measuring instrument underestimated resistance changes, as it did in calibration studies. Especially considering all of these factors, which would act to reduce the measured change slightly, the theoretical prediction and the measurements were in broad agreement.

The representative value predicted by the *cortical model* for bulk cortical resistivity fell well within the range reported in the literature. The same model predicted a representative value for the local resistivity change, at DC, of –0.6% for evoked responses, a result that would translate to 0.06% scalp changes.

It is difficult to compare the predictions with the existing reports of *in vivo* measurements due to the range of frequencies and different measurement configurations used. The sensitivity of the Klivington and Galambos (Klivington and Galambos 1967; 1968) resistance measurements was maximal in the region of depolarization so their reported figures were roughly equivalent to measurements of localized resistivity change. However, the measurement was made at 10kHz, at which frequency the above model is not optimized and phase considerations may need to be made. In preliminary measurements Boone observed a decrease at DC of 0.01-0.03% during evoked responses in rabbit cortex. The results require confirmation but these distant measurements seem consistent with the predictions of the *cortical model*. However, measurements of resistance are acutely sensitive to the placement of the electrodes and their proximity to the activity. Without resolving issues in the use of FEM methods for bulk field calculations, it is difficult to compare measurements reporting a resistance change, to the predictions of the model, which concern a localized change in resistivity.

Many assumptions have been made in the *cortical model*, two of which appear to have the most significant effect on its predictions. The literature reports electrotonic length L_e for many different types of neuron but only the range of values for cat spinal motoneurons has been used in this model. Perhaps a more complete model of resistance changes in the cortex during depolarization would take into account the different active neuronal populations and

their different electrotonic lengths. The resistance change is very sensitive to the reduction of L_e from 1.5*λ to λ, so it may be that different neurons contribute more or less to the resistivity change per unit population density, depending on their electrotonic length. However, the integrative properties of dendritic trees require that electrotonic length is neither too large, in which case distal synaptic input would never cause a neuron to fire, nor too small, in which case the neuron would fire constantly (Rall 1975). It is not unreasonable to suggest that the range of values of L_e used in the model above represents adequately those of the entire set of cortical neurons.

Dendrites were long thought only to depolarize electrotonically, which is to say that they do not actively propagate action potentials as do axons. Instead they were thought to depolarize passively and locally, at varying degrees of synchronization along their length. Since most of the membrane in the cortex is dendritic, the above model would drastically overestimate the bulk resistivity change associated with neuronal depolarization. However, most neuronal dendrites are now believed to have excitable properties (Segev and Rall 1998; Rall 1999; Segev and London 1999) although the dendritic membrane resistance change during depolarization is unknown and difficult to measure. (Araki and Terzuolo 1962) were unsure whether to report a somatic or a dendritic resistance change after their voltage clamp experiments from which we took values for D_c. However, there is a near linear relation between the percentage membrane resistivity change and the bulk resistivity change so their result suffices as an order of magnitude estimate.

Using the crude estimate presented in section 5.1.1, scalp EIT signals of order –0.06% may be expected during evoked responses. However this is dependent on the assumption that synchronous depolarization occurs throughout a similar volume to that occupied by blood flow changes. Boone presented a typical cortical recording of resistance change during median nerve stimulation on a rabbit (Boone 1995). Noise on this trace is of order 0.03% after 800-2000 stimulations. The smallest predicted resistance changes 0.006% would not be observed but the representative value would give a signal to noise ratio of 2. The model therefore predicts that it would be possible to measure resistance decreases with a 10/20 system of electrode placement after 800-2000 evoked responses.

Our group expects soon to make DC single channel scalp measurements of the fast cortical resistance changes that accompany evoked responses in humans. These will be compared to the predictions of the model described above. Further work may involve use of the cable model to predict slower impedance changes due to cell swelling, thought to be responsible for some of the signals observed in previous EIT images.

In summary, the smallest predicted mean signal decreases were of the same order as the change of 0.01% predicted by Boone. Representative mean signal decreases were 6 times larger, the representative, maximum predicted change was 12 times larger and the upper limit of the maximum predicted change was 34 times larger.

5.5   Conclusion

Scalp signals generated by the predicted resistivity changes are at the limit of detectability using hardware presently available and image reconstruction is already difficult, even with the larger signals obtained previously. At present, the predicted resistivity decrease could not be imaged but, allowing for improvements in EIT technology, the technique may be used in the future to produce images of the fast resistance changes associated with neuronal depolarization.

Conclusions and Suggestions

6 Conclusions and Suggestions

6.1 Progress

New mathematical models were presented in this thesis in order to approximate the conduction of electricity through spherical tanks, head-shaped tanks and the human head in order to reconstruct impedance images. Modified models were also presented of conduction through resting and depolarising neuronal tissue.

6.1.1 Modified Reconstruction Algorithm

A new one-step, linear, SVD reconstruction algorithm was suggested in chapter 2 in order to provide a level playing field on which reconstruction could be compared using layered, non-layered, spherical and non-spherical models. The algorithm employed *post-weighting*, which represented an advance on the technique, used previously by this group, of multiplying the resultant image by a radially dependent penalty function. It also reduced electrode artefact since the post-weighting was dependent both on radius and on distance from the electrodes.

Correct *row-normalisation* was also performed for the first time when reconstructing the normalised data acquired by this UCL group (section 2.1.5.2) and the possibility was highlighted of neglecting data when it corresponds to small predictions of voltage measurements (section 2.3.2.2).

6.1.2 New Analytical Shell Model

For the first time, EIT images were reconstructed using an analytical 4-shell spherical model and an algorithm optimized for an inhomogeneous object. Use of the model was shown to produce more accurate image reconstruction of resistance perturbations within concentric shells than did use of a homogeneous model (Chapter 3). The model was also moderately successful for image reconstruction of perturbations within realistic head-shapes, tank and human (Chapter 4), when best-fit electrode positions were used and the reconstructed images were warped.

6.1.3 Testing MaTOAST Linear FEM Implementation

Also presented (Chapter 3) was the first thorough test of the ability of a 3-D, linear FEM model to account for shells in spheres when post-weighting and row-normalisation were incorporated in the reconstruction algorithm. As in the previous study, without these

(Bagshaw, Liston et al. In press), the linear FEM model appeared to be unable to account for the effect of shells.

The same FEM was then applied to a layered, realistic head-shaped 3-D geometry, in chapter 4, and perturbations reconstructed, with moderate success, within a skull in a saline-filled, head-shaped tank. No improvements were gained by inclusion of geometry or layers in the models used but meshing differences were found to be too great to draw general conclusions by this MaTOAST linear FEM implementation. The study was very useful, however, for revealing the importance of meshing and its potential to bias solutions.

6.1.4   Neuronal Depolarisation

New microscopic models were presented of depolarizing tissue using more rigorous approximations and more appropriate boundary conditions than before (Boone 1995). Boone's cortical model was taken further, assuming a range of values for each parameter and assuming that 10% of neurons depolarise in active tissue. The mean scalp signal decrease was predicted as well as the maximum signal expected if the present EIT measurement protocol were to be used. Although signals were predicted which were larger than those predicted by Boone they are still at the limit of detectability under present noise considerations.

6.2   *Future Work*

6.2.1   Reconstruction issues

6.2.1.1   Forward

6.2.1.1.1   Meshing

As a first step, I suggest that further layered and homogeneous head-shaped meshes be produced, with mesh densities as similar to each other and as regular as possible throughout the region of interest, namely the brain. It is desirable for the spheres to be re-meshed also, so that there may be no bias towards the centers of the partitioned octants. These should have density similar to the head-shaped meshes for a fair comparison to be made using the above data, reconstruction algorithm and analysis techniques.

6.2.1.1.2   Quadratic FEM

The results of chapter 3 suggest that the differences, in Chapter 4, between homogeneous and layered, head-shaped reconstruction are likely to have been due to meshing issues rather than the ability of the linear FEM implementation to account for the presence of the thin, resistive skull layer. Should this be confirmed, after repeated studies using better meshes, the next step should be to implement the quadratic FEM within the existing MaTOAST code.

This would take into account thin layers to a higher degree than the linear method (section 2.1.3.2.3). For spherical studies, it may show similar improvements over the homogeneous model as did the analytical multi-shell model, when perturbations occurred within concentric, spherical layers. While the linear FEM may prove useful for modeling realistic geometry, the quadratic FEM might go one step further and also model, more convincingly, the effects of scalp, skull and CSF.

6.2.1.1.3   BEM / FEM

Another method which could better take into account the layers in the head would be to solve a model for the outer layers using the Boundary Element Method (BEM) and then to impose the solution found on the outside of the brain as the boundary condition for a FEM solution inside the brain. BEM / FEM has been applied before to the problem of spherical shells (Bradley, Harris et al. 2001) and for consideration of the electrocardiographic forward problem (Fischer, Tilg et al. 2000). It may be worth considering this method for EIT of brain

function but, as mentioned in section 2.1.3.1, it would sacrifice the potential advantage of the FEM to account for holes and anisotropy in the skull.

6.2.1.1.4 Anisotropy

Perspex presents a much larger resistance perturbation than does any physiological change within the brain and the target image in VER studies is much less well defined than in tank studies. For these reasons, as well as the presence of anisotropy within the human head, the human images in this thesis were much more noisy and difficult to interpret than tank images.

Another reason may be that the human brain is highly anisotropic, whereas tanks were filled with saline, which is isotropic. In the future, once issues of mesh density have been resolved, inclusion of information about the anisotropy of the brain and skull may lead to significant improvements in image quality. This information could be obtained from diffusion weighted MRI (section 1.7.4).

6.2.1.1.5 Capacitance

One further reason, which may account for the significant difference between human images and tank images, is that the human head has capacitive properties while the tanks were purely resistive. Kleinermann suggested that capacitive effects should be taken into account in a model for conduction when frequencies are above 100kHz (Kleinermann 2001). However, this threshold was determined for blood. It is not clear-cut and depends on the biological material under investigation.

Since there is a move by this group towards spectroscopic imaging using frequencies up to and beyond 1MHz, it would be of great use to develop a multi-frequency algorithm where the solution for field is calculated using the full, frequency-dependent Maxwell equations. This has been implemented analytically for a finite right circular cylinder (Kleinermann 2001) and could also be implemented, for brain imaging, using the FEM for a head shape or analytically for concentric spheres. It might also prove useful for single-frequency reconstructions at 38kHz, the frequency used for the human experiments described above, and answer the question more fully as to whether the quasi-static approximation is valid for imaging human brain function.

6.2.1.1.6 Individual MRI's

The logical conclusion of producing more and more accurate models of the head would be to take a diffusion tensor MRI for every subject, since head shapes and internal conductivity distributions vary considerably from individual to individual. Individual MRI's could be segmented, meshed and conductivity tensors defined at each node. It would be trivial then to measure the positions of the scalp electrodes and transfer these directly to the head mesh in order to provide boundary conditions for a full quadratic and anisotropic FEM solution for each subject. At the present time, it is time consuming to produce a full head mesh, since the process is not automated (section 4.2.3.1), and MRI's would not be available for most normal volunteers taking part in evoked response experiments. This method may be practicable for patients with focal epilepsy for whom MRI's are available and it would be desirable to use a model with the greatest accuracy possible to locate the epileptic focus (section 1.4.2.1.3). However, given the inconclusive evidence, presented in this thesis, for the improvement gained by inclusion of correct geometry and conductivity distributions, it does not appear that the production of individual sensitivity matrices is of great priority at the present time.

6.2.1.2 *Inverse*

6.2.1.2.1 *Iterative Reconstruction*

It was suggested in chapter 3 that an iterative process could reduce the noise in regions distant to the perturbation caused by over-compensation by the post-weighting vector. This could be attempted easily using the analytical model and Landweber's linear method (section 1.6.3.5 and equation [1-24]). Since the problem is essentially non-linear, a non-linear iterative solution could be attempted using the FEM solver to generate a new sensitivity matrix at each step using an updated conductivity vector at each step. This would be very time consuming, however, for the fine 3-D meshes required for an accurate head model.

6.2.1.2.2 *A Priori Information*

It would be of great interest to investigate the effect of using *a priori* information by the methods listed in section 1.6.5 concerning smoothness in the image, anisotropy and the reduction of the volume into a smaller number of sensitivity regions. These sensitivity regions could reflect the known anatomy in an individual's head and could also reflect

knowledge of the physiology of an evoked response experiment if the same paradigm were to be used for an fMRI experiment on the same subject.

6.2.2   Image acquisition

For the data reported in this thesis, one image was acquired every 25s during evoked response experiments. Since the physiological response to stimulus occurs over only a few seconds, it would be of great use to carry out further evoked response experiments using the UCLH Mark 1b, with which images can be acquired at a rate of more than $2s^{-1}$. A further advantage of faster image acquisition is that more electrodes could be used and more measurements made to generate each image. The inverse problem would then be better conditioned and resolution would be higher (section 2.1.2.4).

Repeating the VER experiments would also allow improvements to be made to the stimulation paradigm. A more sophisticated example, suggested by Gibson (2000), was to compare images of left field and right field visual stimuli. These would produce similar activation in other regions of the brain, which would cancel, but different activation in the visual cortex. If experiments were to be carried out on subjects who had already taken part in a VER experiment using fMRI, the paradigm could be made as similar as possible for our EIT experiments and results would be directly comparable. These types of experiment could provide a more convincing validation of our reconstruction algorithms for imaging human brain activity.

6.2.3   Neonatal Imaging

A mesh has just been generated, by Andrew Tizzard, of a neonatal head using the I-DEAS package. The mesh will be used, shortly, to produce a neonatal sensitivity matrix using the MaTOAST linear FEM implementation with appropriate electrode positions and conductivities (Gibson, Bayford et al. 2000). This will enable reconstruction of the data already acquired by Dr Tom Tidswell during visual and motor evoked response experiments carried out on neonates in the past, using the UCLH Mark 1b system (section 1.4.2.1.1).

6.2.4   Imaging Epilepsy

Preliminary findings encourage the idea that EIT may be able to offer functional imaging in ambulant patients undergoing presurgical EEG telemetry, which would provide a valuable addition to current clinical practice (Bagshaw, Liston et al. In press). However, much effort remains to be made to process the data collected thus far, since baseline data have often

shown considerable fluctuations and images are highly dependent on the choice of the baseline epoch.

6.2.5   Data and Image processing

None of the suggestions made by Gibson (Gibson 2000) have been implemented, regarding data processing. Noisy data channels are manually removed, rather than weighted according to the inverse of their variance. However, both techniques act to suppress noisy channels and the improvement gained by more sophisticated data processing is unlikely to be dramatic.

In the use of fMRI and PET, images are analysed using a suite of programs, written for Matlab, known as Statistical Parametric Mapping (SPM, Funcional Imaging Laboratory, UCL, Frackowiak, Friston et al. 1997). These produce probability maps showing whether signals in each pixel could have arisen by chance or whether they are likely to be associated with the stimulus. At present, no such analysis is performed on EIT images and SPM could provide substantial benefits in the interpretation of functional brain images. Further collaboration would be recommended with the Functional Imaging Laboratory.

6.2.6   Multi-Frequency Imaging

Mention has already been made of the moves by this group to apply multi-frequency EIT to imaging hemorrhage and ischemia (Sections 1.4.2.1.2 and 1.5.2.3). However, this technique may also improve understanding of the complex mechanisms, which cause EIT signals during evoked responses (Section 1.4.2). The changes are thought to be due to a combination of effects due to blood flow and cell swelling and it would be possible to separate these if multi-frequency measurements were to be made. Images could then be presented with more direct relation to fMRI images, which are reliant on the BOLD response. The new technique could be referred to as BOLD-Related EIT and the future might be said to be BREIT!

6.3   *Reasons to be Positive*

Impedance changes occur during human evoked responses and are easily measured on the scalp using the systems presently available. Although results presented here cast doubt on the ability of EIT to image the small impedance changes associated with neuronal depolarization, it has been shown already that it is possible to reconstruct images of the slower, medium-sized changes due to the metabolic response to brain activity. It is encouraging that human EIT images can be been obtained even when the head is assumed to be a homogeneous sphere. Implementation of the improvements suggested above, in particular meshing, the introduction of a quadratic FEM solution, and the use of *a priori* information, will result in further refinement of the reconstruction algorithm. It is likely that images will then give a more accurate report of the complex and subtle impedance changes occurring in the brain during activity and that they will be understood more fully in relation to the activity they accompany.

References

Akkermans, L. M. A., F. A. Tekamp, et al. (1993). The effects of stress on gastric emptying as measured by electrical impedance tomography. Clinical and Physiological Applications of Electrical Impedance Tomography. D. S. Holder.

Araki, T. and C. A. Terzuolo (1962). "Membrane Currents in Spinal Motoneurons Associated with the Action Potential." Journal of Neurobiology 6: 772-790.

Arridge, S. R., J. C. Hebden, et al. (2000). "A method for three-dimensional time-resolved optical tomography." International Journal of Imaging Systems and Technology 11(1): 2-11.

Ary, J. P., S. A. Klein, et al. (1981). "Location of Sources of Evoked Scalp Potentials: Corrections for Skull and Scalp Thickness." IEEE Transactions on Biomedical Engineering BME-28(6): 447-452.

Avis, N. J. (1993). Image reconstruction in Electrical Impedance Tomography. Sheffield, University of Sheffield.

Avis, N. J. and D. C. Barber (1994). "Image Reconstruction Using Non-Adjacent Drive Configuration." Physiol. Meas. 15(2A): 153-160.

Bagshaw, A. P., A. D. Liston, et al. (In press). "Electrical Impedance Tomography of Human Brain Function using Reconstruction Algorithms based on the Finite Element Method." Neuroimage.

Baillet, S., J. J. Riera, et al. (2001). "Evaluation of inverse methods and head models for EEG source localisation using a human skull phantom." Physics in Medicine and Biology 46: 77-96.

Barber, D. C. and B. H. Brown (1986). Recent developments in applied potential tomography. Information Processing in Medical Imaging. S. L. Bacharach. Dordrecht, Martinus Nijhoff: 106-121.

Barber, D. C. and A. D. Seagar (1987). "Fast reconstruction of resistance images." Clin. Phys. Physiol. Meas. 8(A): 47-54.

Barbour, D. J. (1998). Feasibility Study to investigate whether current impedance measurements could be used to detect C-fibre activity. Clinical Neurophysiology. London, University College London: 103.

Baron, J. C., P. L. Grandie, et al. (1982). "Noninvasive measurement of blood flow, oxygen consumption and glucose utilization in the same brain regions in man by positron emission tomography: Coneise communication." J. Nucl. Med 23: 391-399.

Baumann, S. B., D. R. Wozny, et al. (1997). "The Electrical Conductivity of Human Cerebrospinal Fluid at Body Temperature." IEEE Trans. on Biomed. Eng. 44(3): 220-223.

Bayford, R., Y. Hanquan, et al. (1995). "Experimental validation of a novel reconstruction algorithm for electrical impedance tomography based on backprojection of Lagrange multipliers." Physiol. Meas. 16: A237-A247.

Bayford, R. H., K. G. Boone, et al. (1996). "Improvement of the positional accuracy of EIT images of the head using a Lagrange multiplier reconstruction algorithm with diametric excitation." Physiol. Meas. 17(A): 49-57.

Bayford, R. H., A. Gibson, et al. (2001). "Solving the forward problem in electrical impedance tomography for the human head using IDEAS(integrated design engineering analysis software), a finite element modelling tool." Physiological Measurement 22: 56-64.

Bayford, R. H., Y. Hanquan, et al. (1995). "Experimental validation of a novel reconstruction algorithm for electrical impedance tomography based on backprojection of Lagrange multipliers." Physiol. Meas. 16 (A): 237-247.

Bertero, M. and P. Boccacci (1998). Introduction to inverse problems in imaging, Institute of Physics Publishing.

Binnie, C. D., A. J. Rowan, et al. (1982). A manual of electro-encephalographic technology, Cambridge University Press.

Blue, R. S., D. Isaacson, et al. (2000). "Real-time three-dimensional electrical impedance imaging." Physiol. Meas. 21(1): 27-34.

Bodurka, J. and P. A. Bandettini (2002). "Toward Direct Mapping of Neuronal Activity: MRI Detection of Ultraweak, Transient Magnetic Field Changes." Magnetic Resonance in Medecine 47: 1052-1058.

Bonovas, P. M., G. A. Kyriacou, et al. (2001). "A realistic three-dimensional FEM of the human head." Physiol. Meas. 22: 65-75.

Boone (1995). The possible use of applied potential tomography for imaging action potentials in the brain. Clinical Neurophysiology. London, UCL: 184.

Boone and Holder (1995). "Design considerations and performance of a prototype system for imaging neuronal depolarisation in the brain using 'direct current' electrical resistance tomography." Physiological measurement 16: A87-A98.

Boone, Lewis, et al. (1994). "Imaging of cortical spreading depression by EIT: implications for localisation of epileptic focii." Physiol. Meas. 15(2A): 189-198.

Boone, K., D. Barbour, et al. (1997). " Imaging with electricity: report of the European Concerted Action on Impedance Tomography." Journal of Medical Engineering and Technology(21): 201-232.

Borsic, A., W. R. B. Lionheart, et al. (2002). "Generation of Anisotropic-Smoothness Regularization Filters for EIT." IEEE Transactions on Medical Imaging 21(6): 579-587.

Borsic, A., C. McLeod, et al. (2001). "Realistic 2D human thorax modelling for EIT." Physiol. Meas. 22: 77-83.

Bradley, C. P., G. M. Harris, et al. (2001). "The computational performance of a high-order coupled FEM/BEM procedure in electropotential problems." IEEE Trans Biomed. Eng. 48(11): 1238-1250.

Breckon, W. R. (1990). Electrical Impedance Tomography. School of Computing and Mathematical Sciences. Oxford, Oxford Polytechnic.

Brown, B. H., A. D. Leathard, et al. (1995). "Measured and expected Cole parameters from electrical impedance tomographic images of human thorax." Physiological Measurement 16: A57-A67.

Brown, B. H., R. A. Primhak, et al. (2002). "Neonatal lungs--can absolute lung resistivity be determined non-invasively?" Med Biol Eng Comput 40(4): 388-94.

Bures, J., O. Buresova, et al. (1974). The mechanism and application of Leao's spreading depression of electroencephalographic activity. New York, Academic Press.

Burger, H. C. and J. B. v. Milaan (1943). "Measurements of the specific resistance of the human body to direct current." Act. Med. Scand. 114: 584-607.

Carson, R. E., Y. Wu, et al. (2003). "Brain uptake of the acid metabolites of F-18-labeled WAY 100635 analogs." J Cereb Blood Flow Metab 23(2): 249-60.

Cheney, M., D. Isaacson, et al. (1999). "Electrical Impedance Tomography." SIAM Review 41(1): 85-101.

Cheng, K.-S., D. Isaacson, et al. (1989). "Electrode Models for Electric Current Computed Tomography." IEEE Transactions on Biomedical Engineering 36(9): 918-924.

Cherepenin, V. A., A. Y. Karpov, et al. (2002). "Three-Dimensional EIT Imaging of Breast Tissues: System Design and Clinical Testing." IEEE Transactions on Medical Imaging 21(6): 662-667.

Clay, M. T. and T. C. Ferree (2002). "Weighted regularization in Electrical Impedance Tomography With Applications to Acute Cerebral Stroke." IEEE Transactions on Medical Imaging 21(6): 629-637.

Cole and Curtis (1939). "Electrical Impedance of the squid giant axon during activity." J. Gen. Physiol. 22: 649-70.

Cole, K. S. and A. L. Hodgkin (1939). "Membrane and Protoplasm Resistance in the Squid Giant Axon." The Journal of General Physiology 22(5): 671-687.

Cuffin, B. N. (2001). "Effects of Modeling Errors and EEG Measurement Montage on Source Localization Accuracy." Journal of Clinical Neurophysiology 18(1): 37-44.

Cuffin, B. N. and D. L. Schomer (2001). "Experimental Tests of EEG Source Localization Accuracy in Spherical Head Models." Clinical Neurophysiology 112: 46-51.

Dale, A. M. and E. Halgren (2001). "Spatiotemporal mapping of brain activity by integration of multiple imaging modalities." Current Opinion in Neurobiology 11: 202-208.

Dehghani, H. (1999). Finite element modelling and image reconstruction in single and multi-frequency electrical impedance tomography. Sheffield, Sheffield Hallam University: 166.

Devane, S. P. (1993). Application of EIT to gastric emptying measurement in infants: validation against residual volume method. Clinical and Physiological applications of Electrical Impedance Tomography. D. Holder. London, UCL Press: 113-125.

Dong, G., R. H. Bayford, et al. (2003). "The Application of the Generalized Vector Sample Pattern Matching Method for EIT Image Reconstruction." Physiological Measurement 24: 449-466.

Dudykevych, T., I. Frerichs, et al. (2001). Application of EIT for studying gravity effects on lung ventilation and LBNP induced fluid shifts during parabolic flights. X1 International Conference on Electrical Bio-Impedance, Oslo, unipu forlag.

Eyüboglu, B. M. (1996). "An interleaved drive electrical impedance tomography image reconstruction algorithm." Physiol. Meas. 17 (A): 59-71.

Eyüboglu, B. M., B. H. Brown, et al. (1987). "Localisation of cardiac-related impedance changes in the thorax." Clin. Phys. Physiol. Meas. 8(A): 167-73.

Ferree, T. C., K. J. Eriksen, et al. (2000). "Regional Head Tissue Conductivity Estimation for Improved EEG Analysis." IEEE Transactions on Biomedical Engineering 47(12).

Ferree, T. C., K. J. Eriksen, et al. (2001). "Correction to "regional head tissue conductivity estimation for improved EEG analysis"." IEEE Transactions on Biomedical Engineering 48(6): 742.

Fischer, G., B. Tilg, et al. (2000). "A bidomain model based BEM-FEM coupling formulation for anisotropic cardiac tissue." Ann Biomed Eng 28(10): 1229-1243.

Foster and Schwann (1989). "Dielectric properties of tissues and biological materials: a critical review." Critical Reviews in Biomedical Engineering 17(1).

Fox, P. and M. Raichle (1984). "Stimulus rate dependence of regional cerebral blood flow in human striate cortex, demonstrated with positron emission tomography." Journal of Neurophysiology 51: 1109-1121.

Frackowiak, R. S. J., K. J. Friston, et al. (1997). Human Brain Function, Academic Press.

Freygang and Landau (1955). "Some relations between resistance and electrical activity in the cerebral cortex of cat." Journal of Cellular and Comparitive Physiology 45: 377-92.

Geddes, L. A. and L. E. Baker (1967). "The Specific Resistance of Biological Materials: A compendium of data for the biomedical engineer and physiologist." Med. Biol. Eng. 5: 271-293.

Geselowitz, D. B. (1971). "An Application of Lead Theory to Impedance Plethysmography." IEEE Transactions on Biomedical Engineering **BME-18**(1): 38-41.

Gibson, A. (2000). Electrical Impedance Tomography of Human Brain Function. Clinical Neurophysiology. London, UCL.

Gibson, A., R. H. Bayford, et al. (2000). "Two-dimensional finite element modelling of the neonatal head." Physiol. Meas. **21**: 45-52.

Gibson, A., A. T. Tidswell, et al. (1999). A 3D reconstruction algorithm for imaging impedance changes in the human head. Biomedical Applications of EIT, London, UK.

Gibson, A., A. T. Tidswell, et al. (1999). "Three-dimensional electrical impedance tomography of the human head."

Glickman, Y. A., O. Filo, et al. (2002). "Novel EIS Postprocessing Algorithm for Breast Cancer Diagnosis." IEEE Transactions on Medical Imaging **21**(6): 710-712.

Golub, G. H. and C. F. V. Loam (1996). Matrix Computations, John Hopkins University Press.

Goncalves, S., J. C. d. Munck, et al. (2000). "The application of electrical impedance tomography to reduce systematic errors in the EEG inverse problem--a simulation study." Physiol. Meas. **21**(3): 379-393.

Grinvald, A. (1992). "Optical imaging of architecture and function in the living brain sheds new light on cortical mechanisms underlying visual perception." Brain Topogr **5**(2): 71-75.

Guzowski, J. F., B. L. McNaughton, et al. (2001). "Imaging neural activity with temporal and cellular resolution using FISH." Current Opinion in Neurobiology **11**(5): 579-584.

Hansen, J. H. and C. E. Olsen (1980). "Brain extracellular space during spreading depression and ischaemia." Acta Physiol. Scand. **108**: 355-365.

Harel, N., S.-P. Lee, et al. (2002). "Origin of Negative Blood Oxygenation Level-Dependent fMRI Signals." Journal of Cerebral Blood Flow & Metabolism **22**: 908-917.

Haueisen, J., D. S. Tuch, et al. (2002). "The Influence of Brain Tissue Anisotropy on Human EEG and MEG." Neuroimage **15**: 159-166.

Hebden, J. C., A. Gibson, et al. (2002). "Three-dimensional optical tomography of the premature infant brain." Phys. Med. Biol. **47**: 4155-4166.

Hemingway, A. and J. F. McLendon (1932). "The high frequency resistance of human tissue." Am. J. Physiol. **102**: 56-59.

Hodgkin, A. L. (1947). "The membrane resistance of a non-medullated nerve fibre." J. Physiol. **106**: 305-318.

Hodgkin, A. L. and W. A. H. Rushton (1946). "The electrical constants of a crustacean nerve." Proc Roy Soc Lond B **133**: 444-479.

Hoetink, A. E., T. J. C. Faes, et al. (2002). "Imaging of Thoracic Blood Volume Changes During the Heart Cycle With Electrical Impedance Using a Linear Spot-Electrode Array." IEEE Transactions on Medical Imaging 21(6): 653-661.

Hoffman, C. J., F. J. Clarck, et al. (1973). "Intracortical Impedance Changes during spreading depression." J. Neurobiol. 4: 471-486.

Holder, D. S., A. Rao, et al. (1996). "Imaging of physiologically evoked responses by EIT tomography with cortical electrodes in the anaesthetised rabbit." Physiol. Meas. 17(A): 179-186.

Holder, D. S. and A. J. Temple (1993). Effectiveness of the Sheffield EIT system in distinguishing patients with pulmonary pathology from a series of normal subjects. Clinical and physiological applications of Electrical Impedance Tomography. D. S. Holder. London, UCL Press.

Hua, P., E. J. Woo, et al. (1993). "Using Compound Electrodes in Electrical Impedance Tomography." IEEE Transactions on Biomedical Engineering 40(1): 29-34.

Isaacson, D., M. Cheney, et al. (1992). "Comments on reconstruction algorithms." Clin. Phys. Physiol. Meas. 13: A83-89.

Jagust, W., R. Thisted, et al. (2001). "SPECT perfusion imaging in the diagnosis of Alzheimer's disease." Neurology 56: 950-956.

Jain, H., D. Isaacson, et al. (1997). "Electrical impedance tomography of complex conductivity distributions with noncircular boundary." IEEE Trans Biomed. Eng. 44(11): 1051-1060.

Jerbi, K., W. R. B. Lionheart, et al. (2000). "Sensitivity matrix and reconstruction algorithm for EIT assuming axial uniformity." Physiol. Meas. 21: 61-66.

Jezzard, P. and R. Turner (1996). "Magnetic resonance imaging methods for study of human brain function and their application at high magnetic field." Computerized Medical Imaging and Graphics 20(6): 467-481.

Jin, J. (1993). The Finite Element Method in Electromagnetics. New York, John Wiley & Sons.

Johnson, D. W., W. A. Stringer, et al. (1991). "Stable xenon CT cerebral blood flow imaging: rationale for and role in clinical decision making." Am. J. Neuroradiol 12: 201-213.

Jueptner, M. and C. Weiller (1995). "Review: Does Measurement of Regional Cerebral Blood flow Reflect Synaptic Activity? - Implications for PET and fMRI." Neuroimage 2(2): 148-156.

Kaipio, J. P., V. Kolehmainen, et al. (1999). "Inverse problems with structural prior information." Inverse Problems 15: 713-729.

Kelly, P. A. T. and J. McCulloch (1983). "The effects of GABAergic agonist muscimol upon the relationship between local cerebral blood flow and glucose utilisation." Brain Res 258: 338-342.

Kerner, T. E., K. D. Paulsen, et al. (2002). "Electrical Impedance Spectroscopy of the Breast: Clinical Imaging Results in 26 Subjects." IEEE Transactions on Medical Imaging 21(6): 638-645.

Keynes, R. D. and P. R. Lewis (1951). "The Resting Exchange of Radioactive Potassium in Crab Nerve." J. Physiol 113: 73-98.

Kleinermann, F. (2001). Three Dimensional Modelling of Electrical Impedance Tomography. The Centre for Virtual Environment. Salford, UK, University of Salford: 214.

Kleinermann, F. and N. J. Avis (2000). "Analytical Solution to the three-dimensional electrical forward problem for a circular cylinder." Inverse Problems 16: 461-468.

Klivington and Galambos (1967). "Resistance shifts accompanying the evoked cortical response in the cat." Science 157: 211-213.

Klivington and Galambos (1968). "Rapid Resistance Shifts in Cat Cortex During Click-Evoked Responses." JN 31: 565-573.

Konig, M. (2003). "Brain Perfusion CT in acute stroke: current status." European Journal of Radiology 45: S11-S22.

Kosterich, J. D., K. R. Foster, et al. (1983). "Dielectric permittivity and electrical conductivity of fluid saturated bone." IEEE Trans Biomed. Eng. BME-30(2): 81-86.

Kotre, C. J. (1994). "EIT image reconstruction using sensitivity weighted filtered backprojection." Physiol. Meas. 15 (A): 125-136.

Krings, T., K. Chiappa, et al. (1999). "Accuracy of EEG dipole source localisation using implanted sources in the human brain." Clinical Neurophysiology 110(1): 106-114.

Kristeva-Feige, R., C. Grimm, et al. (1997). "Reproducibility and Validity of Electric Source Localisation with High-Resolution Electroencephalography." Electroencephalography and clinical neurophysiology 103(6): 652-660.

Lauterbur, P. C. (1973). "Image formation by induced local interactions: examples employing nuclear magnetic resonance." Nature 242: 190-191.

Law, S. K. (1993). "Thickness and resistivity Variations over the Surface of the Human Skull." Brain Topography 6(2): 99-109.

Leao, A. A. P. (1944). "Spreading depression of activity in the cerebral cortex." J. Neurophysiol. 7: 359-390.

leHyriac, A. and M. K. Pidcock (2000). "A one step image reconstruction algorithm for electrical impedance tomography in three-dimensional electrical impedance tomography." Physiol. Meas. 21(1): 95-98.

Lionheart, W. R. B. (1998). "Boundary shape and electrical impedance tomography." Inverse Problems 14: 139-147.

Liston, A. D., R. H. Bayford, et al. (2002). "A multi-shell algorithm to reconstruct EIT images of brain function." Physiological Measurement 23: 105-119.

Liu, P. and H. Griffiths (1993). Limitations to the sensitivity of EIT in monitoring tissue temperature in hyperthermia. Clinical and physiological applications of Electrical Impedance Tomography. D. S. Holder. London, UCL Press: 211-217.

Logothetis, N. K., J. Pauls, et al. (2001). "Neurophysiological investigation of the basis of the fMRI signal." Nature 412(6843): 150-158.

Lux, H. D., U. Heinemann, et al. (1986). Ionic changes and alterations in the size of the extracellular space during epileptic activity. Advances in Neurology. A. V. Delgado-Escueta, A. A. W. Jr, D. M. Woodbury and R. J. Porter. New York, Raven Press. 44.

Mangnall, Y. F., A. J. Baxter, et al. (1987). "Applied potential tomography: a new non-invasive technique for assessing gastric function." Clin. Phys. Physiol. Meas. 8 (A): 119-131.

McArdle, F. J., B. H. Brown, et al. (1993). Imaging cardiosynchronous impedance changes in the adult head. Clinical and physiological applications of Electrical Impedance Tomography. D. S. Holder. London, UCL Press: 177-183.

Menon, R. S. (2001). "Imaging function in the working brain with fMRI." Current Opinion in Neurobiology 11(5): 630-636.

Mentis, M. J., G. E. Alexander, et al. (1997). "Frequency Variation of a Pattern-Flash Stimulus during PET Differentially Activates Brain from Striate through Frontal Cortex." Neuroimage 5: 116-128.

Metherall, P. (1998). Three Dimensional Electrical Impedance Tomography of the Human Thorax. Medical Physics and Clinical Engineering. Sheffield, University of Sheffield.

Metherall, P., D. C. Barber, et al. (1996). "Three-dimensional electrical impedance tomography." Nature 380: 509-512.

Molinari, M., S. J. Cox, et al. (2001). "Adaptive mesh refinement tecniques for electrical impedance tomography." Physiol. Meas. 22(1): 91-96.

Molinari, M., S. J. Cox, et al. (2002). "Comparison of algorithms for non-linear inverse 3D electrical tomography reconstruction." Physiol. Meas. 23(1): 95-104.

Morucci, J.-P., M. Granié, et al. (1995). "3D reconstruction in electrical impedance tomography using a direct sensitivity matrix approach." Physiol. Meas. 16 (A): 123-128.

Morucci, J.-P., P. M. Marsili, et al. (1994). "A direct sensitivity matrix approach for fast reconstruction in electrical impedance tomography." Physiol. Meas. 15(2A): 107-114.

Mosher, J. C., R. M. Leahy, et al. (1999). "EEG and MEG: Forward Solutions for Inverse Methods." IEEE Transactions on Biomedical Engineering 46(3): 245-259.

Mueller, J. L., D. Isaacson, et al. (2001). "Reconstruction of conductivity changes due to ventilation and perfusion from EIT data collected on a rectangular electrode array." Physiological Measurement 22(1): 97-107.

Munck, J. C. d., T. J. Faes, et al. (2000). "The boundary element method in the forward and inverse problem of electrical impedance tomography." IEEE Trans Biomed. Eng. 47(6): 792-800.

Murai, T. and Y. Kagawa (1985). "Electrical Impedance Tomography Based on a Finite Element Model." IEEE Transactions on Biomedical Engineering 32(3): 177-184.

Murphy, D., P. Burton, et al. (1987). "Impedance imaging in the newborn." Clin. Phys. Physiol. Meas. 8(A): 131-140.

Obrig, H. and A. Villringer (2003). "Beyond the visible--imaging the human brain with light." J Cereb Blood Flow Metab 23(1): 1-18.

Okada, Huang, et al. (1994). "Origin of apparent tissue conductivity in the molecular and granular layers of the in vitro turtle cerebellum." Journal of Neurophysiology 72(2): 742-753.

Oostendorp, T. F., J. Delbeke, et al. (2000). "The conductivity of the human skull: results of in vivo and in vitro measurements." IEEE Transactions on Biomedical Engineering 47(11): 1487 -1492.

Patterson, R. P., J. Zhang, et al. (2001). "Variability in the cardiac EIT image as a function of electrode position, lung volume and body position." Physiol. Meas. 22: 159-166.

Paulson, K., W. Lionheart, et al. (1993). "Optimal experiments in electrical impedance tomography." IEEE Trans. Med. Imag. 12(4): 681-686.

Paulson, K., W. Lionheart, et al. (1995). "POMPUS: an optimised EIT reconstruction algorithm." Inverse Problems 11: 425-437.

Pidcock, M. K., M. Kuzuoglu, et al. (1995). "Analytic and semi-analytic solutions in electrical impedance tomography: I. Two-dimensional problems." Physiologocal Measurement 16(2): 77-90.

Pidcock, M. K., M. Kuzuoglu, et al. (1995). "Analytical and semi-analytical solutions in Electrical Impedance Tomography: II. Three-dimensional problems." Physiological Measurement 16(2): 91-110.

Polydorides, N. and W. Lionheart (2001). Electrical Imaging of the Brain using a Realistic Head Model. Biomedical Applications of EIT, University College London.

Raichle, M. E. (1998). "Behind the Scenes of Functional Brain Imaging: A Historical and Physiological Perspective." Proc. Natl. Acad. Sci 95: 765-772.

Rall (1975). The nervous system 1 - Core conductor theory and cable properties of neurons. Handbook of physiology: 39-97.

Rall, W. (1999). An historical perspective on modelling dendrites. Dendrites. G. Stuart, N. Spruston and M. Hausser. Oxford, Oxford University Press: 193-204.

Ramachandran, V. S. and S. Blakeslee (1998). Phantoms in the Brain. London, Fourth Estate.

Ranck (1963). "Analysis of specific impedance of rabbit cerebral cortex." Experimental neurology 7: 153-174.

Ranck (1963). "Specific impedance of rabbit cerebral cortex." Experimental neurology 7: 144-152.

Ranck (1966). "Electrical Impedance in the Subicular Area of Rats during Paradoxical Sleep." Experimental Neurology 16: 416-437.

Ranck, J. (1964). "Specific Impedance of Cerebral Cortex during Spreading Depression, and an Analysis of Neuronal, Neuroglial, and Interstitial Contributions." Experimental Neurology 9: 1-16.

Rao, A. (2000). Electrical Impedance Tomography of Brain Activity: Studies into its Accuracy and Physiological Mechanisms. Department of Physiology. London, University College London: 228.

Rao, A., A. Gibson, et al. (1997). "EIT images of electrically induced epileptic activity in anaesthetised rabbits." Med & Biol. Eng & Comp. 35(1): 327.

Rosenthal, R. L. and C. W. Tobias (1948). "Measurement of the electrical resistance of human blood, use in coagulation studies and cell volume determinations." J. Lab. Clin. Med. 33: 1110-22.

Roth, B. J., M. Balish, et al. (1993). "How well does a three-sphere model predict positions of dipoles in a realistically shaped head?" Electroencephalography and Clinical Neurophysiology 87: 175-184.

Rush, S. and D. Driscoll (1969). "EEG Electrode Sensitivity - An Application of Reciprocity." IEEE Transactions on Biomedical Engineering BME-16(1): 15-22.

Rush, S. and D. A. Driscoll (1968). "Current distribution in the brain from surface electrodes." Anaesthesia and Analgesia 47: 717-727.

Saha, S. and P. A. Williams (1992). "Electric and dielectric properties of wet human cortical bone as a function of frequency." IEEE Trans Biomed. Eng. BME-39(12): 1298-1304.

Saulnier, G. J., R. S. Blue, et al. (2001). "Electrical Impedance Tomography." IEEE Signal Processing Magazine 18(6): 31-43.

Segev and Rall (1998). "Excitable dendrite and spines: earlier theoretical insights elucidate recent direct observations." Trends in Neuroscience 21: 453-460.

Segev, l. and M. London (1999). dendrites: A Theoretical view of passive and actve dendrites. Oxford, Oxford University Press.

Somersalo, E., M. Cheney, et al. (1991). "Layer Stripping: a direct numerical method for impedance imaging." Inverse Problems 7: 899-926.

Stephanesco, S., C. Schlumberger, et al. (1930). "Sur la distribution électric autour d'une prise de tere ponctuelle dans un terrain a couchés horizontales, homogènes et istotropes." J. Physics Radium Sen 7: 132-140.

Tang, M., W. Wang, et al. (2002). "The number of electroeds and basis functions in EIT image reconstruction." Physiol. Meas. 23: 129-140.

Ter-Pogossian, M. M., M. E. Phelps, et al. (1975). "A positron-emission tomograph for nuclear imaging (PET)." Radiology 114: 89-98.

Thevenet, M., O. Bertrand, et al. (1991). "The finite element method for a realistic head model of electrical brain activities: preliminary results." Clin. Phys. Physiol. Meas. 12(Suppl. A): 89-94.

Tidswell, A. T., A. Gibson, et al. (2001a). "Validation of a 3D Reconstruction Algorithm for EIT of Human Brain Function in a Realistic Head-Shaped Tank." Physiological Measurement 22: 177-185.

Tidswell, T., A. Gibson, et al. (2001b). "Three-Dimensional Electrical Impedance Tomography of Human Brain Activity." Neuroimage 13(2): 283-294.

Towers, C. M., H. McCann, et al. (2000). "3D simulation of EIT for monitoring impedance variations within the human head." Physiol. Meas. 21: 119-124.

VanHarreveld, S., Murphy, et al. (1963). "Specific Impedance of Rabbit's Cortical Tissue." American Journal of Physiology 205: 203-207.

VanHarreveld, S. and A. Ochs (1956). "Cerebral Impedance Changes After Circulatory Arrest." American Journal of Physiology 187: 180-192.

Vauhkonen, M., J. P. Kaipio, et al. (1997). "Electrical impedance tomography with basis contraints." Inverse Problems 13(523-530).

Vauhkonen, M., D. Vadasz, et al. (1998). "Tikhonov regularization and prior information in electrical impedance tomography." IEEE Trans Med Imaging 17(2): 285-93.

Vauhkonen, P. J., M. Vauhkonen, et al. (2000). "Errors due to truncation of the computational domain in static three-dimensional electrical impedance tomography." Physiol. Meas. 21: 125-135.

Vaukhonen, M., W. R. B. Lionheart, et al. (2001). "A MATLAB package for the EIDORS project to reconstruct two-dimensional images." Physiol. Meas. 22: 107-111.

Webster, J. G. (1990). Electrical Impedance Tomography.

Welch, K., G. Barkley, et al. (1987). "Central Neurogenic Mechanisms of Migraine." Neurology 43(6): S21-S25.

Wilson, A. J., P. Milnes, et al. (2001). "Mk3.5: a modular, multi-frequency successor to the Mk3a EIS/EIT system." Physiological Measurement 22(1): 49-54.

Wilson, A. J., P. Milnes, et al. (2001). "Mk3.5: a modular, multi-frequency successor to the Mk3a EIS/EIT system." Physiol. Meas. 22: 49-54.

Wirestam, R., E. Ryding, et al. (2000). "Absolute cerebral blood flow measured by dynamic susceptibility contrast MRI: a direct comparison with Xe-133 SPECT." MAGMA (Magnetic Resonance Materials in Physics, Biology and Medecine 11(3): 96-103.

Wright, J. W. (1993). The effect of nutrient and non-nutrient test meals on gastric emptying as measured by EIT. Clinical and physiological applications of Electrical Impedance Tomography. D. S. Holder. London, UCL Press: 100-107.

Xu, P. (1998). "Truncated SVD methods for discrete linear ill-posed problems." Geophys. J. Int. 135: 505-514.

Yerworth, R. J., R. H. Bayford, et al. (2003). "Electrical impedance tomography spectroscopy (EITS) from human head imaging." Physiological Measurement 24(2): 477-490.

Yoon, R. S., A. Czaya, et al. (1999). "Changes in the Complex Permittivity During Spreading Depression in Rat Cortex." IEEE Trans Biomed. Eng. 46(11): 1330-1338.

Yorkey, T. J., J. G. Webster, et al. (1987). "Comparing Reconstruction Algorithms for Electrical Impedance Tomography." IEEE Transactions on Biomedical Engineering BME-34(11): 843-852.

Yvert, B., O. Bertrand, et al. (1997). "A systematic evaluation of the spherical model accuracy in EEG dipole localization." Electroencephalogr Clin Neurophysiol 102(5): 452-459.